Study on the tolerance of partially and fully depleted CPS to non-ionizing radiation

GOETHE
UNIVERSITÄT
FRANKFURT AM MAIN

Dissertation
zur Erlangung des Doktorgrades
der Naturwissenschaften

vorgelegt beim Fachbereich Physik
der Johann Wolfgang Goethe-Universität
in Frankfurt am Main

von
Benjamin Linnik
aus Frankfurt am Main

Frankfurt am Main 2022
(D 30)

vom Fachbereich Physik der
Johann Wolfgang Goethe-Universität als Dissertation angenommen.

Dekan: Prof. Dr. Harald Appelshäuser

Gutachter: Prof. Dr. Joachim Stroth
PD Dr. Michael Deveaux

Datum der Disputation: 29. November 2022

Abstract

Sensors for high rate charge particle tracking have to withstand the harsh radiation doses deposited by the particles to be sensed. This holds particularly for the novel CMOS Monolithic Active Pixel Sensors, which are considered a promising sensor technology for future vertex detectors due to their very light material budget and excellent spatial resolution. To resist the radiation doses expected close to the interaction regions of heavy-ion experiments, the sensors have to be hardened against radiation doses, which exceed the native tolerance of CMOS technology significantly. In this thesis, the results of non-ionizing radiation hardness studies at the IKF on sensor prototypes developed at the IPHC in Strasbourg are presented. Our results demonstrate that the CMOS sensors evaluated in the context of this thesis can withstand non-ionizing radiation of up to $5 \times 10^{14}\,\mathrm{n_{eq}/cm^2}$. This hardness qualifies them as promising candidates for use in future vertex detectors.

Zusammenfassung

In Schwerionen-Kollisionen verschmelzen Atomkerne und Nukleonen in ihre elementaren Bestandteile, die Quarks und Gluonen, und bilden für einen kurzen Augenblick jene Urmaterie, von der man annimmt, dass sie das Universum bis wenige Mikrosekunden nach dem Urknall erfüllte. Die heiße Reaktionszone dehnt sich mit fast Lichtgeschwindigkeit aus, kühlt dabei ab und kondensiert wieder zu einer Vielzahl gewöhnlicher Materieteilchen. Teilchendetektoren müssen möglichst viele dieser Teilchen vermessen und ihre Anzahl, Art, Masse, Energie und Trajektorie aufzeichnen, um die Eigenschaften der Materie unter diesen extremen Bedingungen ermitteln zu können. Hierzu kommen unter anderem, CMOS Monolithisch Aktive Pixel-Sensoren (CPS) zum Einsatz.

Diese sind hochempfindlich und dünn und eignen sich daher hervorragend für die Vermessung der Spuren geladener Teilchen. Jedoch war die Strahlungstoleranz von CPS ursprünglich unzureichend. Diese Einschränkung wurde dank der Forschung zur Strahlenhärte der CPS, sowie verbesserter Herstellungsprozesse in den letzten Jahren um mehrere Größenordnungen zurückgedrängt.

Diese Dissertation untersucht die Strahlungstoleranz einiger vom IPHC Strasbourg entwickelter CPS MIMOSA-Sensoren. Die Arbeit ist in acht Hauptkapitel unterteilt, die unterschiedliche Aspekte der Studien beleuchten. In den ersten drei Kapiteln werden eine allgemeine Motivation, sowie die theoretischen und methodischen Grundlagen vorgestellt. Dabei werden bestehende Konzepte erweitert, um neuartige Sensoren mit einem aktiv verarmten Volumen zu untersuchen.

Das vierte Kapitel zeigt Studienergebnisse zur Verbesserung der Leistung von unbestrahlten CPS in Abhängigkeit von unterschiedlichen Epitaxieschichten. Es wird auf den Einfluss unterschiedlicher Epitaxieschichtdicken und der genauen Dotierungsprofile auf die Ladungssammlungseffizienz (CCE) und das S/N-Verhältnis eingegangen. Um eine bessere Vergleichbarkeit zu vorangegangenen Studien herzustellen werden bekannte Methoden aufgegriffen und auf die neuen Sensoren angewendet. Basierend auf früheren Arbeiten und der erweiterten Messmethode “Volumenanteile der Ladungssammlung” [Doe15, p. 86] vergleichen wir in 0,35 µm Technologie gefertigte MIMOSA-Sensoren mit den, in dieser Arbeit untersuchten, in 180 nm Technologie gefertigte Sensoren mit unterschiedlicher Dicke und Epitaxieschicht-Dotierung. Es wird auch ein Vergleich zu dem vollständig depletierten Pipper-2-Sensor gezogen. Im Vergleich zu den älteren Sensoren haben die hier untersuchten 180 nm Sensoren eine wesentlich höhere CCE und stellen damit eine erfolgreiche Weiterentwicklung dar. Vergleiche hierzu Abbildung 4.4 mit Abbildung 4.5. Die Verbesserung der Ladungssammlungseffizienz lässt sich insbesondere durch die verbesserte Epitaxieschicht erklären. Um diese neuartige Epitaxieschicht näher zu untersuchen, wurden MIMOSA-34 Sensoren mit 18 µm,

20 µm und 28 µm dicken Epitaxieschichten mit einer Fe-55 α- und Sr-90 γ-Quelle bestrahlt und miteinander verglichen. Da das sensitive Volumen der MIMOSA-34-Sensoren nicht vollständig verarmt ist, erfolgt die Sammlung der Signalladung nicht nur durch das elektrische Feld des depletierte Teilvolumen, sondern auch durch Driftfelder zwischen Schichten verschiedener Dotierungskonzentration. Die Ergebnisse zeigen, dass hochohmige Epitaxieschichten mit einer Dicke von 18 µm und einem ausgeprägten “Rampen”-Dotierungsprofil eine bessere Leistung aufweisen als vergleichbare Sensoren anderer Epitaxieschichtdicken und Dotierungen.

Das fünfte Kapitel untersucht unterschiedliche Merkmale von MIMOSA-34 Prototypensensoren, um die bestmögliche Kombination hinsichtlich der Härte gegen nichtionisierende Strahlung zu finden. Zu den untersuchten Parametern gehören die bereits im vorherigen Kapitel untersuchten Epitaxieschicht-Dotierungsprofile, als auch verschiedene Pixel- und Diodengrößen. Die kleinsten untersuchten Pixel haben eine effektive Größe von 26,9 µm, die größten eine von 46,7 µm. Die Diodenflächen reichen von 1 bis 15 µm^2. Es wird festgestellt, dass Sensoren, die im TowerJazz-0,18 µm Herstellungsprozess mit einer 18 µm dicken Epitaxieschicht hergestellt werden vergleichbare Sensoren in Bezug auf Ladungssammlungseffizienz, Signal-Rausch-Verhältnis (S/N) und Härte gegen nichtionisierende Strahlung übertreffen. Die 18 µm dicke MIMOSA-34 P1 Pixel-Matrix mit einem Pixelabstand von 33 µm und einer Diodenoberfläche von 8 µm^2 erreichte im Labor bei Abkühlung auf −60 °C eine nicht ionisierende Strahlenhärte von bis zu $10^{14}\,\mathrm{n_{eq}/cm^2}$. Zum Zeitpunkt des Experiments war dies der höchste erreichte Strahlenhärtewert bei dieser Pixelgröße.

Außer der Pixelgröße wird in Abschnitt 5.3 der Einfluss der Diodengröße auf das S/N diskutiert. Kleinere Dioden haben tendenziell ein geringeres Rauschen, aber auch eine niedrigere CCE. Größere Dioden weisen hingegen ein höheres Rauschen, aber auch eine bessere CCE auf. Ein Optimum wird bei einer Diodenfläche von etwa 5 µm^2 beobachtet, siehe Tabelle 5.4.

Im sechsten Kapitel werden die Auswirkungen einer aktiven Depletierung des Sensorvolumens untersucht. Es werden sowohl neue Messtechniken, als auch theoretische und experimentelle Ergebnisse vorgestellt. Zur theoretischen Beschreibung des Einflusses einer Depletierungsspannung auf Sensoren mit einer kleinen Diode wird in Anhang A ein analytisches Modell hergeleitet. Dieses Modell wird mit im Labor an MIMOSA-34 Sensoren gemessenen und in TCAD simulierten Werten in Unterabschnitt 6.3.1 verglichen. Der bereits im vorherigem Kapitel untersuchte MIMOSA-34 Sensor ist mit einer besonderen Pixelmatrix (P13) ausgestattet, die eine eingeschränkte Depletierung mit einer externen Spannungsquelle mit bis zu 9 V erlaubt. Der Einfluss einer Verarmungsspannung auf das verarmte Volumen ist erheblich geringer als für einen abrupten PN-Übergang erwartet. Vielmehr sagt das analytische Modell einen langsamen Anstieg des Depletionsradius mit der sechsten Wurzel der angelegten Spannung voraus. Dieser langsame Anstieg darf nicht als Sättigung und damit als Anzeichen einer vollständigen Depletierung des Sensors verstanden werden. Sowohl die analytische Lösung, als auch die TCAD Simulation können die gemessenen Depletionsvolumen-Werte sehr gut reproduzieren und sagen eine Teildepletierung voraus.

Trotz der gezeigten geringen Veränderung des depletierten Volumens, hat sich die gemessene CCE von 29,4 % ohne eine aktive Depletierung, auf 43,8 % bei einer angelegten Spannung von 8,3 V deutlich verbessert. Insbesondere die in Abbildung 6.6 gezeigten "Volumenanteile der Ladungssammlung" zeigen, dass die P13 Pixel-Matrix des MIMOSA-34 Sensors durch das aktive Depletieren die Signalladung effizienter sammelt. Der Anteil der mit einer CCE$\geq 40\,\%$ registrierten Fe-55 Treffer hat sich von 28,4 auf 66,9 % erhöht.

Eine vollständige Depletierung des aktiven Volumens sollen speziell mit einer größeren Diode ausgestattete Sensoren der nächsten Generation erreichen. Unabhängige Analysen der Kapazität der Sammeldiode, ihres Leckstroms und der Signalladungsverteilung (charge sharing) deuten darauf hin, dass das aktive Volumen eines Pipper-2 Sensors ab einer angelegten Spannung von 10 V größtenteils depletiert ist. Es wird beobachtet, wie sich diese zur vollständigen Depletierung benötigte Spannung mit der nicht-ionisierenden Strahlendosis erhöht. In Abschnitt 6.5 wird gezeigt, dass Pipper-2 Sensoren bei hinreichender Kühlung und Verarmung mit bis zu 20 V eine nicht-ionisierende Strahlung von bis zu $5 \cdot 10^{14}\,\mathrm{n_{eq}/cm^2}$ bei einem Pixelabstand von 22 µm tolerieren können.

Im siebten Kapitel werden mögliche zusätzliche, nicht vom NIEL-Modell vorhergesagte Strahlenschäden betrachtet. Das aktive Volumen von CPS ist meistens mit Bor p-dotiert, während das für die Berechnung der totalen nicht-ionisierenden Strahlendosis genutzte NIEL-Hypothese reines Silizium zu Grunde legt. Bor wird von thermischen Neutronen unter Freisetzung von kinetischer Energie gespalten: $n + {}^{10}\mathrm{B} \rightarrow {}^{7}\mathrm{Li} + {}^{4}\mathrm{He} + 2{,}8\,\mathrm{MeV}$. In den hoch-dotierten Strukturen erzeugte Spaltionen könnten in die Epitaxieschicht gelangen und dort zusätzliche Volumenschäden verursachen. Um die Auswirkungen der Kernspaltung zu untersuchen, wurden MIMOSA-19-Sensoren der IPHC PICSEL-Gruppe im Garchinger FRM II-Forschungsreaktor mit kalten Neutronen mit einer mittleren Energie von $E_{\mathrm{neutron}} = 1{,}8 \cdot 10^{-3}\,\mathrm{eV}$ bestrahlt. Nach der Bestrahlung wurde die CCE gemessen. Die experimentellen Ergebnisse zeigen eine unerwartete Steigerung der CCE. Eine mögliche Erklärung könnte eine unerwartet starke, strahlungsinduzierte Inaktivierung von Akzeptoren sein, welche die Dotierung der Epitaxieschicht verringert und das Volumen der verarmten Zone um die Ladungssammlungsdiode vergrößert. Frühere Studien [Dev+11] stützen diese Hypothese. Das Kapitel schließt mit der Schlussfolgerung, dass das NIEL-Modell nicht geeignet zu sein scheint, die durch langsame Neutronen in CMOS Sensoren induzierten Schäden durch nicht-ionisierende Bestrahlung zu quantifizieren und vorherzusagen. Alle Ergebnisse des Kapitels wurden in [Lin+17] veröffentlicht.

Im letzten und achten Kapitel wird der Strahlenschaden an CMOS MAPS durch schwere Ionen untersucht. Der nicht-ionisierende Strahlenschaden nach NIEL war für relativistische Schwerionen weitgehend unbekannt: In [Xap+04] und [Mes+03] werden Berechnungen zum NIEL für hochenergetische schwere Ionen mit der Ordnungszahl Z von bis zu 26 (Fe/Eisen) mit Energien zwischen 200 MeV bis 2,1 GeV pro Nukleon in Silizium gezeigt. Zu Strahlenschäden durch Schwerionen höherer Ordnungszahlen konnten in der Literatur weder theoretische, noch experimentelle Angaben gefunden werden.

Es ist jedoch wichtig den erwarteten Schaden abzuschätzen, um die Sensoren nah am Strahlengang in Schwerionenexperimenten einsetzen zu können. Hierzu wurden vier MIMOSA-34 THR-CPS am CERN-SPS Pb-Ionen mit einer Energie von 30 AGeV ausgesetzt. Während des zweiwöchigen Betriebs wurde ein maximaler Ionenfluss von bis zu $1{,}2 \cdot 10^{10}$ Pb Ionen pro cm^2 von den Sensorchips absorbiert. Die bestrahlten Sensor werden mit identischen MIMOSA-Sensoren mit bereits bekannten Volumenschäden verglichen. Dabei wird angenommen, dass eine vergleichbare CCE einer vergleichbaren Strahlendosis in Einheiten von $\mathrm{n_{eq}/cm^2}$ entspricht.

Die durchgeführte Analyse der Sensoren weist auf einen Strahlungschaden von weniger als $3 \cdot 10^{12}\ \mathrm{n_{eq}/cm^2}$ hin, dies entspricht einer oberen Schranke von $\mathrm{k}_{ion} < 300$ $\mathrm{n_{eq}/cm^2}$ für den Härtefaktor für 30 AGeV Pb-Ionen. Die Sensoren zeigen weder einen Anstieg des Rauschens noch nennenswerte durch nicht-ionisierende Strahlung entstandene Volumenschäden. Die Ergebnisse wurden zuerst in [LDB16] präsentiert und später in [Dev19] einer breiten Öffentlichkeit zugänglich gemacht.

Zur systematischen Durchführung der für diese Arbeit benötigten Versuchsreihen wurde eine eigens dafür entwickelte Software-Lösung genutzt [Lin14a]. Details zum Messaufbau kann der interessierte Leser in Anhang B nachlesen.

In dieser Arbeit wurden die Schäden durch nicht-ionisierende Strahlung an Sensoren unterschiedlicher Generationen untersucht. Dabei wurden für jede untersuchte Generation unterschiedliche Aspekte des Sensordesigns näher betrachtet. Die 3T-Pixel der älteren MIMOSA-19-Sensoren erlauben eine genaue Vermessung des Leckstroms. Dieser Leckstrom gab Aufschluss über die Auswirkungen der neutroneninduzierten Spaltung der Bor Dotierung durch langsame Neutronen. Die untersuchten MIMOSA-34-Sensoren weisen 30 Untermatrizen pro Chip auf, jede

Submatrix mit einer anderen Kombination von Parametern, Details siehe Tabelle 4.1. Des weiteren wurden die Sensoren mit unterschiedlichen Epitaxieschichtdicken und Typen hergestellt. Diese Sensoren waren besonders gut geeignet, die Sensorleistung in Abhängigkeit von mehreren Designparametern zu untersuchen, um explorativ ein Optimum der Parameter zu finden. MIMOSA-34 THR-Sensoren wurden mit Blei-Ionen bestrahlt, um mögliche Schäden durch schwere Ionen in einem Schwerionenexperiment abschätzen zu können. Die Auswirkungen der aktiven Verarmung des Sensorvolumens wurde an drei Generationen von Sensoren untersucht: An MIMOSA-34, als auch an modernen, speziell zum Depletieren entwickelten Pegasus- und Pipper-2-Sensoren. So konnten wir im Rahmen dieser Arbeit ein tieferes Verständnis über die Auswirkungen von nicht-ionisierenden Strahlenschäden an CPS aufbauen, als auch Strategien aufzeigen wie mögliche Schäden reduziert werden können. Diese Fortschritte konnten aktiv dazu beitragen, das Sensordesign zu verbessern und werden auch dazu beitragen, dass die CPS-Technologie in zukünftigen Detektoren eingesetzt wird.

Thesis overview

In particle accelerators, nucleons collide, breaking into their elementary constituents – quarks and gluons – and very briefly forming the primordial matter that filled the universe right after the Big Bang. The hot reaction zone expands at almost the speed of light after the collision, then cools down and condenses into a variety of ordinary matter particles. Particle detectors detect these particles and determine their multiplicity, type, mass, energy, and direction to gain insight into the properties of matter at such extreme conditions.

The sensors required for this purpose must meet high standards. CMOS[1] Monolithic Active Pixel Sensors (CPS or CMOS MAPS) are commonly used; they are cost-effective and highly sensitive, have a low material budget, and are theoretically well-suited for tracking charged particles. However, the radiation tolerance of CPS was restricted. Intensive studies on CPS's radiation hardness have improved these limitations by several orders of magnitude in recent years.

This thesis investigates the radiation tolerance of several CPS developed by the Institut Pluridisciplinaire Hubert Curien (IPHC) in Strasbourg. The thesis is organized into eight chapters. The first three chapters introduce a general motivation, the theoretical foundation of the thesis, and the methodology used to study the radiation hardness of CMOS MAPS. Throughout these chapters, existing concepts are extended to investigate novel sensors featuring an actively depleted volume.

The fourth chapter describes the results of experiments on improving CPS performance with different epitaxial layers. The effects of different epitaxial layer thicknesses and specific doping profiles on charge collection efficiency (CCE) and signal-to-noise (S/N[2]) ratio were investigated. To allow for comparison to previous studies, methods based on previous work and the extended measurement method "Volume fractions of charge collection" [Doe15, p. 86] were applied. Austria Micro Systems (AMS) 0.35 µm manufactured sensors were compared to sensors manufactured in a TowerJazz[3]-0.18 µm manufacturing process; thickness and epitaxial layer doping were varied for each sensor. Compared to the older 0.35 µm sensors, the 0.18 µm sensors had significantly higher CCE and radiation hardness and thus represent a successful successor. The improved epitaxial layer partly explains the increase in CCE. 0.18 µm manufactured MIMOSA[4]-34 sensors with 18 µm, 20 µm and 28 µm thick epitaxial layers were irradiated with Fe-55[5] α and Sr-90[6] γ sources to investigate the novel epitaxial layers in more detail. Because the sensitive volume of the MIMOSA-34 sensors was not fully depleted, the signal charge collection was performed not only by the electrical field in the partially depleted sensing volume, but also by drift fields between layers of different doping concentrations.

---

[1] **C**omplementary **M**etal-**O**xide-**S**emiconductor

[2] **S**ignal-**N**oise-Ratio

[3] CMOS-Process by the manufacturer **Tower**-Jazz with a minimum structure size of **0,18**µm

[4] **M**inimum **I**onizing Particle **MOS** **A**ctive Pixel Sensor

[5] **Fe**rrum-(Iron)-Isotope with a mass number of **55**

[6] **Sr**ontium-Isotope with a mass number of **90**

The results demonstrate that high-resistance epitaxial layers with a thickness of 18 µm and a distinct "ramp" doping profile perform better than comparable sensors with other epitaxial layer thicknesses and profiles.

The fifth chapter investigates irradiated MIMOSA-34 prototype sensors to find the best combination of sensor design properties for optimizing non-ion radiation hardness. The epitaxial layer doping profile examined in the previous chapter was among the parameters studied, as were variations in pixel and diode size. The smallest investigated pixels had an effective pixel pitch of 26.9 µm, and the largest had an effective pixel pitch of 46.7 µm. The diode areas ranged from 1 to 15 μm^2. The 18 µm MIMOSA-34 sensor could sustain adequate CCE after mild irradiation with $10^{13}\,n_{eq}/cm^2$. Even after exposure to $10^{14}\,n_{eq}/cm^2$, the 18 µm thick sensor showed a higher CCE than sensors with other epitaxial layers. Sensors that were manufactured with the TowerJazz-0.18 µm manufacturing process and that had an 18 µm-thick epitaxial layer outperformed comparable sensors in terms of CCE, S/N ratio, and hardness against non-ionizing radiation. The 18 µm thick MIMOSA-34 P1 pixel matrix with a pixel pitch of 33 µm and a diode surface of 8 μm^2 reached a non-ionizing radiation hardness of up to $10^{14}\,n_{eq}/cm^2$ when cooled to $-60\,°C$. At the time of the experiment, this was the highest achieved radiation hardness value for this pixel size.

The sixth chapter investigates the effects of depleting the active sensor volume and introduces novel measurement techniques, as well as theoretical and experimental results. An analytical model, as derived in Appendix A, was used to better understand the influence of depletion voltage on sensors with small collection diodes. This model is compared to experimental measurements of MIMOSA-34 sensors and TCAD[7] simulations in subsection 6.3.1. The MIMOSA-34 sensor examined in the previous chapter features a P13 pixel matrix, which allows for limited depletion with an external voltage source of up to 9 V. The influence of depletion voltage on the depleted volume was much smaller than expected from an abrupt PN junction. The analytical model predicted a slow increase in depletion radius, determined by the sixth root of the applied voltage. This shallow slope should not be misinterpreted as saturation and perceived as a sign of full depletion. Both the analytical solution and the TCAD simulation could reproduce the measured depletion volume consistently and predicted a partial depletion.

Despite not attaining full depletion, the measured CCE improved significantly, increasing from 29.4 % to 43.8 % at an applied voltage of 8.3V. The volume fraction of charge collection presented in Figure 6.6 shows that the P13 pixel matrix of the MIMOSA-34 sensor collected signal charge more efficiently due to active depletion. The percentage of Fe-55 hits registered with CCE $\geq 40\,\%$ increased from 28.4 to 66.9 %.

Full depletion of the active volume was achieved by equipping the next generation of sensors with larger collection diodes. Independent analyses of the calibration peak position, leakage current, and multiplicity of pixel clusters indicate that the active volume of a Pipper-2 sensor was largely depleted for depletion voltages

---

[7] **T**echnology **C**omputer **A**ided **D**esign

above 10 V. The voltage required to achieve full depletion increased with the non-ionizing radiation dose. Results reported in section 6.5 show that Pipper-2 sensors can tolerate a non-ionizing radiation dose of up to $5 \times 10^{14}\,\mathrm{n_{eq}/cm^2}$ at a pixel pitch of 22 µm, provided the sensor is sufficiently cooled and depleted with 20 V.

The seventh chapter analyzes possible radiation damage beyond the NIEL model. The active volume of CPS is usually p-doped with boron, while the Non-ionizing energy loss hypothesis (NIEL) used to calculate the total non-ionizing radiation dose assumes pure silicon. Preliminary calculations indicated that the fission products of the decayed boron could cause additional unpredicted radiation damage. Simulations suggested that boron could decay into lithium and helium creating an additional 2.8 MeV of total kinetic energy. These fission ions may cause additional bulk damage. Nevertheless, the experimental results showed excessive acceptor removal and an increase in the sensor's CCE. This observation suggests that cold, fast neutrons generate traps with different properties. The NIEL model appears ill-suited to parametrize or predict the non-ionizing radiation damage slow neutrons induce on CMOS sensors. All results of this chapter were published in [Lin+17].

In the eighth chapter, the radiation damage to CMOS MAPS by heavy ions is examined. In [Xap+04] and [Mes+03], calculations are shown for the NIEL of high-energy heavy ions with atomic number Z of up to 26 (Fe/iron) at energies between 200 MeV to 2.1 GeV per nucleon in silicon. Neither theoretical nor experimental data on radiation damage caused by heavy ions of higher atomic numbers could be found in the literature. However, estimations of the expected damage are vital for operating the sensors near the beam lines of heavy-ion experiments. Four MIMOSA-34 THR[8] CPS were exposed to 30 AGeV Pb-ions at the CERN[9]-SPS[10]. During two weeks of collider operation, a maximum ion flux of 1.2×10^{10} Pb ions per cm^2 was absorbed by the sensor chips. The presented analysis of the sensors indicates a radiation damage of less than $< 3 \times 10^{12}\,\mathrm{n_{eq}/cm^2}$. This corresponds to an upper limit of $\mathrm{k}_{ion} < 300\,\mathrm{n_{eq}/cm^2}$ for the hardness factor. The sensors showed neither an increase in noise nor significant non-ionizing bulk damage. These results were published in [Dev19] and presented in [LDB16].

A dedicated software tool-stack was developed to carry out the systematic measurements and experiments described in this thesis [Lin14a]. More details can be found in Appendix B.

For this thesis, the damage caused by non-ionizing radiation on sensors of different generations was investigated. Different aspects of sensor design were examined for each generation. The results offer a deeper understanding of the effects of non-ionizing radiation damage on CPS and reveal strategies to reduce this damage. These findings have actively contributed to sensor design improvements and to the continued use of CPS technology in particle detectors.

---

[8] **T**ower-Jazz sensors with a **H**igh **R**esistivity epitaxial layer

[9] **C**onseil **E**uropéen pour la **R**echerche **N**ucléaire

[10] **S**uper **P**roton **S**ynchrotron

Contents

Chapter 1

The Compressed Baryonic Matter experiment

> *"No amount of experimentation can ever prove me right; a single experiment can prove me wrong."*
>
> ALBERT EINSTEIN

The Compressed Baryonic Matter Experiment (CBM) will explore the phase diagram of nuclear matter at energies between $\sqrt{s_{NN}} = 2\,\mathrm{GeV}$ and $4.9\,\mathrm{GeV}$ and at large baryochemical potentials above $\mu_B > 500\,\mathrm{MeV}$. This experiment will be situated at the future Facility for Antiproton and Ion Research (FAIR), which is currently under construction. Figure 1.2 presents some important components of the FAIR. In the following section, I provide a short overview of the CBM experiment, FAIR, and the MVD[1] foreseen in CBM.

1.1 CBM

Rare probes can provide insight into the properties of dense nuclear matter, but detecting these rare probes and deducing the related observables requires sophisticated statistical analysis. The CBM experiment will utilize both an unprecedentedly high interaction rate and an exceptionally sensitive particle detector. The detector will have a high-speed data readout, a large acceptance, and the ability to precisely reconstruct the secondary decay vertex of particles. [Abl+17] provides an overview of the counting rates of other experiments, both ongoing and planned, conducted at high values of baryon chemical potential. Figure 1.1 utilizes this data.

The CBM experiment will run at interaction rates up to three orders of magnitude higher than any other existing or currently planned heavy-ion experiment [Fri16]. This is crucial for detecting the rare probes of interest for the CBM.

---

[1] **M**icro**v**ertex**d**etector

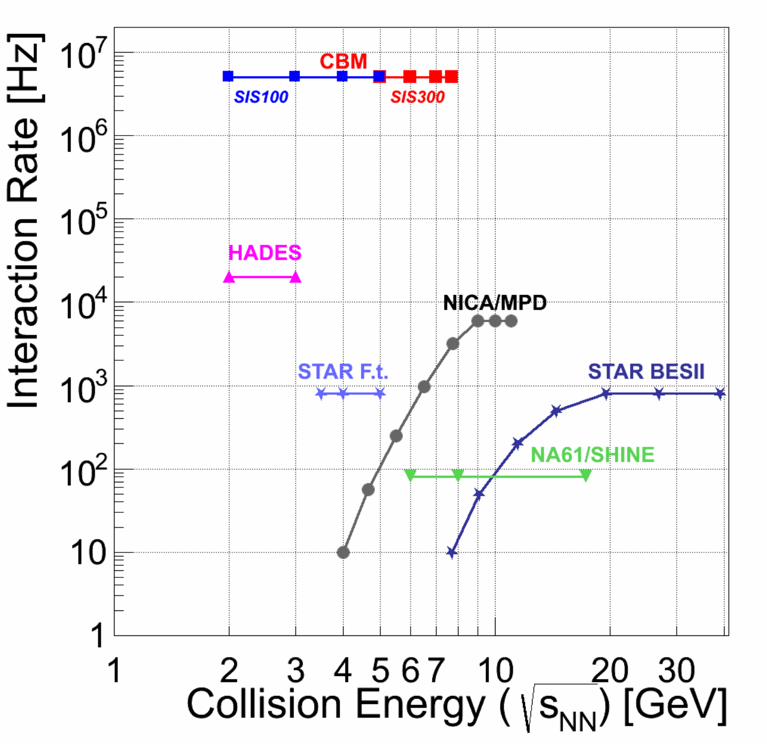

Figure 1.1: Comparison of interaction rates and center-of-mass collision energies for existing and planned fixed-target experiments [Heu16].

The flow of identified particles will be compared with theoretical models to estimate the viscosity of the produced medium. Fluctuations in the higher moments of event-by-event multiplicity distributions of conserved quantities will be used to observe phase transitions of the nuclear medium. Changes in the multiplicity of multi-strange hyperons might be used to study the chiral symmetry restoration. Precise dilepton invariant mass spectra will be used to evaluate competing dilepton production models, while the early-stage production of particles containing charm quarks will be used to test the theory of quantum chromodynamics (QCD[2]) [Abl+17].

The two experiments, CBM and HADES[3] will provide data for the study of dense hadronic matter. Thank to its large polar acceptance angle, HADES will be used for reference measurements at low energies and moderate particle multiplicities [Str17]. CBM is designed to run at high interaction rates of up to 10 MHz over all of the predicted center of mass-energy range for gold nuclei ($\sqrt{s_{NN}} = 2-$4.9 GeV) [DSa18]. CBM also features a multi-purpose detector capable of measuring and identifying hadrons, electrons, and muons over the full energy range of SIS100. Section 1.2 provides a more sophisticated overview of the experimental setup for the CBM and the FAIR project.

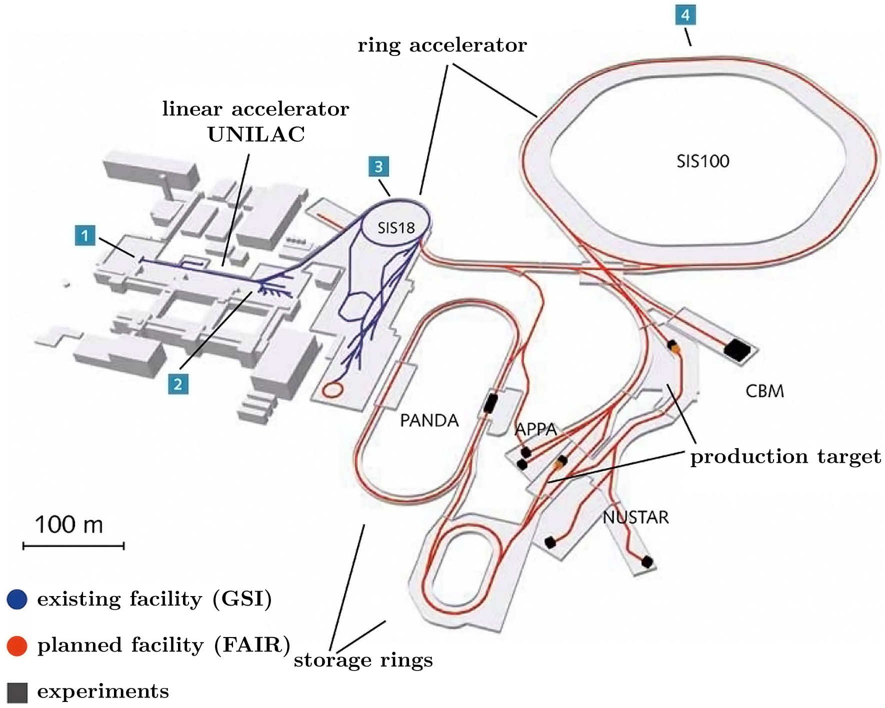

Figure 1.2: A plan of the future FAIR facility. Translated and taken from [FAI16].

1.2 FAIR

The upcoming FAIR research facility will be located in Darmstadt. At this unique particle accelerator facility, scientists will recreate conditions similar to those of nuclear matter immediately after the Big Bang and in neutron stars. To do this, they will direct beams of fast-moving particles at a fixed target to produce high-energy collisions.

The large accelerator ring, SIS100[4], will have a circumference of 1083 m [SF06]. The structure will resemble a hexagon with six straight and six curved segments. Recently developed high-tech superconducting magnets will be used to direct and hold accelerated particles on their trajectory in the ring. A two-second acceleration cycle is planned in order to reach the extremely high beam luminosity needed for high collision rates of SIS100. Because the magnets must be initiated with 4 Tesla per second, they will be subject to heating by edgy currents [Kes+13]. The magnets will reach a maximum field strength of 1.9 Tesla[5] within a half-second which is possible due to superconductivity and a cooling system that will maintain 4 K during operation [Smi+14]. Along the SIS100 beam line, 108 of these dipole magnets, each with a length of 3 m and a weight of more than 3 t, will be installed [FAI17], and 82 % of the beamline will have a temperature of 10 K [Smi+14]. To achieve a high interaction rate, air will be evacuated from the beam pipe – the predicted pressure is between 10^{-10} and 10^{-12} mbar.

---

[2] **Q**uanten**c**hromo**d**ynamics

[3] **H**igh-**A**cceptance **D**ielectron **S**pectrometer

[4] Schwerionensynchrotron

[5] 38 000 times more than the magnetic field of the Earth.

1.3 The Micro-Vertex-Detector

The Micro-Vertex-Detector (MVD) foreseen in CBM will be used for secondary vertex determination with a resolution of ≈50 µm, for background rejection in di-electron spectroscopy, and for weak decay reconstruction. It will be operated in a vacuum next to the target under high magnetic fields. The four stations will host approximately 300 CPS, with a total power dissipation of ≈150 W. To withstand the heat this will create, the sensors will be actively cooled using an aluminum heat sink: The sensors of the first station, located about 5 cm from the target, will be mounted on highly heat conductive CVD[6] diamond, while the three stations behind it, located up to 20 cm downstream, will evacuate heat to the heat sink via TPG[7] sensor carriers. All sensors will be integrated on both sides to reach maximum detection efficiency. Passive signal processing circuit areas on one side of the sensor will be complemented with active areas on the opposite side. Figure 1.3 shows a visualization of the design. The targeted average collision rate for the MVD is 100 kHz (4 - 10 *A*GeV Au+Au collisions) or 10 MHz (up to 28 GeV p-Au collisions). To cope with potential beam fluctuations, the sensors will be built to withstand a peak collision rate three times above this average value. The expected peak particle rate is $70\,\mathrm{MHz/cm^2}$ [Dev+19].

Ultra-light and highly granular CMOS MAPS will be used for the MVD. A dedicated R&D program of the PICSEL[8] group at the IPHC in Strasbourg and the IKF[9] in Frankfurt aims to improve their radiation tolerance to meet the requirements of the CBM-MVD ($7 \times 10^{13}\,\mathrm{n_{eq}/cm^2}$ and 5 Mrad per year of operation) [Mor+20].

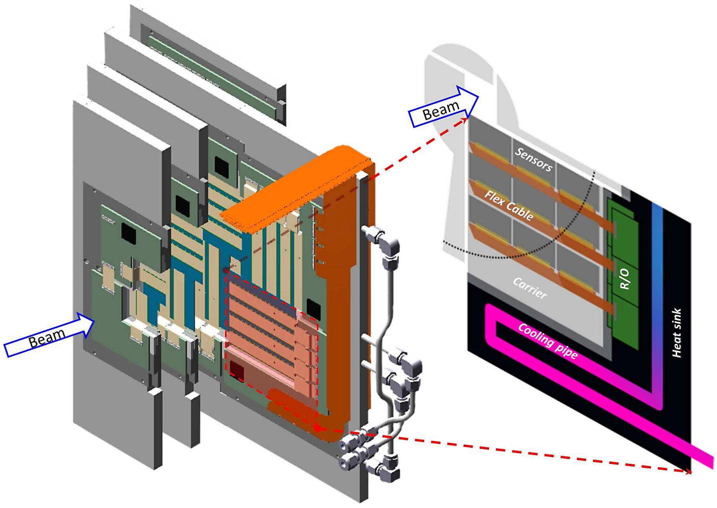

Figure 1.3: Visualization of the Micro-Vertex Detector for the CBM experiment. Only the third station is fully visible. The sensors are mounted on a TPG carrier, which is clamped into an aluminum heat sink holding read-out electronics. The heat sink has integrated cooling pipes to cool the sensors during operation. Image used with permission from Philipp Klaus [FAI19][Mor+20].

---

[6] **C**hemical **V**apor **d**eposition

[7] **T**hermal **P**yrolytic **G**raphite

[8] **P**hysics with **I**ntegrated **C**mos **S**ensors and **EL**ectron machines

[9] **I**nstitut für **K**ernphysik **F**rankfurt

Chapter 2

CMOS Monolithic Active Pixel Sensors

> *"The science of today is the technology of tomorrow."*
>
> Edward Teller

CMOS Monolithic Active Pixel Sensors (CPS) are ultra-light and granular silicon pixel detectors designed for highly accurate charged-particle tracking. Because CPS are manufactured using standard, cost-efficient CMOS processes, it is possible to combine sensing elements with both analog and digital data processing circuits on a single chip.

CPS were invented for optical imaging but were soon considered for charged particle tracking in high-energy physics. First attempts [Dep+02] demonstrated a spatial resolution of 1.4 µm at a 99.5 % detection efficiency. Later, the sensor was thinned to 50 µm to decrease multiple scattering.

Using CMOS technology to integrate an active amplifier and a photodiode into each pixel reduces the cost and the production complexity. If readout electronics are also integrated onto the sensors, they are called "Monolithic" Active Pixel Sensors (MAPS). The monolithic approach offers advantages in the assembly, cost, and detector capacitance, especially when compared to the third kind of technology often used in high-energy physics – the hybrid pixel sensor. In a hybrid pixel, the sensor matrix and readout electronics are implemented in two separate silicon pieces, with bump bonding connecting the two layers. CMOS MAPS have better spatial resolution due to smaller pixels, lower cost due to standard technology and no bump bonding, and lower noise due to smaller capacitance at the signal input. Due to this high granularity, current CPS offer excellent spatial resolution at the µm scale. They have good signal generation with conventionally some ten-micrometers thick active volumes, resulting in an ultra-low material budget $\approx 0.05\,\%\,X_0$ for a single sensor. Implementing readout electronics on the chip, as mentioned above, allows for simplifying the downstream electronics and enables installation of the sensors in previously unreachable applications.

However, CMOS technology-based sensors have lower radiation tolerance than hybrid pixels: R&D[1] for CMOS MAPS is primarily driven by exploiting currently available industrial processes, which are not optimized for radiation hard particle detection sensors. As a result, intense research was needed to increase the radiation hardness of CMOS sensors to a competitive level.

Today, CMOS MAPS are integrated into beam telescopes to provide precision tests at DESY[2] and are also integrated into the micro vertex detector for NA61/SHINE[3], the Heavy Flavor Tracker (HFT) for STAR[4] [Con+15], and the Inner Tracking System (ITS) for ALICE[5] [Col14]. Moreover, they are considered for future projects like the International Linear Collider (ILC), the upgraded tracker of the ATLAS[6] detector, and the CBM experiment [DH14]. This chapter of the thesis presents an overview of studies on the technology and radiation hardness of CMOS MAPS.

2.1 Silicon

Two interlocked face-centered cubic (FCC) sub-lattices form a silicon crystal. The sub-lattices are displaced by one-quarter of the distance along the diagonal. Figure 2.1a shows a planar projection. All of the atoms in the pure silicon lattice are of the same element. Because silicon has four valence electrons, each atom can connect to four neighbors. In a silicon crystal, these neighbors belong to the other FCC sub-lattices.

Figure 2.1b depicts a two-dimensional schematic representation of the bonds formed in an ideal silicon crystal. Each covalent bond connecting silicon atoms consists of two electrons from two distinct atoms. Silicon atoms share their four valence electrons with four surrounding atoms in this way. In the image, each dot connecting two silicon atoms represents an electron being shared. These electron are available for conduction and leave a free place or a hole in the regular lattice structure.

2.1.1 Energy bands

In a crystal, the atoms are firmly arranged in a lattice, and the individual electron energy states overlap. Quantum mechanical calculations show that this causes the electron energy levels to degenerate, forming energy “bands” [Lut07].

---

[1] **R**esearch & **D**evelopment

[2] **D**eutsches **E**lektronen-**Sy**nchrotron, research center in Hamburg

[3] **S**PS **H**eavy **I**on and **N**eutrino **E**xperiment, experiemnt at the SPS

[4] **S**olenoidal **T**racker **A**t **R**HIC, experiment at **R**elativistic **H**eavy **I**on **C**ollider (RHIC)

[5] **A** **L**arge **I**on **C**ollider **E**xperiment, Heavy ion experiment at the **L**arge **H**adron **C**ollider (LHC)

[6] **A** **T**oroidal **L**HC **A**pparatu**s**, experiment at the LHC

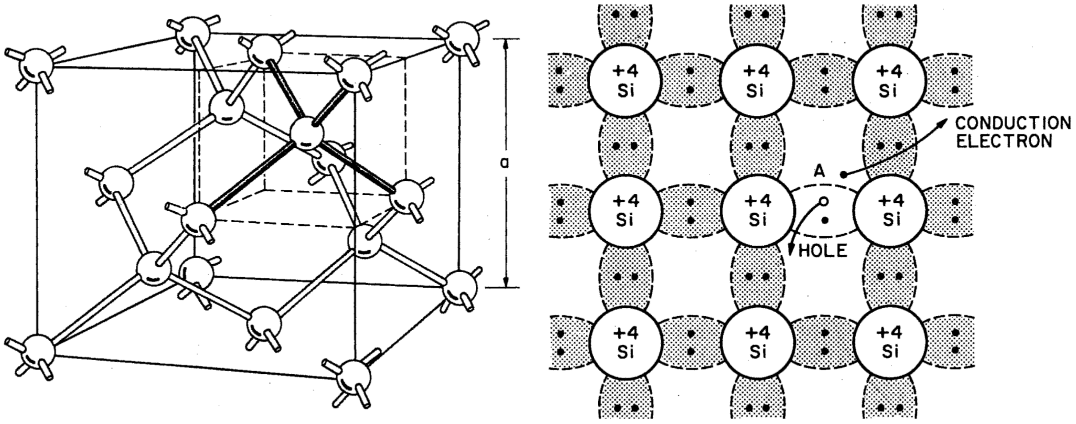

(a) (b)

Figure 2.1: A visualization of the silicon lattice (a) and a schematic representation of the covalent bonds between the silicon atoms (b) [Lut07].

$$f\left(E\right) = \frac{1}{1 + \exp\left(\frac{E - E_F}{k_B T}\right)}$$

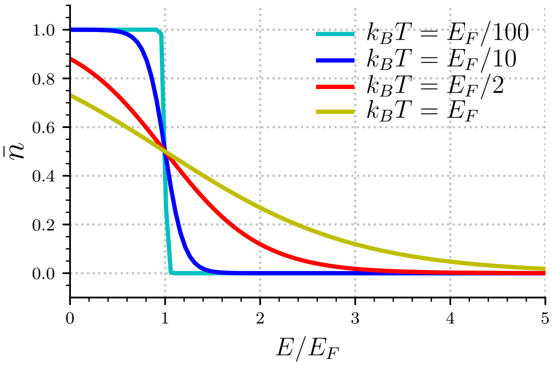

Figure 2.2: Fermi-Dirac probability distribution for various temperatures.

The distribution of electrons within the bands of a semiconductor is highly temperature-dependent. At a temperature of 0 K, all valence electrons remain in their places within the lattice. At higher temperatures, thermal vibrations break some of the covalent bonds, and valence electrons become free, creating electron/hole paris. Both electrons and holes are available for conduction; the charge-carrying electrons are in the conduction band, while the holes are in the valence band [Lut07]. The Fermi-Dirac distribution in figure 2.2 denotes the probability $f(E)$ of a state with energy E being occupied. In the equation, k_B is the Boltzmann constant[7], T is the absolute temperature, and E_F is the energy of the Fermi level.

A Fermi Level represents electrons' total electrochemical potential and is defined as an energy level at which the occupation probability is 50 %, when in thermodynamical equilibrium. In an intrinsic semiconductor, the Fermi level is located between the conduction and valence bands. For silicon, this gap is 1.14 eV at

---

[7] $k_\mathrm{B} = 8.617\,33 \times 10^{-5}\,\mathrm{eV/K}$

room temperature. Some electrons can bridge the gap and create weak conductivity. At room temperature, all materials have an almost-full valence band; only conductors have a well-occupied conduction band. In insulators, the conduction band is empty.

An average energy of 3.6 eV is required to create an electron-hole pair in silicon by means of X-ray or charged particle. This energy is approximately three times the band gap[8]. The difference between the band gap energy in silicon and the measured 3.6 eV for electron-hole pair creation is due to optical phonon losses and the residual kinetic energy from threshold effects; [AB75] described a calculation for this that included momentum and energy conservation, and [OP04] offered a detailed discussion on this effect. Most of the electrons must be promoted from deep in the valence band to high levels in the conduction band, which explains the high energy difference. The value of 3.6 eV is an average over many possible electron transitions and will be used for theoretical calculations in this thesis.

2.1.2 Doping

Doping is a process in which a small fraction of main grid atoms is replaced by atoms with a different number of valence electrons. This process is used to supply semiconductors with a controlled number of charge carriers.

For example, when a phosphorus atom is integrated into the silicon crystal lattice, the fifth valence electron of the atom cannot form a covalent bond with the surrounding silicon atoms and is therefore surplus. The quasi-free electron will appear as a filled state just below the conduction band (figure 2.3 for a schematic sketch). This electron can be transferred into the conduction band with little thermal energy and becomes a charge carrier. A material doped in this way is called n-doped and the foreign atoms are called donors since they provide an additional electron to the lattice. Charge carriers obtained by doping are called majority carriers, in contrast to the thermally generated minority charge carriers.

p-typed material is created by doping with atoms that have one valence electron less than the major grid atoms. For example, boron has three valence electrons and can replace a silicon atom, which has four valence electrons; this creates empty states close to the valence band. As a result, holes are generated, as discussed in section 2.1.1. These holes can effectively be treated as majority charge carriers.

By combining semiconductors of opposite doping, a PN junction is formed. This type of structure forms a diode, primarily conducting current in only one direction (see Figure 2.5). A remarkable feature of the PN junction is the formation of a space-charge zone (also known as a depletion layer) with no free majority-charge carriers. Applying an external voltage to the PN junction can change the size of

---

[8] The empirical formula known as the “Klein function” states: $E_{\text{pair cr.}} = {}^{14}\!/_{5} E_{\text{gap}} + 0.55$ [Kle68].

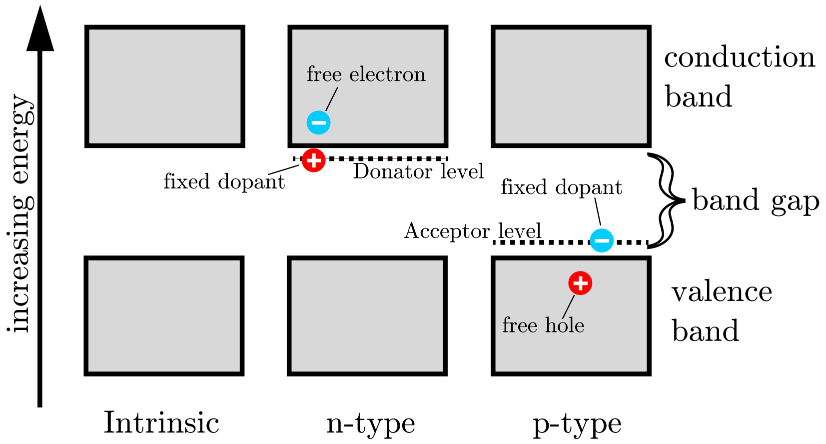

Figure 2.3: Schematic representation of an ideal intrinsic not doped semiconductor, an n-doped and on the right side, a p-doped semiconductor.

the depleted region. Such a construction occurs in many electrical components of semiconductor technology, as well as in CMOS MAPS (as described in section 2.3).

The image above has its limitations. To realistically describe semiconductors, the complex band structure must be considered in three dimensions, and direct and indirect band gaps must be differentiated. The literature contains a more detailed description of this topic is found in [Lut07][Sze85].

2.2 Interaction of silicon and radiation

The total number of available signal electrons in a silicon detector depends on the trans-passing particle, as well as the thickness of the sensing volume. This number is proportional to the mean energy loss in the sensor or, alternatively, the stopping power in the active volume. The Bethe-Bloch formula [Sig14] describes this relation (see Figure 2.4). This energy loss value is usually near the minimum for high-energy physics experiments. As the energy loss values around this minimum are approximately the same for differently charged particles, particles with energy in this region are often grouped and collectively called minimum ionizing particles (MIP[9]s). MIPs generate an average ≈80 electron-hole pairs per pervaded µm in silicon. Thus, the total number of available signal electrons depends primarily on the particle trajectory length through the sensing volume. A more substantial number of collected electrons simplifies the amplification and discrimination of the signal from noise, so a thicker active volume seems beneficial. However, a overall thicker sensor causes additional multiple scattering of the incident particle; this distorts the trajectory, though vertex detectors can

---

[9] **M**inimal **I**onizing **P**article minimum ionizing particle, a hypothetical particle with the lowest energy loss in matter, conventionally pions are used in experiments as MIPs

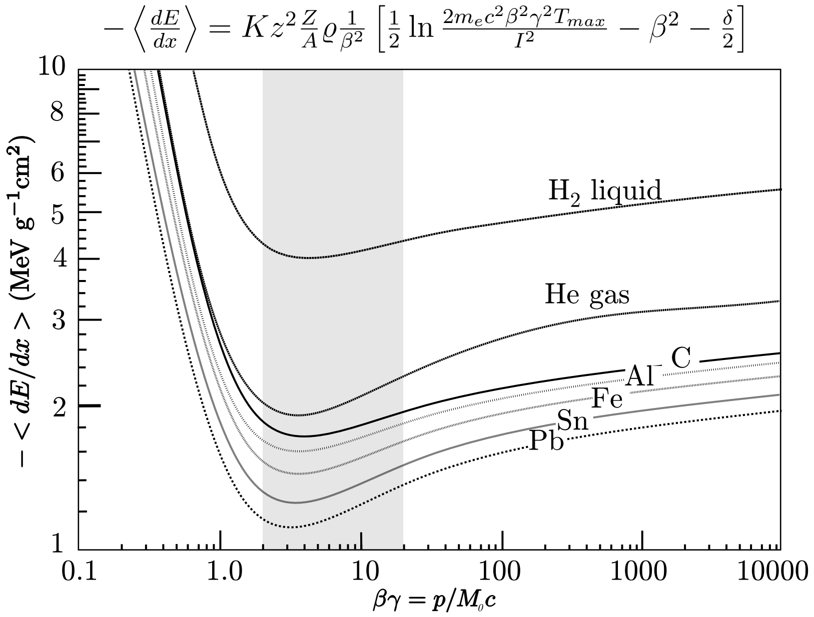

Figure 2.4: The Bethe formula and its plot for various materials. On the abscissa, the term $p/(M_0c)$ is shown. For light particles at the speed of light, when $M_0 << E$, like for muons and pions, the momentum p is approximately E. The gray region denotes the area of minimal interaction – particles in this range are called MIPs. Pions with energy between 300 MeV $< E_\pi <$ 3 GeV and muons with energy between 200 MeV $< E_\mu <$ 2 GeV are in this minimum interaction range [Par16].

counteract this distortion somewhat through trajectory preservation and reconstruction methods. As such, researchers must balance having the lowest possible material budget with generating a sufficiently large number of electrons.

2.3 Sensor diodes

Although fabricated single crystalline silicon is considered the purest material in existence [Era14][Föl16], it still has imperfections, which can act as recombination centers for signal electrons. In theory, pure silicon has an equal number of excited electrons and holes which would make it an intrinsic semiconductor. Conversely, a semiconductor with an imbalance in the number of free electrons and holes is an extrinsic semiconductor. Intrinsic configurations are advantageous due to their lower signal-electron recombination rates and lower dark currents at room temperature, but it is not yet possible to produce sufficiently pure intrinsic semiconductors. To overcome this, PN junctions are used for collection as they block the majority charge carriers generated by impurities, but are transparent for the minority charge carriers created by impinging particles. This technique enables the use of impure silicon for efficient charge collection.

When two extrinsic semiconductors of opposite doping are joined, an exchange of free majority charge carries occurs between the two parts. Electrons diffuse into the p-region, and holes from the p-doped piece diffuse into the n-type material. Prior to this migration, the materials are electrically neutral; after the migration, there is a net negative electrical charge within the p-region and a net positive charge within the n-region. This disparity creates an electrical field that prevents further diffusion. The electrical field also affects the thermally excited mobile charge carriers in the region between the two junctions (see Figure 2.5), which creates a space-charge-free region with no majority charge carriers. This region is called the depleted volume.

The width of the depleted region primarily depends on the doping concentrations of the semiconductors involved. Heavily doped silicon has a large number of free charge carriers, and so the net electrical charge density is high. This shrinks the depleted region in a heavily doped material.

The difference in potential between the two sides is called the barrier potential. Its magnitude depends on the doping concentrations, and temperature. Silicon PN junctions typically have an intrinsic or built-in voltage of around 0.7 V.

A structure that allows a current to flow unidirectionally is called a diode. Diodes are a fundamental component of many electronic devices, including transistors, solar cells, power converters, voltage stabilizers, temperature sensors, optical devices, and integrated circuits. PN junctions exhibit diode characteristics; they prevent the flow of majority charge carrier electrons from the n-side and the flow of holes from the p-side, but they do not impact the flow of minority charge carriers (electrons on the p-side and holes on the n-side). These minority charge carriers, which are produced by thermal energy, are attracted to the opposite side of the barrier (i.e., electrons to the n-side and holes to the p-side). This flow is usually low and therefore neglected.

2.3.1 Diode biasing

Applying an external voltage to a PN junction is called biasing. There are two types of biasing: forward biasing and reverse biasing. If the positive pole of a battery connects to the p-type region and the negative pole connects to the n-type region, the diode is forward biased. In this configuration, a current can flow through the junction provided the build-in voltage is high enough to overcome the intrinsic voltage. If the polarity of the battery is reversed, with the p-type side connected to the negative terminal and the n-type side connected to the positive terminal, the PN junction will block the electric current from the battery; this creates a reverse-biased diode. Such a diode configuration is ghenerally used in silicon radiation detectors (see Figure 2.7).

Biasing affects the width of the depleted area. In a forwardly biased configuration, the depleted region becomes smaller. The applied voltage feeds free electrons into the n-region and holes into the p-region, which produces the same effect as

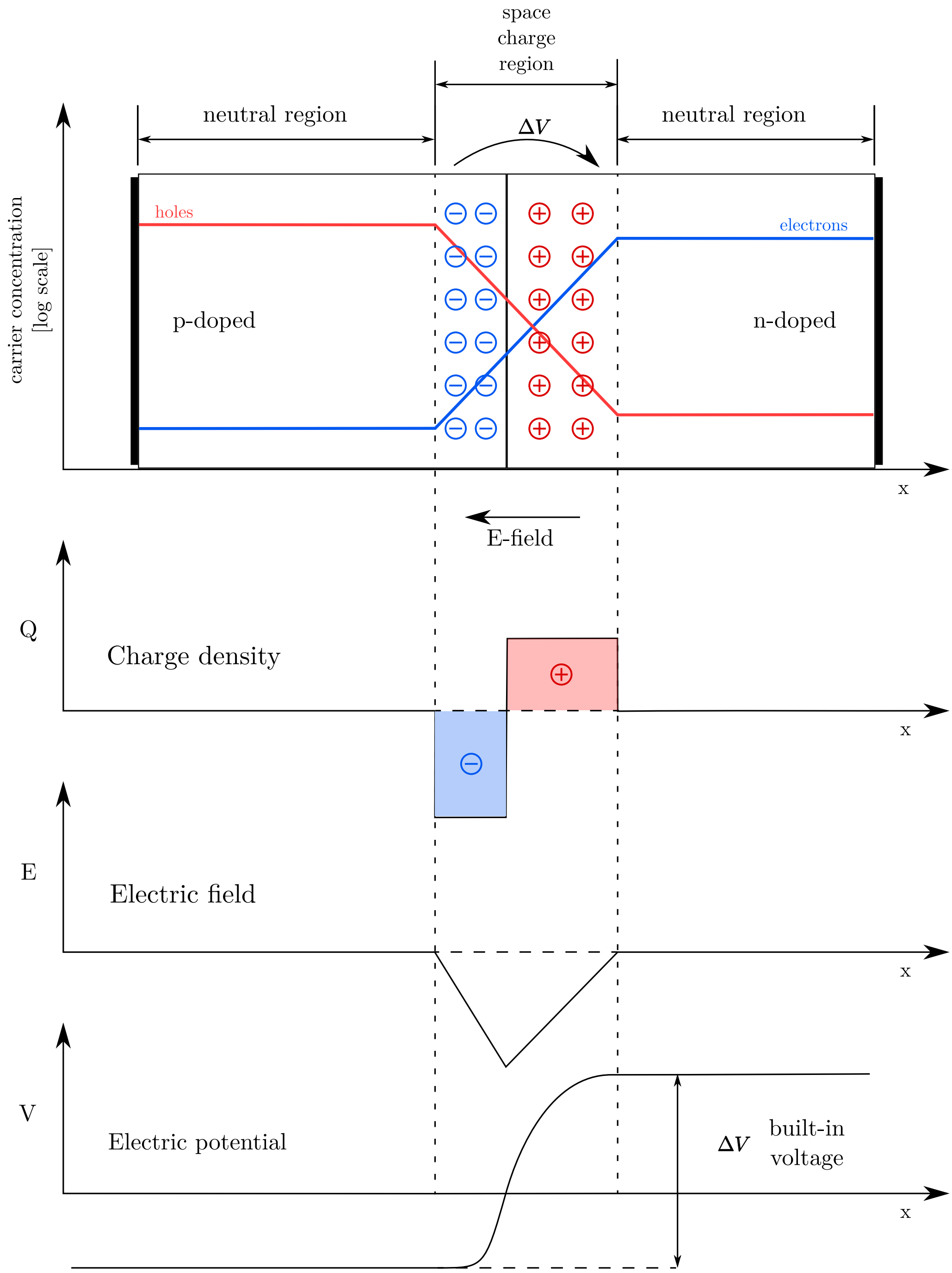

Figure 2.5: A PN junction in thermal equilibrium with a zero-bias voltage applied. Electron and hole concentrations are drawn with blue and red, respectively. Under the junction, plots for the charge density, the electric field strength, and the voltage potential are shown. Modified from [The18].

an increase in doping concentration (see Section 2.1.2). The electrical field generated by the applied voltage is in the opposite direction of the electrical field in the depleted volume. However, due to the large number of free electrons at the negative terminal of the power supply, the two fields repel each other and move from the region of higher concentration of free electrons (the n-side) to the region of lower concentration (the p-side) in the diode. At the junction, the free electron charge carriers neutralize the positive ions on the n-side of the depleted region. Simultaneously, the positive free holes in the positive terminal of the power supply move to the opposite side of the depleted region and neutralize the negative ions there. These processes continue until the depleted area and its electrical field disappears. The remaining free electron charge carriers cross the depleted region and recombine with the holes present in the p-type region, becoming valence electrons. These valence electrons pass from one atom to another and move towards the positive terminal of the power supply, while holes towards the negative terminal. This allows the applied electrical current to flow from one side of the junction to the other.

In a reverse-biased configuration, the positive terminal of a power supply is connected to the n-type region, and the negative terminal is connected to the p-type region of the PN junction; the depleted volume becomes larger, and the flow of electric current is blocked[10]. Holes from the p-type region are attracted to the negative pole, while electrons from the n-type region move towards the positive pole. This migration broadens the space-charge-free region between the two sides and extends the depleted area. Alternatively, the free electrons at the negative electrode recombine with the holes in the p-type semiconductor. This recombination creates negatively charged ions near the junction. The electrons from the n-type side of the junction recombine with the holes from the positive terminal of the power supply. This mechanism creates additional ions on both sides of the junction. The generated electrical field points in the same direction as the electrical field of the depleted region of the PN junction, counteracting the flow of majority charge carriers from the power supply. An increase in the voltage reinforces this effect because it also increases the depleted volume. Therefore, I refer to the reverse-bias voltage as depletion voltage throughout the rest of this thesis.

The reverse-biased diode blocks the flow of majority charge carriers from the power supply, but the minority charge carriers, which are generated by thermal excitation, create a negligible electrical current. This effect is known as leakage current. This drift depends on the temperature and is called reverse saturation current. If the depletion voltage increases beyond a certain value, the junction breaks down, and the current and voltage increase rapidly. This value is called the break-through voltage. Reverse-biased diodes should operate below the break-through voltage to prevent damage to the semiconductor devices.

---

[10] Up to a certain point, called the break-through voltage.

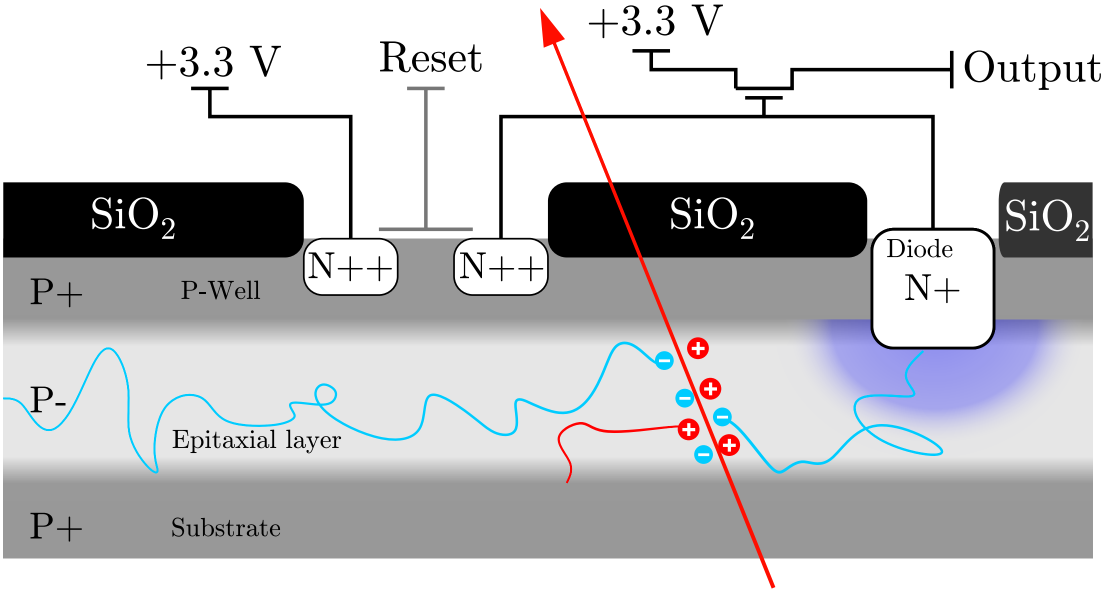

Figure 2.6: A schematic view of four layers of traditional MAPS. The gray shading indicates the p-doping density. The blue area depicts the depleted volume around the n-doped implementation. Altered graphic based on [Dev08].

In CMOS MAPS, the n-implementations embedded in the p-well above the p-type doped active volume act as charge collecting diodes. The distance between the n-type implementations is the pixel pitch or pixel size, please see Figure 2.6 for an illustration.

2.4 The design and working principles of MAPS

Figure 2.6 shows a schematic sketch of a traditional CMOS sensor layout. The bottom substrate layer is highly p-doped, with $10^{17} - 10^{20}$ dopants per cm^3, and may be thinned to a few µm. The epitaxial layer above the bottom substrate acts as the active volume. It is typically about 15 µm thick and has a lower p-doping concentration of $10^{12} - 10^{15}$ dopants per cm^3. The layer above the epitaxial layer consists of a highly p-doped p-well ($\approx 10^{17}$ p-dopants per cm^3) with embedded highly n-doped n-diff implementations. Some of these n-doped implementations are used to realize metal-oxide-semiconductor field-effect transistors.

If an electron is excited in the epitaxial layer, it is deflected by the high potentials of the substrate and the p-well, particularly the high potential between the P- to P+ transition, and is collected in the n-doped region. The readout electronics are integrated into one of the top layers. The red line in Figure 2.6 represents the trajectory of an MIP. The blue and red circles show electron-hole pairs generated along its path. The curved blue lines signify paths of the signal electrons. One signal electron is collected by the nearby n-doped diode, while the other diffuses into the neighboring pixel.

CMOS MAPS measure signal electrons that have been excited by either fast charged particles pinning through the active volume of the sensor or absorbed photons via the photoelectric effect. A PN junction, formed from a n-well (N+) implantation and the active volume of the sensor, the epitaxial layer, act as a reverse-biased

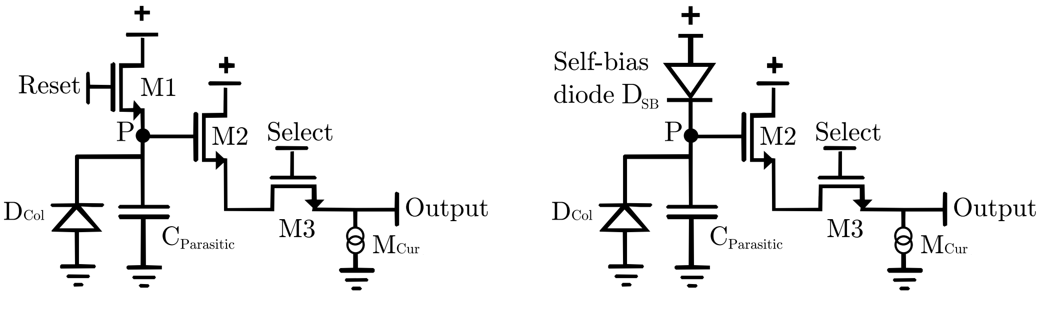

(a) 3T-Pixel (b) SB-Pixel

Figure 2.7: Circuit diagram of a 3T-Pixel (a) and an SB-Pixel (b). A 3T-Pixel consists of three transistors: the reset transistor (M1), the source follower transistor (M2), and the select transistor (M3). In an SB-Pixel, the capacitance $C_{\text{Parasitic}}$ of the collecting diode D_{Col} is reloaded by a self-biased diode D_{SB} rather than by closing the transistor M1.

diode. It collects the excited electrons from the active volume using drift fields and diffusion. The conductors and the diode act similar to a capacitor and convert the charge to voltage. A source follower transistor formed from NMOS[11] and a current source (not shown) buffers this potential. Which, generates a signal.

2.5 Methodology

A sophisticated framework has been developed to systematically carry out radiation hardness studies. A C++[12] CERN-ROOT[13] software and laboratory automation tool called the "MIMOSA Automated Bot System" (MABS) helps analyze the radiation tolerance of sensors using user-defined observables [Lin14a]. The process of data acquisition, long-term storage, measurement supervision and temperature control has been reviewed, reworked and automated. For more details on MABS and its functionality, see Appendix B (page 120).

2.5.1 Sensor signal

Figure 2.8 depicts a typical analog raw data output signal recorded from the integrated pre-amplifier of a sensor with a three-transistor pixel (3T-Pixel). The integrated pixel pre-amplifier aims to amplify the collected signals of a few hundred electrons within the pixel so that they can be transmitted and processed by the readout chain. The essential observed variables are described in the following subsections. For a detailed description of the measuring equipment and hardware, refer to chapters 2 and 4 in [Doe15] and [Dev08]. The sensor pixels studied in this thesis feature one of two amplifier types, both of which transform the gathered charge into a voltage. The older sensors have a 3T amplifier, which

---

[11] **N**-Channel-**M**etal-**O**xide-**S**emiconductor Transistor

[12] A standardized general-purpose programming language created in 1979 [Str13].

[13] An object-oriented data analysis framework developed at CERN [BR97].

consists of three transistors (see Figure 2.7a for a schematic view). This type of amplifier converts charge to voltage by accumulating electrons from the epitaxial layer at the pixel capacity $C_{\text{Parasitic}}$. The gathered electrons cause a potential drop at point P, which is registered by the gate of the source follower transistor (M2) . This buffer is needed as the limited number of gathered electrons cannot provide the necessary current to transmit a signal out of the pixel to the readout chain. The gain g of the source follower is nearly one, so the value of the capacity C determines the total resulting gain of the amplifier:

$$U_S = Q_{\text{Observed}} \cdot \frac{g}{C} \tag{2.1}$$

U_S	Transformed outgoing voltage signal
g	Gain of the source follower
Q_{Observed}	Signal charge stored by the capacitance $C_{\text{Parasitic}}$
C	Capacitance of the sensing node

As Equation (2.1) suggests, maximizing the observed voltage signal U_S requires that the overall capacitance C of the sensing node to be minimized. This capacitance is composed from the parasitic capacitances of the diode and the other amplifier components. Usually, the aim is to minimize the size of the collection diode D_{Col} and the capacity of the gate for the M2 transistor. Note that, by this strategy, the signal-to-noise (S/N) ratio is maximized, since the M2 transistor usually generates the dominating noise from the in-pixel amplifier. However, an undersized diode does not efficiently collect signal electrons, and an undersized transistor gate causes excessive random telegraph signal (RTS[14]), as [Dev+08] and [Doe08] have shown. After each readout-cycle, the reset transistor (M1) is closed, and the potential of the capacitance $\text{C}_{\text{parasitic}}$ is restored to prepare the pixel for the next integration period. The pixel is insensitive to hits during this recharging period, an undesired side-effect for a tracking detector.

The more modern self-biased pixel (SB-Pixel) operates with a continuous bias voltage and has no dead time (see Figure 2.7b for a schematic). A forward-biased diode D_{SB} replaces the M1 transistor. It compensates the leackage current of the diode and clears after some time the signal charge of impinging particles. This feature allows to operate the pixel without dead-time as needed in particle physics. However, unlike the 3T-pixel, the SB-pixel is not suited for optical imaging.

Figure 2.8 shows raw data measured using a non-irradiated 3T-Pixel. The readout cycle of a 3T-Pixel is divided into two intervals. The sensitive integration time t_{int} and the insensitive dead time, during which the capacitance $C_{\text{Parasitic}}$ of the readout diode is recharged by the reset transistor (see Figure 2.7a). The integration time t_{int} is defined as the elapsed time between two measuring points, t_{F_0} and t_{F_1}. The potential of an isolated pixel measured at time t_{F_0} is denoted U_{F_0}. Collected electrons and the leakage current lower the potential of the in-pixel capacity. After the integration time t_{int}, a new measurement of the potential,

---

[14] **R**andom-**T**elegraph-**S**ignal

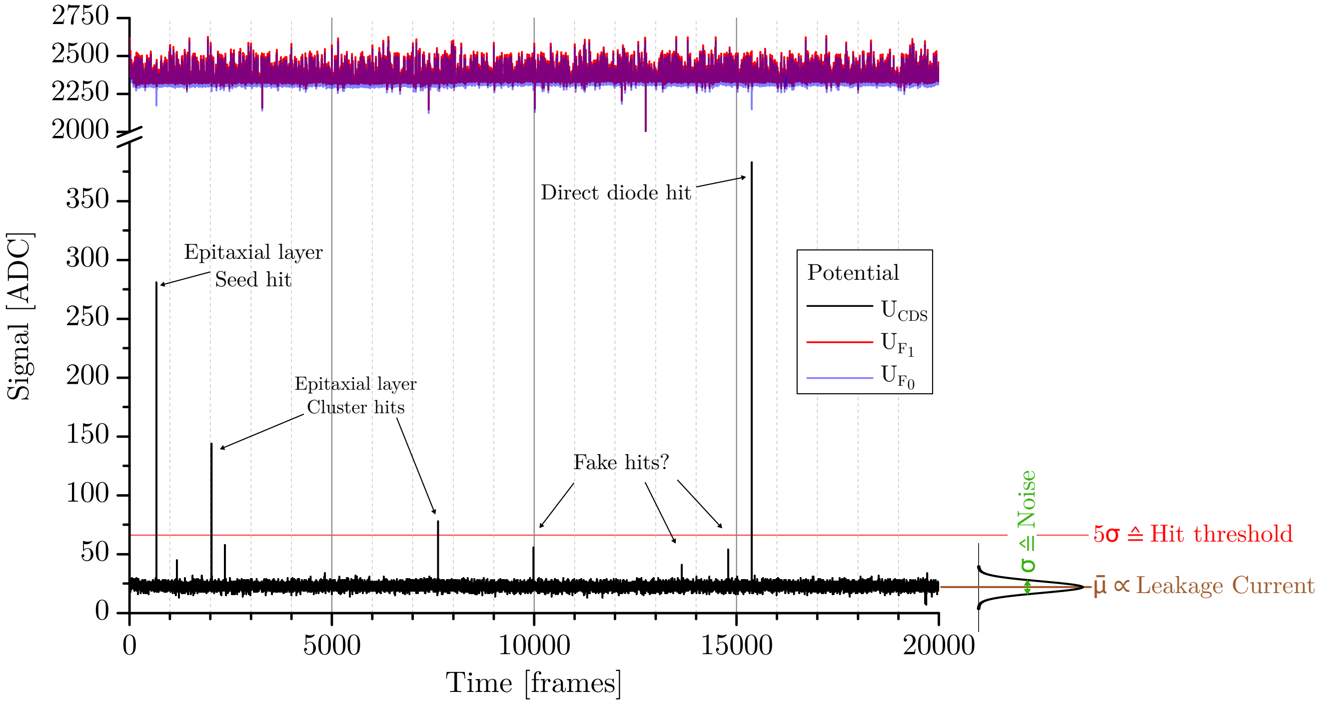

Figure 2.8: The measured potential at the analog sensor readout at two different times (t_{F_0} and t_{F_1}) for a single 3T-Pixel are shown in blue and red. The potential difference ($U_{\mathrm{CDS}} = U_{\mathrm{F}_1} - U_{\mathrm{F}_0}$) is plotted in black. The data was compiled from a non-irradiated pixel by [Doe15]. Leakage current is shown in brown, the noise is in green, and the hit threshold is a horizontal red line.

U_{F_1}, is taken before the pixel is reset. Taking the difference between the two potentials is called correlated double sampling (CDS[15]). This method is used to compensate for the pixel-to-pixel baseline dependence of the initial potentials U_{F_0} and U_{F_1}, the temporal diode noise, and possible baseline shifting after the reset in 3T-Pixels or during the recharging period in SB[16]-Pixel. The time between two independent CDS measurements is defined as the readout time $t_{\mathrm{r.o.}}$.

$$U_{\mathrm{CDS}} = U_{\mathrm{F}_1} - U_{\mathrm{F}_0}$$

The resulting CDS spectrum varies around a fixed value. In Figure 2.8, which shows data for a 3T-Pixel, this value is around 20 ADU. In a 3T-Pixel, this fixed value corresponds to the average discharge of the in-pixel capacitor during the integration time. Even if no hit is detected by the pixel within the integration time t_{int} and no signal electrons discharge the diode capacitor, dark currents from thermal excitation cause a discharge with the potential U_{F_0}. Therefore, the potential U_{F_1} recorded after the integration time t_{int} is lower than U_{F_0}, and the median CDS over multiple time frames corresponds to the median leakage current of the pixel during the recorded frames. The leakage current value is marked by a brown line and the symbol $\overline{\mu}$ in Figure 2.8. The ability of a 3T-Pixel to capture

---

[15] **C**orrelated **D**ouble **S**ampling

[16] **S**elf-**B**ias Diode

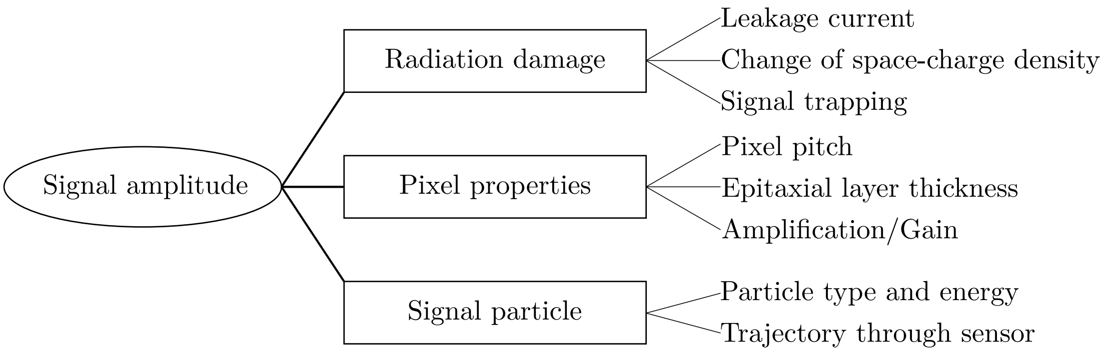

Figure 2.9: The amplitude of a signal depends on numerous factors; some are related to radiation damage effects, while others involve the technical pixel properties or the particle specifics that caused the signal.

the leakage current of the sensing volume makes makes these pixels very helpful in analyzing the radiation damage of a sensor. The standard deviation of the leakage current distribution is called noise, shown as a green σ at the width of the distribution in Figure 2.8. The figure shows the noise of a single pixel. The noise is unique to each pixel, so a distribution of noise values for the whole pixel matrix is calculated in this thesis. Though the average CDS for SB-Pixels is zero, there are time-dependent fluctuations from the median CDS value. Therefore, the noise of SB-Pixels can be determined in the same way as the noise of 3T-Pixels. Strong outliers from the base value $\overline{\mu}$ indicate hits (see Equation (2.2)). These hits were excluded from analysis to prevent distortion of the estimated noise result. In this thesis, the hit threshold for an individual pixel is defined as

$$U_{\text{hit thr.}} = \overline{\mu} + 5\sigma \tag{2.2}$$

Each pixel has its own hit threshold $U_{\text{hit thr.}}$. If the CDS value is above $U_{\text{hit thr.}}$, the pixel likely detected a hit. Figure 2.8 shows several hit signals, the amplitudes of which vary strongly. The CDS level significantly impacts the amplitude of the signal. This observable differs, especially when collected signal electrons cause a drop in potential during t_{int}. The number of electrons collected depends on multiple factors, some of which are summarized in Figure 2.9. Radiation damage has several consequences (see Section 3.3), namely an increase of leakage current, a change in space-charge density and signal electron trapping. Below, the individual consequences and their qualitative impact of signal amplitude are discussed. Leakage current impacts signal height differently for 3T-Pixel and SB-Pixels; these differences were investigated in this thesis. In 3T-Pixel, an increased leakage current increases the baseline $\bar{\mu}$ of the CDS (see Figure 2.8). Furthermore, a higher leakage current usually increases the noise value σ [Doe08] and the hit threshold $U_{\text{hit thr.}}$. Hits can fall below the raised threshold and go undetected (see Equation (2.2)). This effect can be compared to the saturation of an optical camera pixel at excessive luminance. This baseline-shifting only applies to 3T-Pixels since the recharging diode in self-biased pixels compensates the leakage current – there is no CDS baseline shift in SB-Pixels. Nevertheless, the leakage current also has an adverse effect on the signal amplitude of SB-Pixels. Higher leakage currents (I_{leak}) cause the self-bias diode D_{SB} to recharge the capacity $C_{\mathrm{Parasitic}}$ of the collecting diode $\mathrm{D}_{\mathrm{col}}$ more quickly (see Figure 2.7b for a schematic). This non-linear characteristic curve for recharging the diode D_{SB} results in faster restoration of the potential at point P (Figure 2.7b) when there is a high leakage current. Given a constant readout time $t_{\mathrm{r.o.}}$, the measured CDS is reduced, which in turn reduces the effective gain of the affected pixel (compare Figure 2.10 to 2.11).

As such, charge clearing can be observed via a shifting calibration peak in the charge spectrum; the peak also becomes broader, and eventually, the spectrum becomes uninterpretable. Because the time between the impact of an X-ray photon and the actual readout of the pixel is evenly distributed within the integration time, a random amount of remaining charge is collected, which widens the spectrum. Charge clearing is important to address because it may be misinterpreted as a loss in charge collection efficiency (CCE) from bulk damage. Accelerating the integration time is an effective technique for separating charge loss due to radiation-induced modification of the sensing volume from charge loss due to charge clearing. If the readout time is reduced significantly, the charge clearing constant τ in Equation (2.3) becomes larger than the readout time and no significant charge loss should be observed; charge loss due to signal trapping is independent of the readout frequency.

The curves in the images are calculated using the following equations, for a derivation see [Dev19]:

$$\begin{aligned} U_{\mathrm{CDS}}(t) \propto Q_{\mathrm{Observed}}(t) &= Q_{\mathrm{Phys}} \cdot \exp\left(-\frac{t}{\tau}\right) \quad \text{, where} \\ \tau &\approx \frac{k_B T C_{\mathrm{Parasitic}}}{e} \frac{1}{I_{\mathrm{leak}}} \end{aligned} \tag{2.3}$$

The following variables are used in Figure 2.10 and 2.11 and are set to these values:

Q_{Observed}	Charge measured by the readout (blue plotted line)
Q_{Phys}	Initial charge at the capacitance $\mathrm{C}_{\mathrm{Parasitic}}$ of the collecting diode $\mathrm{D}_{\mathrm{col}}$, set to 1000 a.u. (arbitrary units)
k_B	Boltzmann Constant, $1.380\,65 \times 10^{-23}\,\mathrm{m^2 s^{-2} K^{-1} kg}$
$C_{\mathrm{Parasitic}}$	Capacitance of collecting diode, set to 10 fF
T	Temperature, set to 250 K (about −20 °C)
e	Electron charge, $1.602\,176\,6 \times 10^{-19}\,\mathrm{C}$
I_{leak}	leakage current, set to 100 fA for moderate current (Figure 2.10) and to 500 fA to demonstrate the effect of a high leakage current (Figure 2.11)

Equation (2.3) calculates radiation-induced charge clearing, which plays a major role in highly irradiated SB-Pixels; I discuss this further in section 5.3 (page 74), where I investigate the S/N ratio for sensors with different diode sizes and with temperature dependance. As the clearing constant τ approaches the same order

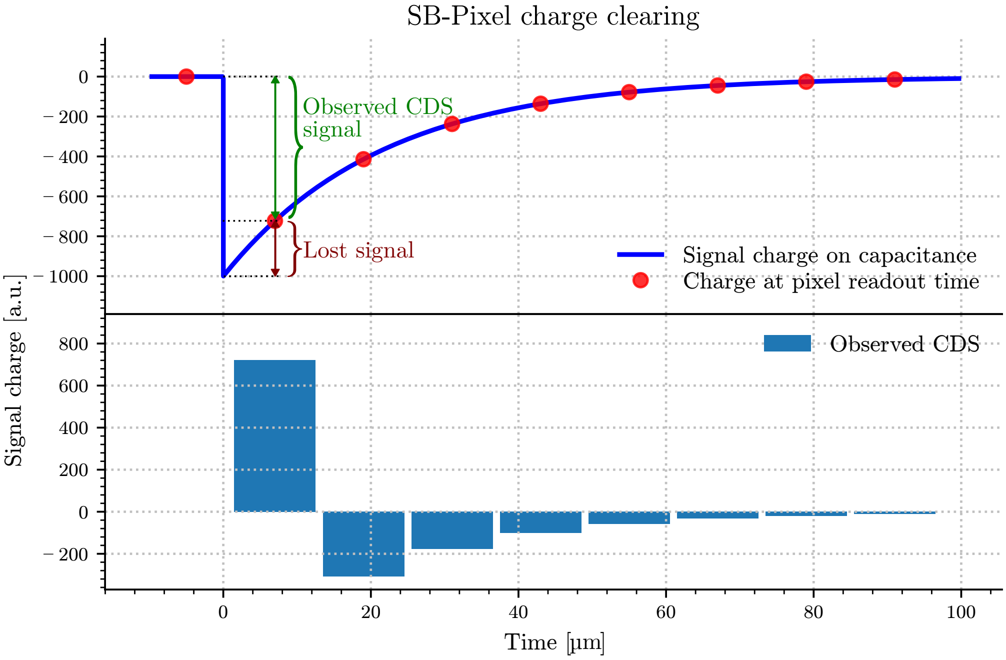

Figure 2.10: Charge clearing of an SB-Pixel with moderate leakage current. The readout time is set to $t_{\text{r.o.}} = 12\,\mu\text{s}$. A hit happens at time $t_{\text{hit}} = 0\,\mu\text{s}$ and is read out at time $t_{\text{coll.}} = 7\,\mu\text{s}$. The observed CDS spectrum is displayed beneath the declining signal charge curve. The changes in the sign of the CDS signal at 7 and 19 µs is noteworthy; they may be used as an indicator of hit detection. A period of recharging occurs after a high CDS signal amplitude, and then the CDS becomes zero again.

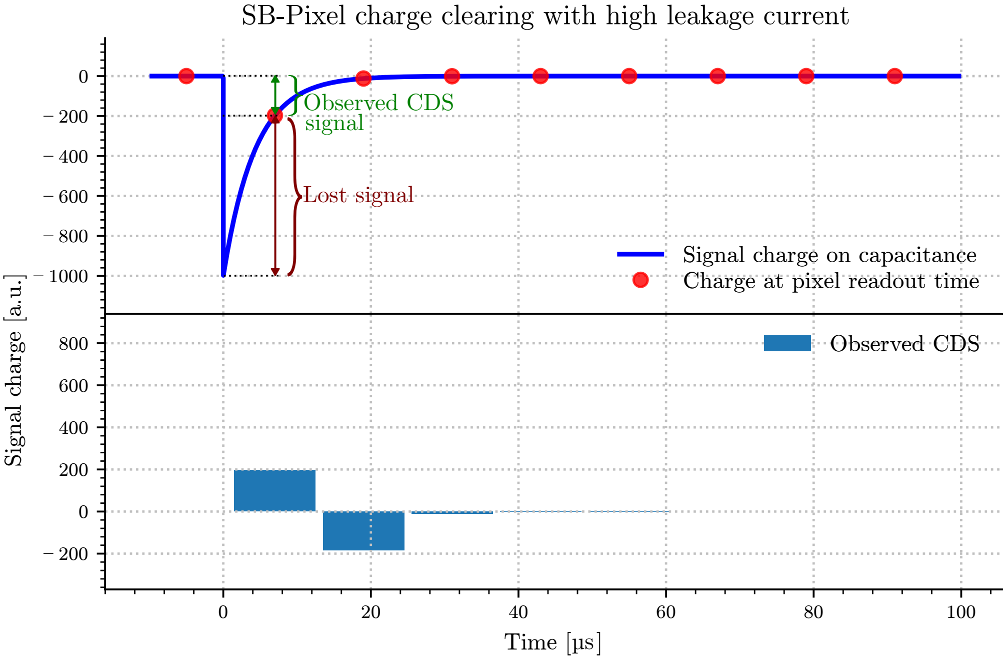

Figure 2.11: Charge clearing of an SB-Pixel with high leakage current. All parameters except leakage current are the same as in Figure 2.10; leakage current has been increased from 100 fA to 500 fA.

of magnitude as the integration time t_{int}, a substantial fraction of the initial signal charge Q_{Phys} is cleared before the pixel is read out.

Binning the individual amplified CDS signal heights which are higher than $U_{\text{hit thr.}}$ into a histogram creates a seed spectrum for a pixel. Combining these histograms creates a seed spectrum of an entire pixel matrix. This signal response spectrum was used extensively in this thesis to analyze the radiation hardness of CMOS MAPS. The following subsection (Section 2.5.2) introduces important derived observables used to quantify the radiation hardness of a sensor based on these spectra; it also discusses charge collection efficiency.

The radiation-induced change in space-charge density affects the depleted volume of a sensor. In the depleted volume, an electrical field is used to collect signal electrons. This type of charge carrier collection is significantly more effective than collection via thermal diffusion (used when an electrical field is not present) [Dor+10]. Damage from radiation exposure increases the space-charge density, which reduces the depleted volume and so makes charge collection more difficult. In contrast, a reduction in space-charge density can have a positive effect on charge collection. A theoretical treatise on the reduction of the depleted volume can be found in Section 2.3; experimental findings are reported in Chapter 7.

2.5.2 Charge collection efficiency and seed spectra

The signal height of a single hit[17] can be binned into a histogram, resulting in a charge distribution spectrum (see f.e. Figure 2.12). The magnitude of each hit signal depends on many factors, see Figure 2.9. These factors are:

- The number of signal electrons generated by a single hit, which depends on the energy and the type of the sensor trans-passing particle
- The collected charge, which depends on the sensor efficiency and its quality
- The gain, which depends on the capacity of the diode and the sensing circuit
- The mean free path of an electron in the epitaxial layer of the pixel, which depends on epitaxial layer resistivity, radiation damage, and temperature
- The exact geometry of the pixel and its components, especially its diode size, epitaxial layer thickness, and distance to neighboring pixels
- The size of the depleted area, where the charge is collected via electric fields
- The size of the non-depleted area, where the charge is collected mostly through diffusion and doping gradients

The central pixel, which collects the most electrons for a single hit, is called the seed pixel. Together, the seed pixel and its neighbors form a pixel cluster. A cluster accumulates nearly all of the diffused charge of all participating pixels [Dri10].

---

[17] detectable impact of an individual particle on the sensor

The fraction of the maximum charge, collected together by all cluster pixels is called cluster charge collection efficiency (CCE$_{25}$). The portion of the maximum charge, collected by a single seed pixel is called seed charge collection efficiency (CCE$_1$); CCE data is given in percentages in this thesis.

The resulting charge distribution spectrum depends on the shape of the radiation-generated charge cloud. This charge cloud depends on processes in the silicon – the primary particle often produces several secondary particles. The most important interactions in this thesis result from:

Electrons/β-source (Sr-90): An electron through silicon ionizes grid atoms along its path. Due to its low mass, it reaches relativistic velocities quickly. A singly charged relativistic particle with $\gamma \approx 3$ is often referred to as an MIP. A γ-particle creates on average 80 electron-hole pairs per µm of its trajectory in silicon.

Heavy ions (Lead/Pb) : Heavy ions, like all charged particles, create charged particles along their path. The number of electron-hole pairs scales with the square of the heavy ion charge; more electron-hole pairs are generated by ionized particles with more charge. Non-relativistic heavy ions produce electron-hole pairs non-homogeneously along their path. The density is inversely proportional to their continuously decreasing energy [Lut07, p. 26].

X-rays/γ-source (Fe-55, Cd-109[18]): High-energy photons have point interactions in silicon, producing many electron-hole pairs in a 1 µm^3 volume when the initial energy is below 200 keV, this is the case in this thesis. In such situations, interactions are based on the photoelectric effect [Lut07]. A photon transfers all of its energy to an orbital electron, which is ejected with a kinetic energy equal to the initial photon energy less the electron binding energy. The number of produced electron-hole pairs can be calculated from the initial photon energy and the average energy for electron-hole pair creation in silicon (3.6 eV).

When illuminating a sensor with a monochromatic γ-source, distinct peaks are visible in the energy distribution. These peaks can be used to calibrate the energy spectra and calculate the amplification (or gain) of the entire readout chain. If a hit occurs in the diode of the sensor or in the depleted area, the diode is able to collect 100 % of the charge. This creates a charge collection peak that can be used to convert the energy amount from analog to digital units (ADU) to the number of produced electrons or the deposited energy; this is accomplished by assuming a linear signal amplification from zero to the energy range of interest. To demonstrate this calibration process we can exemplary take a look at the full charge collection peak in Figure 6.4a at about 240 ADU, with a depletion voltage of 8.3 V. This peak was caused by K_α photons with an energy of 5.9 keV that came from a used Fe-55 source. A second full energy peak can be identified at 280 ADU; this was caused by direct diode or depleted volume hits of K_β photons with an energy of 6.4 keV. The linear energy scaling across the entire range of

---

[18] **Cad**Cadmium isotope with a mass number of **109**

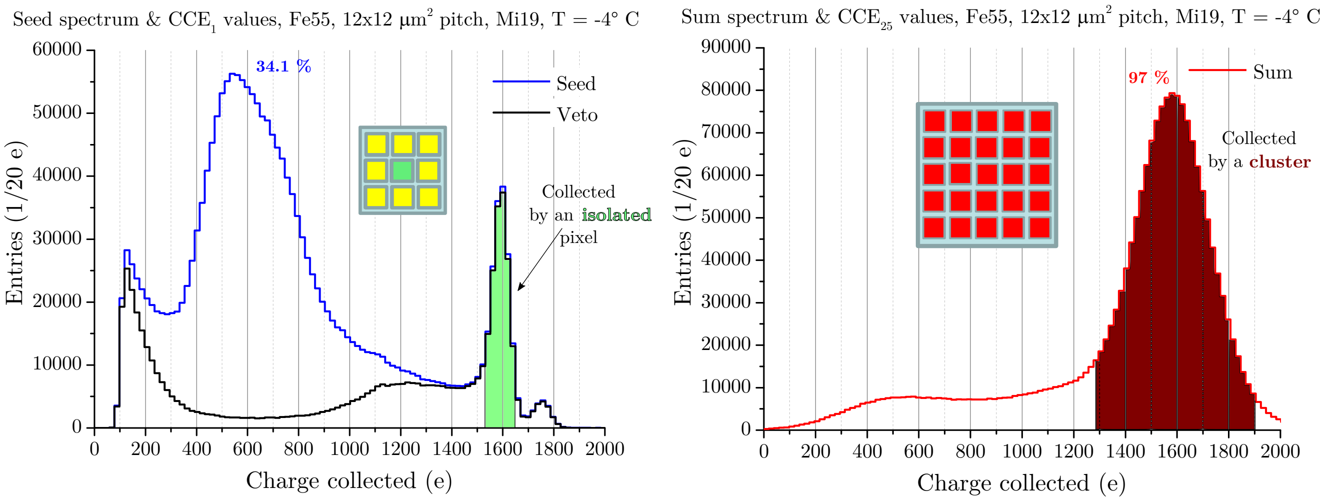

(a) Veto and Seed spectrum.

(b) Sum spectrum.

Figure 2.12: Comparison of MIMOSA-19 veto, seed and sum spectra. The sum spectrum is constructed by summing the charge of a 5×5 pixel cluster surrounding the “firing” hit pixel. The percentages above the peaks denote the CCE$_1$ (a) and CCE$_{25}$ (b) values.

interest can be checked due to the existence of two fixed energy values (the distinct K$_\alpha$ and K$_\beta$ peaks). The scaling technique described here was applied to all calibrated spectra in this thesis. As the calibration is dependent on temperature, the pixel parameters, and radiation damage, each measurement required its own calibration. Figure 4.2 provides a sample comparison of calibrated and uncalibrated spectra.

Figure 2.12a shows an example of an already calibrated seed pixel. The 100 % charge collection peak was used to calibrate the Fe-55 spectrum and so was located at 1640 e. The much higher peak at about 560 e was generated by hits outside of the diode in the epitaxial layer. These more probable hits are collected less efficiently, and part of the signal charge is collected by neighboring pixels. The most probable charge collected by a single pixel from a non-irradiated, cooled MIMOSA-19 sensor is 560 e, which would equal a single pixel CCE (CCE$_1$) of 34.1 % as denoted in Figure 2.12a. The area at low energy values < 300 e in Figure 2.12a contains negligible signal charge and is considered to be dominated by noise.

Veto spectrum

Figure 2.12a shows the veto spectrum in black. The veto spectrum is compiled by only considering hits where most of the charge is collected by an isolated pixel, namely the central (seed) pixel in a cluster. The charge collected in the central seed pixel is compared to the overall collected charge in the neighboring pixels. These neighboring pixels form the pixel cluster. If almost no charge is collected by the neighboring pixels, then the hit contributes to the veto spectrum.

Usually, a particle creates a signal electron cloud, which is collected by multiple pixels. When γ particles convert to electron-hole pairs in silicon, they create a localized signal electron cloud. If this signal electron cloud is created in the collecting diode or the depleted region of the collecting pixel, then most of the charge is collected by an isolated pixel. In silicon, γ particles of the same energy create roughly the same number of signal electrons, so a peak emerges when the number of particles is counted in relation to the collected charge. The black line in Figure 2.12a was formed by collecting only events where an isolated pixel collected all of the hit charge. The blue line shows all hits, not just those where the cluster collected almost no charge. As such, the veto spectrum is embedded in the seed spectrum.

The veto spectrum is important because the resulting peak can be used to calibrate a sensor to a known γ particle energy (see Section Section 2.5.2). Moreover, the spectrum can be used to determine the number of hits detected by only one pixel. From this, depletion, charge sharing, cluster sizes and radiation hardness of the sensor can be estimated.

Sum spectrum

Signal electrons generated outside the depleted area or the diode diffuse into neighboring pixels and are collected by their diodes. The signal charge is shared, so charge collection is below 100 % in the seed pixel for these hits. The sum of the collected charge in a whole cluster accounts for nearly all of the missing charge in an undamaged sensor (see Figure 6.4b).

2.5.3 Signal-to-noise ratio

A Strontium-90 β-ray source can be used to study the sensor response to MIPs like particles. A MIP is defined as a charged particle losing a minimum of energy when traversing a material. According to the Bethe equation (Figure 2.4), β particles happen to have such minimum energy deposit at a γ factor of $\approx$3. On average, such a MIP creates approximately 80 e per passed µm of silicon. By definition, this low energy loss make MIPs most challenging to detect with CMOS MAPS and are therefore used as a benchmark. Therefore we use high energetic β-rays from radioacive decays to test sensor sensitivity in the laboratory.

The Sr-90 decays to Y-90[19] with a half-life of 28.9 years; Y-90 decays with a half-life of 64.1 hours and emits electrons with a maximum energy of 2.2 MeV ($\gamma\approx5.3$). The signal response spectrum for β particles is a continuous distribution with no narrow peaks, in contrast to the signal response spectrum for photons, which has characteristic photo peaks. Although most emitted electrons have lower energies and do not resemble MIPs, there are enough high energetic electrons to study their detector signal response.

---

[19] **Y**ttrium-90, an isotope of yttrium

The energy loss of beta rays in thin detectors is Landau distributed. Therefore a β-spectrum recorded by a sensor has the typical Landau peak – a broad maximum with an asymmetric extension to high energies. The Bethe-Bloch formula (see Figure 2.4) describes the mean energy loss per distance traveled of charged particles when traversing through matter. The energy loss of a charged particle through ionization in a thin layer of matter was theoretically described by Landau in 1944 [Lan44]. The Landau distribution resembles an asymmetric Gaussian distribution with a long tail toward high energies. This tail results from the small number of individual collisions, each of which has a small probability of transferring a large amount of energy. The transferred energy is deposited into the material by a subsequent cascade. The energy limit of the cascade is theoretically infinite, while the energy deposited by the incoming particle cannot exceed the energy of the particle [Mer18]. Protons, pions, and other charged particles, which resemble MIPs, produce approximately Landau-distributed spectra when traversing MAPS.

The S/N ratio indicates how well a signal can be distinguished from the background. It is the quotient of the most probable signal amplitude (MPV[20]) and the average sensor noise. Each pixel in a sensor has its individual noise, the average sensor noise is therefore the average over all pixel. For an example spectrum see Figure 5.3 and previous works [Doe15, p. 72]. A high S/N value indicates that, even in the case of digital readout, actual hits can be clearly separated from fake hits by comparing them to a fixed charge threshold value. Empirical studies have shown that a Sr-90 S/N ratio above 15 implies an MIP detection efficiency above 99 % at a fake hit rate of $< 10^{-5}$ [Dev08, p. 124][Doe15, p. 79].

In this thesis, I evaluate signal detection efficiency by setting a fixed noise threshold value. The exact value is stated in the corresponding plot, when applied. Entries in the Landau distribution below this threshold are considered noise and those above are summed to calculate the number of registered β particles. A strongly irradiated sensor of the same type and exposed to the same environmental conditions must detect the same number of hits as a non-irradiated reference sensor. The sensor is considered radiation hard if the same number of hits is registered, given the same fixed noise threshold value. I use this method in Figure 6.13 on page 98.

---

[20] **M**ost **P**robable **V**alue

Chapter 3

Effects of radiation damage

> *"All models are wrong;*
> *some models are useful."*
>
> George Edward Pelham Box

The MVD aims to reconstruct the secondary decay vertices of D mesons and so must be installed close to the primary interaction vertex of the collision between 5 and 20 cm downstream the target and inside vacuum. Consequently, the sensors will be exposed to more radiation per area and per collision than any other subdetector of the experiment. During operation, the sensor of the MVD will be exposed to radiation damage caused by various particles, such as photons, electrons, charged hadrons, neutrons, and light ions. The precise damage mechanism depends on the nature and energy of the particles. An overview of the relevant types of radiation and their microscopic interactions is provided in this chapter.

Radiation damage is caused by interactions between impinging particles and matter and alters the detector material in undesirable ways. Radiation damage can be subdivided into two major groups, ionizing and non-ionizing. While ionizing interactions with atomic orbital electrons produce ionization processes, non-ionizing interactions cause elastic collisions that remove atoms from the crystal lattice. Most particles can cause both kinds of radiation damage, so irradiated components typically exhibits a mixture of the two types. To improve the radiation tolerance of the devices under study, an understanding of the individual mechanisms is required.

3.1 Ionizing radiation

Charged particles and photons can cause radiation damage through ionization. The energy transferred into the electron cloud ionizes atoms or breaks atomic bonds and molecules. In crystals, this can excite and free electrons from their bands, but the atoms remain at their positions in the crystal lattice.

In pure silicon, holes caused by absent electrons anneal through diffusion, thermally excited conduction-band electrons replace the missing electrons. Nevertheless, interfaces between materials of different lattice constants can be permanently damaged. CMOS MAPS are composed of different layers of material. The uppermost layer is often a SiO_2 insulator. It has a lattice constant that deviates from that of the silicon below it, and there are many irregular lattice bonds at the transition between the two materials [Dev08]. The irregularity makes this area intrinsically imperfect. If ionizing radiation breaks the bonds at the transition, the electric properties of the material change permanently. Because permanent ionizing damage occurs predominantly on the boundary of the active volume between the different material layers in MAPS, it is often called surface damage. The detailed mechanism of the surface damage generated in these structures is explained in [Sch+88]. In dosimetry, the energy of the knocked-out electrons is measured and used to estimate the total energy deposition. Ionizing radiation is quantified in rad, which equals 10^{-2} Gy in SI units. One Gy equals an ionizing energy deposit of 1 J/kg. The rad, though not an SI unit, is widely used in detector physics and is also used in this thesis for consistency with previous publications [Doe15][Dev08].

In silicon dioxide, electric fields can cause the electron-hole pairs generated by ionizing radiation to drift apart in opposite directions. The probability of electron-hole pair recombination decreases as the electrical field increases. Electrons have higher mobility than holes and can exit the silicon dioxide, leaving the holes without a recombination partner. The electric field slowly moves the holes to the interface between the SiO_2 structures and the bulk silicon [Dev19]. At the interface, the holes may be trapped by oxygen-vacancies, which are abundant at the Si-SiO_2 boundary. The total number of traps depends strongly on the exact manufacturing process of the device. As a result, the percentage of trapped holes can vary from a few percent to almost 100 %. A positive charge accumulates at the interface and generates electric fields [LR07].

In absence of an electric field, the electron-hole pairs do not drift apart and therefore recombine in most cases. As a result, the surface damage generated by the ionizing irradiation is significantly less in detectors that are not supplied with voltage during irradiation. To correctly evaluate radiation hardness against ionizing radiation, the surface damage must be produced with detectors that are operational during irradiation. If the detectors are not supplied with power, the radiation hardness will be overestimated, and the results will not reflect a realistic scenario in a detector.

There are two main groups of trapped holes. Holes enclosed in the nonconductive SiO_2 near the interface are called oxide charges. Their charge is always positive. Following irradiation, the number of oxide charges gradually decreases through room temperature annealing. A significant proportion of the traps can withstand several months of annealing. Holes enclosed on the conductive Si side can cause defects in the silicon band gap and are called interface traps. Depending on their energy and the local Fermi level (i.e., doping), their charge can be positive, neutral, or negative. Interface traps do not anneal at room temperature. The charges generated by both types of traps accumulates; the sum can be negative if negatively charged interface traps exceed oxide charges [Dev19].

Historically, surface damage was studied to develop sensors for optical imaging in harsh radiation environments, such as space. However, the requirements for optical sensors in space differ significantly from the requirements for CPS in heavy-ion experiments. As such, some recent studies have focused solely on surface damage in CPS for heavy-ion experiments. A good overview of these studies and their results is provided in M. Deveaux's Ph.D. thesis [Dev08]. In [Doe15], the improvements made in the time resolution and ionizing radiation hardness of MAPS are presented and that the sensors manufactured with the TowerJazz-0.18 µm CMOS process are suitable for achieving the 10 Mrad ionizing radiation hardness required for the CBM experiment is demonstrated.

Ionizing radiation effects were not explicitly studied in this work. However, the related effects must be considered since most sources used for irradiating the detectors also produce an undesired ionizing dose. This dissertation contributes to the experimental study of radiation hardness in MAPS by investigating possibly dangerous types of radiation not previously considered and selecting the most promising sensor properties.

3.2 Non-ionizing radiation

In contrast to photons, massive particles like hadrons can knock a silicon atom from the lattice. Crystal atoms can be displaced from their default position in the grid if a radiation particle transfers an elastic scattering energy of, on average, 25 eV [Van+80][Lut07] to the primary knock-on atom (PKA) of the lattice. The amount of transferred energy can be calculated using the laws of energy and momentum conservation. Particles with a high mass need less kinetic energy to displace an atom; the atom displacement cross-section is primarily dependent on particle type (i.e., particle mass) and kinetic energy.

A cascade occurs when the PKA has enough energy to displace other lattice constituents. In such a scenario, clusters of lattice vacancies and atoms may form in interstitials in a localized region of the crystal. These clusters have a significant effect on the electrical properties of the active volume of the sensor. Massive particles have a higher chance of creating larger defect clusters. This effect is called bulk damage.

Bulk damage is characterized by lattice atom displacement and nuclear interactions like transmutation or neutron capture. These changes are often temporary and partially anneal with temperature. [Doe10] conducted a dedicated study on this effect in MAPS. The ROSE[1] collaboration [al01] did a more general study on the dynamics of defects in silicon.

The minimum energy needed to displace a silicon lattice atom is 15 eV. This energy can be obtained from an energetic particle elastically scattering with the recoiling atom. This energy border is not sharp. The minimum energy needed to knock an atom from the lattice is 15 eV; the energy needed for a 50 % chance of recoil is 25 eV [Van+80].

Proton and neutron projectiles are lighter than silicon target atoms. Due to this mass difference and momentum conservation, their minimum kinetic energy has to exceed a threshold $\approx 190\,\mathrm{eV}$ in order to displace a silicon atom [Lut07]. An electron is lighter still. The minimum kinetic energy required to create a point-like defect must be calculated relativistically and is $\approx 260\,\mathrm{keV}$. For pions, which have a mass between those of an electron and a nucleon, this threshold is above about $\approx 1.3\,\mathrm{keV}$.

If the energy of a projectile significantly exceeds the threshold energy, the recoiling PKA may receive over 2 keV of energy, which is enough to create additional defect clusters in secondary reactions. Typical clusters feature about 100 lattice displacements and are over 5 nm in diameter [Lut07]. Parts of these defects will anneal by diffusion over time. For proton and neutron projectiles, the minimum kinetic energy for cluster creation exceeds about 15 keV. This energy is significantly higher for electrons (approximately 4.6 MeV) [Lut07], so electrons usually do not generate defect clusters.

High-energetic neutrons, hadrons, and ions are responsible for most defect clusters. Usually, defect clusters emerge at the end of a PKA track, when the kinetic energy is between 5 keV and 10 keV and the elastic cross-section with silicon increases by several orders of magnitude [Lut07]. Although these numerical values come from model calculations, they are useful for understanding radiation damage effects.

NIEL

Dosimetry on non-ionizing radiation is completed within the framework of the non-ionizing energy loss (NIEL) model [Vas97]. The NIEL model assumes that the radiation damage scales with the non-ionizing energy deposit. As one is interested in the total displacement damage, rather than in the individual interactions, a particle type and energy-dependent displacement damage cross-section $D(E)$ can be defined as follows:

$$D(E) := \sigma(E) \cdot \int_0^{E_\mathrm{R}^\mathrm{max}} f(E, E_\mathrm{R}) p(E_\mathrm{R}) dE_\mathrm{R} \tag{3.1}$$

---

[1] **R**esearch and development **O**n **S**ilicon for future **E**xperiments

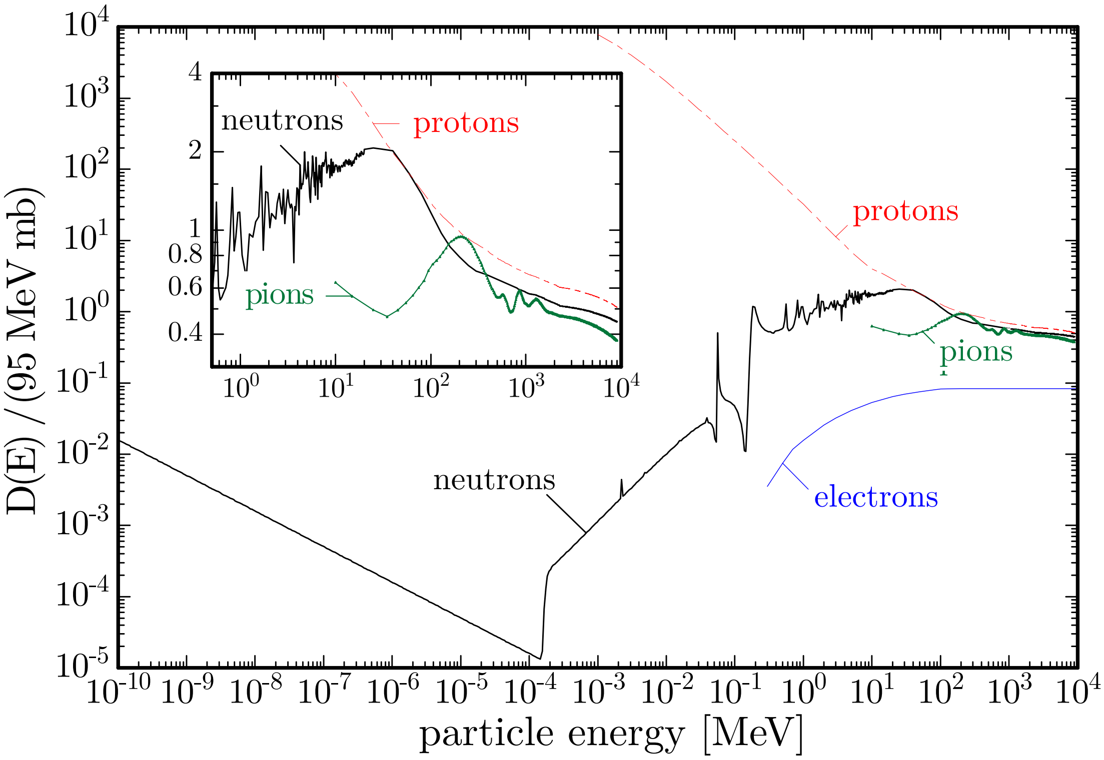

Figure 3.1: Displacement damage cross-section $D(E)$ normalized with respect to 1 MeV neutrons. Data compiled from many sources taken from [Fre+02].

The displacement damage cross-section D describes the total NIEL of a projectile particle with an initial energy E. The function $\sigma(E)$ denotes the total energy-dependent cross-section of different particle types with silicon, $f(E, E_R)$ is the density function relating the transferred energy E_R to the initial particle energy E, and $p(E_R)$ is the probability of a silicon ion being knocked from the lattice for a given transferred energy E_R.

Equation (3.1) relates the displacement damage cross-section in silicon D to the energy E of an impinging particle. Every particle species has a displacement damage cross-section $D(E)$, as seen in Figure 3.1. This cross-section D is equated to the total NIEL of a particle. The NIEL-scaling hypothesis posits that the NIEL value and the total non-ionizing damage in silicon are proportional. This means, that the non-ionizing radiation damage in pure silicon is proportional to the NIEL of particles traversing it. This scaling is based on the hypothesis that the multifaceted primary knock-on interaction is smoothed out by numerous secondary interactions of the knocked-out silicon atoms. As such, only total energy transfers to the lattice generate bulk damage. The interaction with the electron cloud produces no crystal defects, so there is no bulk damage, and only the NIEL influences the scaling [Vas97]. The units for the displacement damage cross-section are usually MeV mb; the units for the NIEL value are the units either for lost energy per length of traversed material (MeV/cm) or lost energy scaled with the cross-section per mass of crossed material (MeV cm^2/g). For silicon, a conversion can be made, with 100 MeV mb = 2.144 keV cm^2/g. To set the scale, the displacement damage cross-section of a 1 MeV neutron is set to $D_\mathrm{n}(E = 1\,\mathrm{MeV}) = 95\,\mathrm{MeV\,mb}$ by definition [Int]. The NIEL scaling can be used to approximate the bulk damage potential of any particle species with a given energy distribution by a hardness factor k. The actual particle energy spectrum of $\phi(E) = d\mathit{\Phi}/dE$ is folded with its displacement damage cross-section $D(E)$ and normalized to an equivalent 1 MeV neutron flux:

$$k := \frac{\int D(E)\phi(E)dE}{D_\mathrm{n}(E = 1\,\mathrm{MeV}) \cdot \mathit{\Phi}_\mathrm{n}} \quad . \tag{3.2}$$

For example, $k = 2$ implies that the damage from a hypothetical particle flux is twice as large as the same flux Φ_n of mono-energetic 1 MeV neutrons. The total non-ionizing displacement damage of any radiation can be scaled to an equivalent 1 MeV neutron flux that produces the same bulk damage. Based on this convention, the scaled non-ionizing radiation dose is given in units of $\mathrm{n_{eq}/cm^2}$ and describes the equivalent energy deposit of a 1 MeV neutron flux through a $1\,\mathrm{cm}^2$ area.

Figure 3.1 plots the collected damage function cross-section data. The minimum kinetic energy required for a neutron to transfer 15 eV and displace a silicon atom by elastic scattering is ≈120 eV. At this energy, the cross-section for neutrons is at its lowest value in Figure 3.1. For neutron energies below this threshold value, the cross-section rises monotonically. This growth can be explained by neutron capture: silicon can capture slow neutrons in inelastic collisions and emit γ photons. The resulting recoil kinetic energy is 780 eV on average [Sch59], enough to displace additional silicon atoms. As discussed later in this thesis, these inelastic effects should not be neglected in highly boron-doped silicon, which is used in the highly p-doped regions of a CMOS sensor. The NIEL scaling approximates the non-ionizing radiation damage in pure silicon only; deviations are expected for the complex silicon structures in CMOS MAPSs.

For the highest energies, the damage cross-sections of protons and neutrons almost match. A decreasing interaction time at high velocities explains this effect; the particles spend less time in the individual Coulomb potentials of the silicon ions. The neutron and proton curves touch at about 40 MeV in Figure 3.1. This energy corresponds to a relativistic velocity $\beta > 0.27\,c$. For lower velocities, the Coulomb interaction becomes increasingly prominent, and therefore, the damage cross-section for the proton is significantly higher than that of the neutron.

The neutron displacement damage cross-section has multiple calculated resonances within the energy range of 1-20 MeV [al92]. Some experimental data is available for this range and confirms the calculated values [Wun92]. For high energies above 20 MeV, mono-energetic neutron sources are not available [VL00b]. As such, the curve is partly theoretical and partly experimental.

While the hardness factors of the most abundant particles – protons, neutrons, electrons and pions – are well studied, little is known about integrated NIEL damage caused by heavy ions. Chapter 8 (page 106) presents relevant studies on the irradiation of CMOS MAPS with 10^{10} 30 AGeV Pb ions.

Table 3.1: Overview of different particle types and their induced radiation damage. Red cells denote a higher event risk for a CBM CMOS sensor than yellow cells (moderate risk) and green cells, which shall represent a lower risk. Compiled from [Hol12] and [Kni81].

Radiation	**Kinetic Energy**	**Interaction**	**Impurity production**	**Atom displacement**	**Ionization**
Thermal neutrons	meV	Elastic and inelastic nuclear scattering	🟨 Directly by absorption reactions, may induce radiation[a]	🟥 Yes, indirectly	🟥 Indirectly
Cold neutrons	eV			🟥 Indirectly	🟥 Indirectly
Fast neutrons	MeV			🟥 Multiple displacements via scattering reactions; can cause displacement of knock-on atoms[b]	🟥 Indirectly
Fission fragments	keV	Coulomb and nuclear scattering	🟨 Can become impurities[a]		🟥 These highly charged ions cause considerable ionization, and they emit β and γ
α-particles			🟩 Not damaging at MAPS operation energies	🟥 Yes, may cause atom displacement	🟥 Causes sizable ionization
Protons				🟥 Yes	🟥 Directly
Electrons		Coulomb scattering	🟩 n/a	🟨 Some displacement	🟥 Directly
Photons		Compton scattering	🟩 n/a	🟩 Rare displacements	🟨 Directly

---

[a] Studied in chapter 7, see page 99 ff.

[b] Studied in chapter 5, see page 66 ff.

3.3 Effects on detector performance

The changes to the material described in previous sections significantly impact detector properties, causing

1. an increase in the reverse-bias leakage current,
2. a change in space-charge density within the space-charge region, and
3. signal electron trapping/recombination [Lut07].

The importance and magnitude of each effect are dependent on the type of irradiation and the CMOS material used. As shown later in this thesis, all three effects play important roles in different detection scenarios. Table 3.1 gives an overview on the anticipated damage of different particle types in specific energy ranges.

Reverse-bias leakage current

Radiation-induced bulk defects produce additional states in the band gap of silicon. These states can act as generation and recombination centers for free charge carriers and so increase the thermal leakage current of charge collecting diodes. Leakage current is caused by random electron and hole generation within the depletion region of a PN junction (see Section 2.3). This charge generation scales with the number of crystallographic defects within the depletion region of CMOS MAPS. The random shot noise caused by reverse-bias leakage current is one of the primary sources of noise in sensors. Increased leakage current has several adverse effects on the detection properties of CMOS MAPS. For example, an increase in the fluctuating shot noise causes a decrease in S/N ratio and complicates the discrimination of an MIP signal .

Change of space-charge density

Space charge is a theory that treats excess electrical charge as a charge continuum distributed over a region of space rather than as distinct point charges. Defects in the crystal lattice appear as impurities. Depending on their charge states, the defects may alter the effective doping concentration and the space-charge density. Original dopants may be captured by the defects and fail to remain acceptors or donors. This generates further defects, which may produce new states within the space-charge region that are distinct from the original dopant state. [Wun+92] described an effective doping inversion. An n-type doped silicon wafer first becomes intrinsic due to increasing irradiation; at a certain point, the effective doping concentration reverses, and the wafer effectively becomes p-doped. In initially highly p-doped low-resistivity silicon, the doping is reduced through non-ionizing radiation doses of up to $10^{14}\,\mathrm{n_{eq}/cm^2}$. At higher radiation doses, strong effective doping removal occurs, and the effective doping reaches a minimum of a few $10^{15}\,\mathrm{n_{eq}/cm^2}$ [Dev19]. High-resistivity silicon has a lower initial p-doping concentration, so the minimum effective doping concentration is

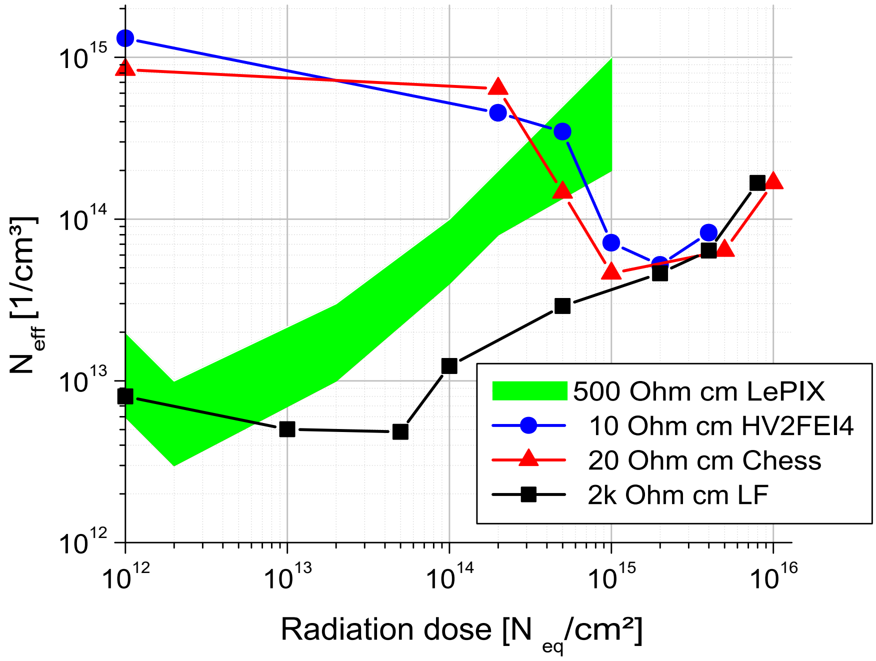

Figure 3.2: The effective doping concentration N_{eff} of silicon produced through different manufacturing processes; the silicon was irradiated with neutrons, the dose is normalized to 1 MeV neutron flux equivalent. The effective dopant concentration of the initially p-doped silicon wafers changes for neutron irradiation of a few 10^{13} to $10^{14}\,\mathrm{n_{eq}/cm^2}$. The plot is from [Dev19], and the data is from [Man+17][Aff+16][Pot+13].

achieved at lower radiation doses (see Figure 3.2). This alters the space-charge density in the space-charge region and the width of the depleted region, which in turn modifies the area of efficient charge collection. Section 2.3 discussed the impact of doping concentration on the width of a depleted volume in a PN junction. Impurities can have a comparable effect on the width of the depleted area of a diode in a CMOS sensor.

Loss of signal electrons

Due to the signal charge transport mechanism, the loss of signal electrons is extremely detrimental to the operation of CMOS MAPS. This loss may be caused by recombination and trapping. Sensors collect the signal charge via thermal diffusion and drift through electrical fields. Defects may capture some of the signal electrons during their drift. The rate at which signal electrons are captured is inversely proportional to their mean free path. Defects decrease the mean free path of signal charge and therefore increase the capture rate. The average probability P_{trap} of a signal charge being captured over a distance z can be expressed as

$$P_{\text{trap}}(z) = \sigma \cdot z \cdot n_{\text{trap}} \quad ,$$

where n_{trap} is the effective concentration of traps and σ is the capture cross-section. In other words, the mean lifetime τ to of an electron is

$$\tau = \frac{1}{\sigma \cdot v \cdot n_{\text{trap}}} \quad ,$$

where v is the velocity of the signal electrons; this value depends on the thermal drift and the applied electrical field. τ can be decomposed into intrinsic and radiation-induced parts [Lut07]. An effective lifetime τ_{eff} of the signal charge until recombination or trapping can be defined as [Dev19]

$$\frac{1}{\tau_{\text{eff}}} = const \cdot \Phi \quad ,$$

where Φ is the normalized non-ionizing radiation dose and *const* is an empirical factor. It can be either a recombination damage factor K or a trapping time parameter β_{e}. K is $\approx 2.5 \times 10^{-6}\,\text{cm}^2/\text{s}$ for electrons in p-doped silicon exposed to 1 MeV neutrons [Kra84]. At $T = 20\,^\circ\text{C}$, β_{e} can have values from $(3.4 \pm 0.3) \times 10^{-7}$ to $(4.7 \pm 0.4) \times 10^{-7}\,\text{cm}^2/\text{s}$, depending on the p-doped material being analyzed [Cin+09]. Part of the signal is lost once τ_{eff} reaches the same order of magnitude as the charge collection time.

3.4 Radiation sources

Once a heavy-ion experiment begins operation, it is difficult to access the built-in detector components. Each maintenance must be planned, and the number of inspections should be kept to a minimum in order to avoid interrupting the experiment. As a result, the deterioration of the sensors in such experiments has been studied in laboratory settings to develop detector components with prolonged maintenance-free operation periods. It is also essential to estimate the time at which sensors have experienced sufficient radiation damage to no longer function properly.

The complex radiation profile of an experiment must be taken into account when predicting sensor lifetime. Unfortunately, it is impossible to irradiate a detector with the same radiation mixture it will experience in an experiment, but as long as the non-ionizing and ionizing total doses are reproduced correctly, the exact particle species and their energies are unimportant (see Section 3.2).

The expected total experiment radiation was reproduced via accelerated aging with a mixture of intense radiation sources in several nuclear research facilities. Ionizing damage and non-ionizing damage can be distinguished from each other because they have different effects on CMOS sensors, as mentioned before. To study these effects separately, the irradiation particles and their energy ranges were selected to closely reproduce the effect of the expected running conditions.

3.4.1 FRM II reactor (fast or slow neutrons)

MEDAPP

The MEDAPP[2] beamline of the FRM II[3] research reactor in Garching was used for irradiation with unmoderated fission neutrons [Bre+08]. Figure 3.3 illustrates the neutron energy spectrum of the reactor. The configuration of the reactor directs thermal neutrons to U235 targets and generates nuclear fission in the air. The resulting unmoderated fission neutrons produce a spectrum with an average neutron energy of (1.9 ± 0.1) MeV and a median of (1.5 ± 0.1) MeV [Bre+08]. About 80 % of the neutrons have energy values in the range of 0.6 – 4.5 MeV, about 4 % have energy values below 0.6 MeV, and only 1 percent have an energy value less than 100 keV. The beamline has a hardness factor $k \approx 1$. The neutron flux of FRM II has a rate of $(3.2 \pm 0.2) \times 10^{8}\,\mathrm{n_{eq}/cm^2{\cdot}s^{-1}}$, the ionizing gamma background is specified as 100 kRad per $10^{13}\,\mathrm{n_{eq}/cm^2}$, and the accuracy of the dosimetry is 10 % [Bre+08].

PGAA

Other sensors were irradiated by the PGAA[4] beamline of the FRM II reactor [Rev15] using cold neutrons, which had a mean energy $E_{\text{cold n.}} = 1.8 \times 10^{-3}$ eV and $k = 0.003$, and an unknown ionizing dose. The hardness factor k used in this thesis was obtained by folding the spectrum given in [Kud+08] with hardness factors according to [VL00a]. The obtained neutron energy distribution spectrum is compared to other prominent neutron beams in Figure 3.3.

3.4.2 Ljubljana (fission and moderated neutrons)

The nuclear reactor TRIGA[5] at the Jožef Stefan Institute in Ljubljana (Slovenia) is the reference reactor for CERN; it was previously used by ROSE and is now used by the RD50 collaboration. This facility is also used for the irradiation of MIMOSA sensors with fast neutrons. Samples are stored in irradiation capsules and placed into the TRIGA reactor [SŽT12]. Figure 3.3 shows a comparison of the MEDAPP and PGAA spectra. The Ljubljana spectrum spans over a broad energy range, reaching up to 10 MeV, while the MEDAPP has a peak at 1.9 MeV.

3.4.3 SPS (heavy ions)

Chapter 8 details a study on the impact of heavy ions on the radiation hardness of the sensors [Con16][LDB16]. Four MIMOSA-34 THR sensors were exposed to primary 30 AGeV Pb ions at the CERN-SPS. The sensors were covered with aluminum foil and mounted on a tailored plastic holding structure. The sensors were placed in the beam line 200 m upstream of the target of the NA61/SHINE

---

[2] **Me**dical **app**lications

[3] **F**orschungs**r**eaktor **M**ünchen 2

[4] **P**rompte-**G**amma-**A**ktivierungs-**A**nalyse

[5] **T**raining, **R**esearch, **I**sotopes, **G**eneral **A**tomic

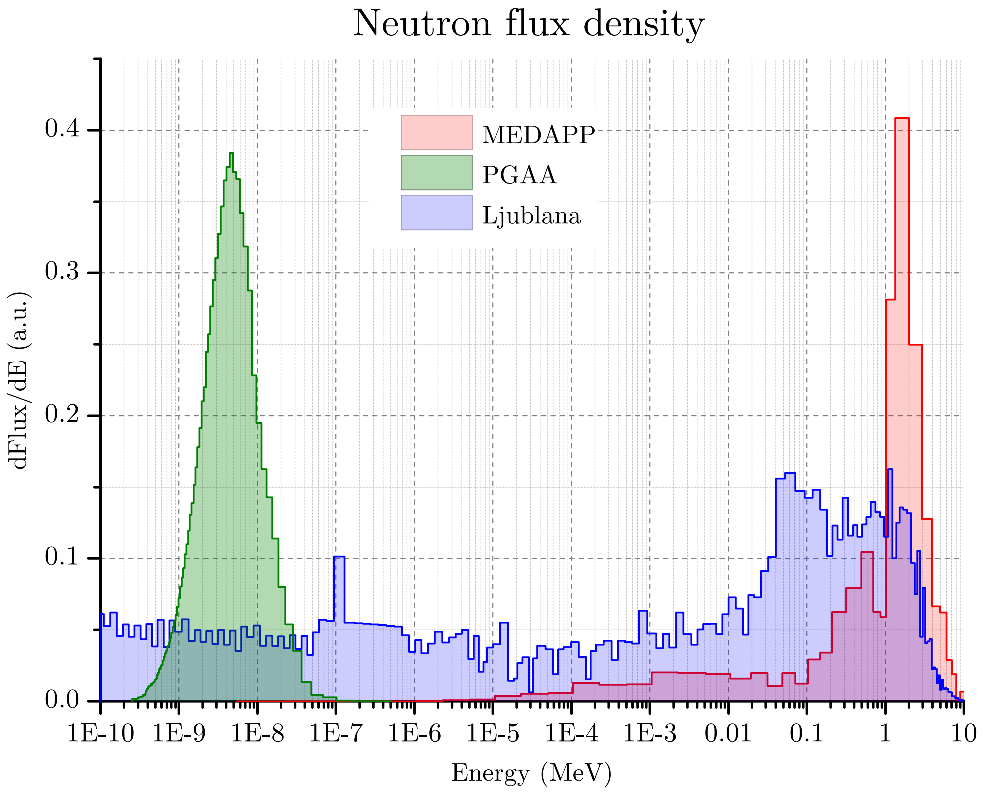

Figure 3.3: The neutron differential flux of the MEDAPP (hardness factor $k \approx 1$) and PGAA beamline of the FRM II research reactor compared to the beamline flux of the research facility Ljubljana, data compiled from [Bre+08], [Man] and [Kud+08].

experiment. The flux of ions was estimated by an ion-sensitive $4 \times 4\,\mathrm{mm}^2$ scintillator. The scintillator PMT[6] signals were forwarded to the counting house, and the individual ions were counted. During two weeks, an integrated ion flux of 1.2×10^{10} Pb ions per cm^2 was applied.

---

[6] **P**hoto**m**ultiplier **t**ube

Chapter 4

Improving radiation hardness

> *"When to use iterative development? You should use iterative development only on projects that you want to succeed."*
>
> ---
>
> Martin Fowler

There are many possible approaches to improving the radiation hardness of CMOS sensors to non-ionizing radiation. Since the study of radiation damage is closely related to the possible mechanisms for improving the radiation resistance of a material, there are several possible strategies. This chapter discusses modulations in the various pixel and epitaxial layer parameters. The following chapters discuss the results of experiments that changed the following design parameters and their impact on radiation hardness (verified experimentally by the IKF). An explanation of the parameters follows.

1. Pixel parameters:
    (a) Pixel size
    (b) Diode size
2. Epitaxial layer parameters:
    (a) Different resistivities
    (b) Various doping profiles
3. Depletion:
    (a) Increase of the depletion voltage
    (b) Changes of the diode geometry

4.1 Pixel parameters

4.1.1 Pixel size

There are various strategies for preserving the signal charge for collection. When only low-resistivity epitaxial layers were available, one approach was to shorten the diffusion paths of the signal electrons by reducing the pixel size[1]. Figure 2.6 visualizes a pixel, the pixel size and the diffusion path. Figure 4.1 shows the non-ionizing radiation hardness of different CMOS MAPS as a function of their effective pixel size. The differently colored bands group sensors with similar epitaxial layers and manufacturing technologies. The blue band represents the TowerJazz-0.18 µm manufactured sensors with $> 1\,\mathrm{k\Omega\,cm}$ epitaxial layers that were studied in this thesis. Chapter 5 discusses the effect of pixel size on the estimated non-ionizing radiation hardness of these sensors. Pixel size is an important parameter that significantly impacts many other sensor properties.

4.1.2 Diode size

The diode is a crucial component of every CMOS MAPS pixel. The purpose of n-doped insertion in the upper layers of a pixel is to collect signal charge carriers and forward them to the readout electronics. Technically speaking, a diode always consists of n-doped and p-doped materials, but sensor engineers often refer to the p-doped material as the "epitaxial layer" and call only the strongly n-doped implant above the epitaxial layer a "diode" (see Figure 2.6, page 25 for an illustration). This "diode" size can be varied to achieve the best possible radiation hardness. In general, the diode size and doping concentration impact depletion, CCE, noise, and overall radiation hardness. Section 5.3 extensively explores the impact of diode size on the non-ionizing radiation hardness of a sensor.

4.2 Epitaxial layer parameters

The epitaxial layer is the sensing volume in MAPS and is created via epitaxy before the CMOS manufacturing process. Non-ionizing radiation damage causes defects in the crystal structure of this layer. Signal electrons can then recombine with these defects (see Section 3.3), which decreases the signal amplitude and makes particle detection more difficult. Therefore, the lifetime of the signal electrons limits the radiation hardness of a conventional sensor. A change in the epitaxial layer has direct consequences for charge collection and radiation hardness. Consequently, multiple epitaxial layer parameters were explored to evaluate their effect on non-ionizing radiation hardness. The aim was to answer the following questions: How does the epitaxial layer thickness affect the signal? How do doping gradients impact the charge collection properties of CPS?

---

[1] also called pixel pitch.

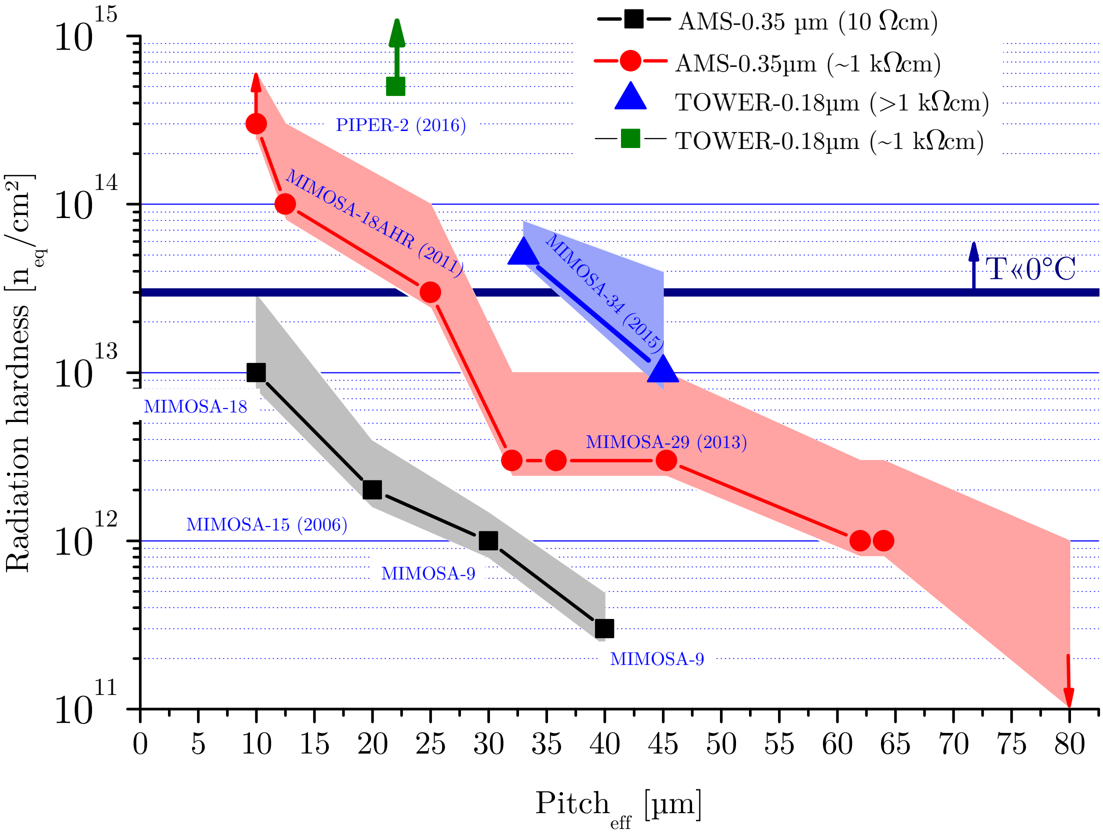

Figure 4.1: Effect of effective pixel pitch on non-ionizing radiation hardness for several generations of MIMOSA sensors. Color bands group sensors with similar epitaxial layers. The graphic is based on a previous design by [Doe15] and has been extended by this thesis (**blue** and **green**).

It was hypothesized that some sensors would be more efficient than others due to the influence of epitaxial layer thickness on the signal. A thicker epitaxial layer potentially produces more signal electrons, while at the same time the larger distance to the collecting diode could reduce the CCE due to more diffusion. In addition, the doping would affect the resulting electrical field and charge collection. There would be an optimal thickness and doping profile to achieve the most efficient charge collection.

To address these hypotheses, the charge collection properties of CPS with gradient[2] epitaxial layers and more conventional layers were compared. Efforts to build CPS with gradient low-resistivity epitaxial layers were mostly inconclusive [Koz11]. Section 4.2.1 focuses on results obtained from Fe-55 spectra. Section 4.2.2 discusses sensors with different doping profiles and a Sr-90 source.

---

[2] gradient doping: not constant dopant concentration, but gradually changing in dependance of sensor depth.

4.2.1 Impact of epitaxial layers on sensor performance

The radiation hardness of sensors built with low-resistivity epitaxial layers ranges from a few $10^{11}\,\mathrm{n_{eq}/cm^2}$ for pixel sizes of 40 µm to $10^{13}\,\mathrm{n_{eq}/cm^2}$ for diode distances of 10 µm [Dev08]. However, pixel size cannot be reduced arbitrarily because the manufacturing process limits the pixel design.

Smaller pixels imply a higher pixel density, which improves the spacial resolution of a detector, but this causes an increase in integration time since more pixels must be read per given area (for a rolling shutter readout). Furthermore, a higher pixel density requires higher power consumption, leading to more heat production. This surplus heat must be counteracted by more sophisticated cooling systems, which translates into a higher material budget, an undesirable outcome.

The MVD is expected to have an effective pixel size of about 28 µm [Dev+19] in order to keep time resolution and power consumption within acceptable limits. The gray stripe in Figure 4.1 illustrates that a pixel with this size and the required radiation hardness ($10^{13}\,\mathrm{n_{eq}/cm^2}$) cannot be achieved using 10 Ω cm low-resistivity epitaxial layer sensors [Doe15].

The radiation hardness improved by one order of magnitude when the active volume doping concentration was reduced. The AMS-0.35 µm ~1 kΩ cm high-resistivity epitaxial layers improved charge collection due to an increased depleted volume. Sensors manufactured with high-resistivity epitaxial layers have also been studied in [Doe15]. The non-ionizing radiation hardness of these sensors is shown as a **red band** in Figure 4.1. Although these devices were only partially depleted, their tolerance to non-ionizing radiation increased by one order of magnitude more than MAPS with low-resistivity epitaxial layers (**gray band**).

Next-generation sensors were introduced in 2015. Most of the sensors examined in this thesis were manufactured with the novel TowerJazz manufacturing process announced in 2013 [Tow13]. The epitaxial layer obtained in this process has a very high resistivity >1 kΩ cm. Unfortunately, the precise doping concentration and resistivity of an epitaxial layer is often kept secret by the manufacturer. Nevertheless, some data on the doping profile has been published and is used throughout this thesis. The extensively studied MIMOSA-34 sensor [DG10] features high-resistivity epitaxial layers of varying thicknesses. As such, the performance characteristics of a high-ohmic MIMOSA sensor can be studied as a function of its thickness and underlying doping profile.

MIMOSA-34

Each MIMOSA-34 sensor features 30 pixel matrices with varying properties, including pixel pitch, diode size, number of diodes per pixel, and pixel arrangement. All variations are listed in Table 4.1. The variety of parameters makes the MIMOSA-34 sensor an excellent candidate for charge collection tests and for exploration of charge collection dependence on pixel dimensions and diode parameters.

MIMOSA-34 sensors have a rolling-shutter readout with an adjustable readout clock of 2 to 10 MHz. The integration time t_{int} can be varied between 6.4 – 32 µs. Each of the 30 independent matrices has 64 rows and 16 columns of pixels. The 1024 matrix pixels are read out with a rolling shutter mode via 16 parallel analog outputs. The depletion voltage is fixed to ≈1.8 V. The pixel size in the matrices ranges from $27 \times 27\,\mu\text{m}^2$ to $33 \times 66\,\mu\text{m}^2$. The surface of the collection diode varies from 1 to $15\,\mu\text{m}^2$ [IPH18]. Some first beam test results were presented in [Sen+14]. All MIMOSA-34 measurements in this thesis were performed with an integration time of 32 µs.

The high-resistivity epitaxial layers in MIMOSA-34 sensors are either 18 µm or 20 µm thick (see Section 4.2.2) and, for this thesis, are denoted as HR18 and HR20, respectively. The sensors were all produced via the TowerJazz-0.18 µm manufacturing process. The chips were designed and submitted for production in March 2013 by the PICSEL group of the IPHC. Table 4.1 summarizes the different matrix features. Some of them will be discussed in the following experimental results.

Fe-55 γ-source study

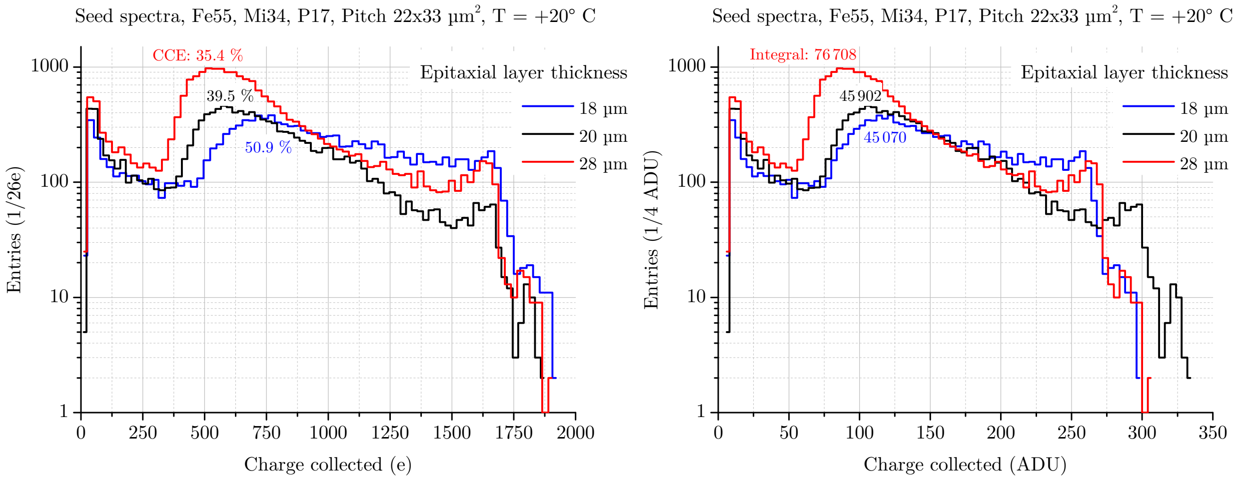

(a) Calibrated Fe-55 spectrum.

(b) Uncalibrated spectrum.

Figure 4.2: The Fe-55 spectrum of MIMOSA-34 sensors is strongly dependent on the thickness of the epitaxial layer, with strong variation in CCE and gain. The pixels were not depleted with high voltage ($U_{\text{dep}} = 1.8\,\text{V}$).
In (a) the numbers next to the peaks denote the measured CCE_1 values, in (b) the numbers show the calculated integral excluding hits with a measured signal $< 250\,\text{e}$.

The spectra in Figure 4.2 demonstrate the effect of different epitaxial layer thicknesses on the sensor response to the γ-spectrum of an Fe-55 source. All measured data were normalized to the same number of measurements[3]. The measured peaks from the thicker epitaxial layer had significantly more entries. The integral over

---

[3] Technically speaking - to the same number of recorded data frames.

Table 4.1: Description of all MIMOSA-34 pixel matrices, taken from the manual [IPH18].

Mimosa 34 description

SF Arrays structure

Pitch (y) = 33

Pixel	**P1**	**P2**	**P3**	**P4**	**P5**	**P6**	**P7**	**P8**	**P9**	**P10**	**P11**	**P12**	**P13**	**P14**	**P15**
Pitch (x)	33	44	66	33	44	66	33	44	66	33	44	66	33	30	27
N(D)	1	1	1	1	1	1	1	1	2	1	1	2	1	1	1
F(D)	15	15	15	11	11	15	11	11	15	11	11	11	11	11	11
S(D)	8	8	8	11	11	8	5	5	5	2	2	2	11	8	8
Pixel staggered		✓	✓		✓	✓		✓			✓			✓	✓
Others	DPW/8col			DPW/8col		LRT	DPW/8col			DPW	N_{diff}	N_{diff}	AC		FBD

Pitch (y) = 22

Pixel	**P17**	**P18**	**P19**	**P20**	**P21**	**P22**	**P23**	**P24**	**P25**	**P26**	**P27**	**P28**	**P29**	**P30**	**P31**
Pitch (x)	33	44	66	33	44	66	33	44	66	33	44	66	33	30	27
N(D)	1	1	1	1	1	1	1	1	2	1	1	2	1	1	1
F(D)	11	11	15	11	11	15	11	11	15	11	11	15	11	11	11
S(D)	11	11	15	8	8	8	2	5	5	2	1	2	11	8	8
Pixel staggered	✓	✓	✓	✓	✓	✓	✓	✓		✓	✓		✓	✓	✓
Others						LRT				N_{diff}	N_{diff}		FBD		

- N(D) = Number of sensing diodes in the pixel (1 or 2)
- F(D) = Footprint of diode, viz. section of volume in which the sensing diode is integrated : 15 or 11 µm^2
- S(D) = Surface of diode : 15, 11, 8, 5, 2 & 1 µm^2
- LRT = Large Reset Transistor : wide gate (2 time longers) against RTS noise
- Ndiff = Diode different that standard the Nwell, less deep
- FBD = Forward Bias Diode replacing reset transistor, (Self_Bias)
- DPW/8col = the first 8 columns are with full deep p-well except an opening of 8x8 µm bellow the diode

Table 4.2: Analysis of the spectra shown in figure 4.2. CCE$_1$ refers to the Charge Collection Efficiency of the seed pixel, CCE$_{25}$ of a whole cluster, see Section 2.5.2. The average charge collected $< \mathrm{CCE}_1 >$ is explained in Equation (4.3).

P17, Fe-55	CCE$_1$ [%]	$<$ CCE$_1$ $>$ [%]	CCE$_{25}$ [%]
HR18	50.9 ± 3.0	60.4 ± 2.6	100.0 ± 1.8
HR20	39.5 ± 2.7	49.4 ± 2.4	100.0 ± 1.9
HR28	35.4 ± 2.5	46.2 ± 2.3	100.0 ± 1.8

the complete seed pixel charge distribution of the thicker sensor was about 64 % larger than the integral of the charge distribution for the thinner sensors. The higher probability of γ photon conversion in the thicker sensor can explain the higher number of registered hits.

It is interesting to note that the gain of the 20 µm sensor is larger than that of the two other sensors. This is not attributable to the thickness of the epitaxial layer but rather to a difference in doping profile. In [Doe15], sensors with high- and low-resistivity layers of the same thickness were compared. The gain for the high-resistivity sensors shifted slightly toward a higher value than that of the low-resistivity sensors. However, it was only a 5 % shift, which could also be explained by manufacturing inaccuracies. However, the effect is more pronounced in Figure 4.2 and is therefore of interest. According to Section 2.5, larger gain reflects a smaller diode capacitance. Since the depletion voltage is the same for all sensors (approximately 1.8 V[4]), variation in the doping of the active volume must play a role (see Equation (2.1) and 6.3).

The HR18 sensor had the highest CCE$_1$, with a value of (50.9 ± 3.0) %. For a definition of how the CCE is measured and defined please see Section 2.5.2. In other words, it is likely that about 50.9 % of the signal electrons from hits in the epitaxial layer were collected only by the seed pixel. The summed CCE for a 5×5 pixel cluster, called the CCE$_{25}$, was 100 % for all sensors. Therefore, the HR20 and HR28 sensors require more pixels to accumulate the charge and collect all of the signal electrons created by the Fe-55 γ-source.

Based on previous studies and the extended measurement method “volume fractions of the charge collection” [Doe15, p. 86], the spectrum was divided into three regions, each representing one volume fraction (Figure 4.4). This method was used to compare the raw Fe-55 spectra, as well as directly compare the MIMOSA-18-AHR HR[5], MIMOSA-18-AHR LR[6], MIMOSA-26-AHR HR, and MIMOSA-26-AHR LR sensors from earlier studies with the MIMOSA-34 HR sensors and fully depleted

---

[4] $U_{\mathrm{dep}} = 1.8\,\mathrm{V}$ was taken from the MIMOSA-34 circuit diagram from the manual [DG10]; the measured laboratory value was $U_{\mathrm{dep.\,meas.}} = 2.2 \pm 0.1\,\mathrm{V}$. The diode built-in voltage U_{bi} was not included.

[5] **H**igh-**R**esistivity

[6] **L**ow-**R**esistivity

Pipper[7]-2 sensor studied in this thesis. The specified percentage indicates the size of the volume and the collection efficiency range relative to the total active volume. In other words, the calculated percentage is equal to the number of hits within the specified CCE range relative to the overall number of hits. Entries below a noise threshold of 300 e were not considered. This division allowed for a clearer interpretation of the findings in figure 4.2. The three areas were selected so that hits collected with a CCE_1 value between 15 - 40 % fall within the **range $\mathbf{V_<}$**. The lower limit (15 %) was chosen to exclude with a high certainty all fake hits. Hits collected with a higher CCE fall into the **$\mathbf{V_>}$ region**. A third region, the **$\mathbf{V_{100\,\%}}$ area**, contains the hits that converged directly in the depleted volume. In this region, almost 100 % of the charge was collected by the seed pixel. See Figure 4.3 for an illustration.

The seed spectrum of each sensor was divided into three sections:

A section for hits with 15 % < $\mathbf{CCE_1 < 40\,\%}$. These hits contribute to the **range $V_<$ region** fraction. Hits in this region were not collected efficiently by a single pixel.

A section for hits with 40 % ≤ $\mathbf{CCE_1 \leq 99\,\%}$. These hits contribute to the **$V_>$ region**.

A section for hits with a $\mathbf{CCE_1 > 99\,\%}$. Fe-55 hits that convert directly in the depleted volume are usually collected with a CCE_1 of 100 %. Depleted region hits were represented by the **$V_{100\,\%}$ region**. An efficient sensor should have as many hits as possible in this region.

Data for a non-irradiated chip was used to compile the plots of the MIMOSA-34 sensors in Figure 4.4. The P17 matrix was chosen; it has a pixel pitch of $22 \times 33\,\mu\text{m}^2$ and a diode surface of $11\,\mu\text{m}^2$ (see Table 4.1). Measurements were taken at room temperature (20 °C). The visualization simplifies the complexity of charge collection in a CMOS epitaxial layer, but it helps clarify the differences between the sensors under study. To count hits in the $V_{100\,\%}$ region, veto charge discrimination (described in detail in earlier studies and in Section 2.5.2) was applied. Only hits with signal electrons collected entirely by one pixel (i.e., >99 % CCE)) and no charge sharing among neighboring pixels were included. This analysis quantitatively determines the three fractions $V_<$, $V_>$ and $V_{100\,\%}$ of the active volume.

Compared to the MIMOSA-18-AHR, the MIMOSA-26 sensors [Doe15, p. 86], and Figure 4.5, the MIMOSA-34 sensors studied in this section had a larger fraction of $V_>$ hits collected with over 40 % CCE. The A0 matrix of the MIMOSA-18-AHR HR sensor accumulated the greatest percentage of charge in [Doe15]. In the following section, this sensor is compared to the MIMOSA-34 sensor studied in this thesis.

Although the MIMOSA-18-AHR HR sensor had an epitaxial layer thickness of 15 µm and a pixel size of 10 µm [IPH18, Mi18AHR description], the fraction of

---

[7] **P**ixelated sensor for Ionizing **P**article and **P**hotons **E**nergy **R**esolved detection

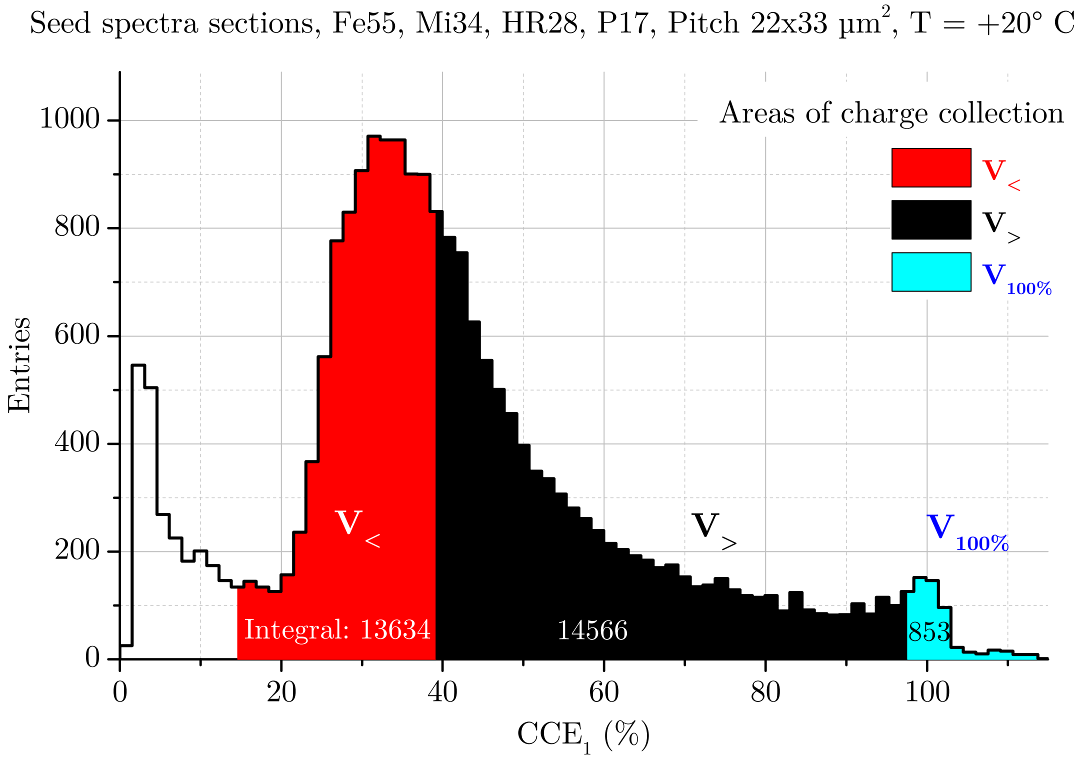

Figure 4.3: Hits from the sensor seed spectra were assigned to different CCE areas, as shown, to compare the sensors studied here to those from previous studies. The numbers denote integral values for relative comparison. Figure 4.4 presents the relative hit count of each region based on these integral values.

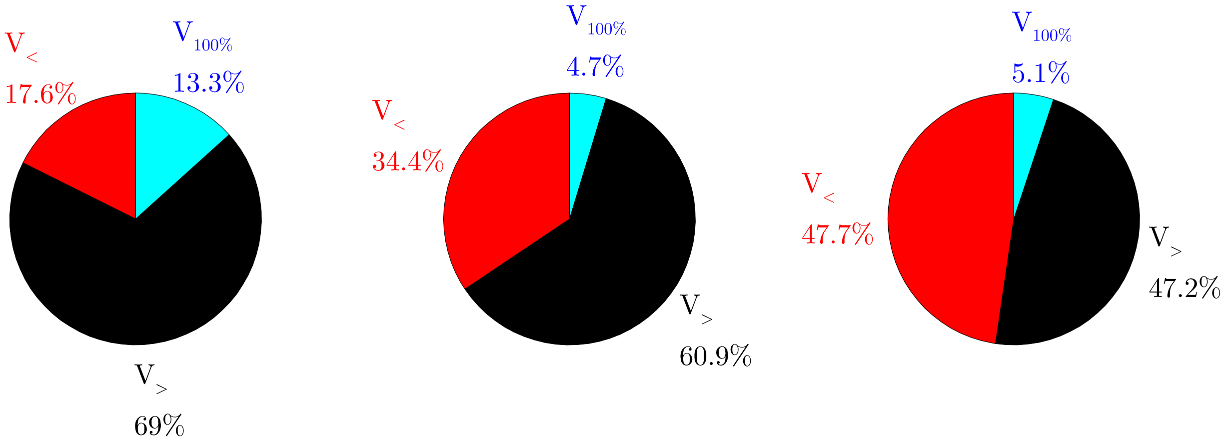

(a) 18 µm (b) 20 µm (c) 28 µm

Figure 4.4: Zone share of the total active volume for different epitaxial layer thicknesses in the P17 pixel matrix (pitch$_{eff.}$ = 26.9 µm) of the MIMOSA-34 sensors. Please see text for an explanation and discussion.

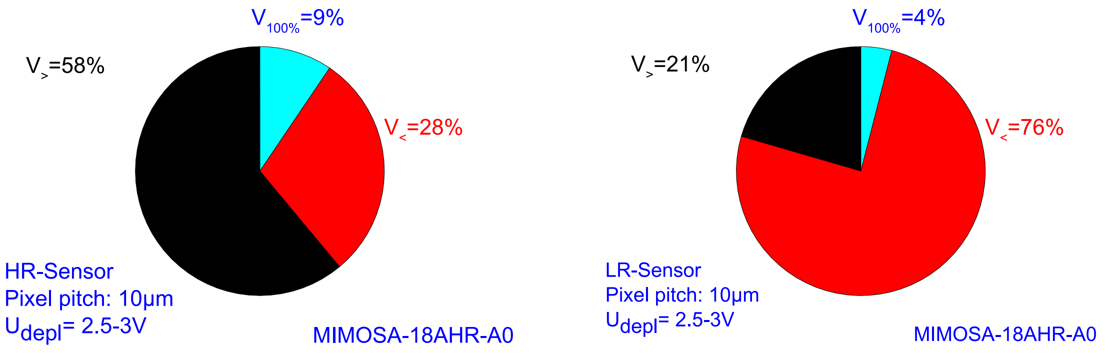

(a) MIMOSA-18-AHR HR-Sensor 10 µm **(b)** MIMOSA-18-AHR LR-Sensor 10 µm

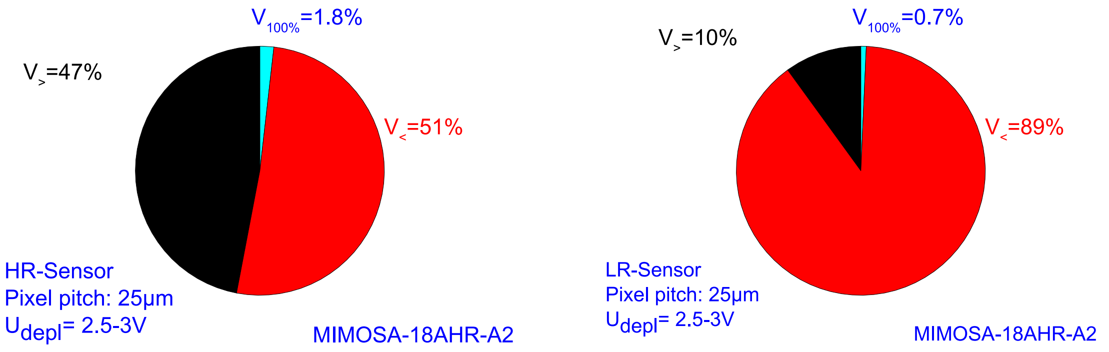

(c) MIMOSA-18-AHR HR-Sensor 25 µm **(d)** MIMOSA-18-AHR LR-Sensor 25 µm

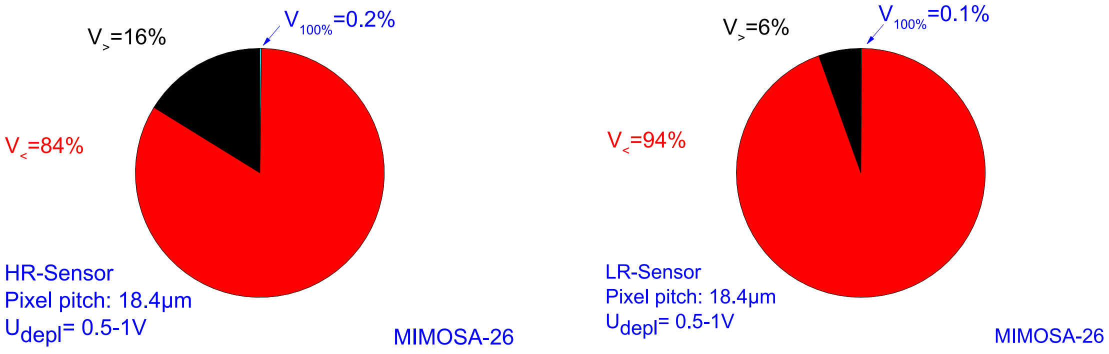

(e) MIMOSA-26-AHR HR-Sensor **(f)** MIMOSA-26-AHR LR-Sensor

Figure 4.5: MIMOSA-18-AHR zone shares of the active volume, taken as it is from [Doe15]. Shown to compare with sensors studied in this thesis (Figure 4.4). The epitaxial layer thickness of the MIMOSA-18-AHR HR sensor was 15 µm, and that of the LR sensor was 14 µm. The MIMOSA-26 sensors had thicknesses of 10 - 15 µm. For details on the measurement please see [Doe15].

hits collected with over 40 % CCE was 67 %; the fraction of hits detected with a CCE_1 of at least 40 % for the 18 µm MIMOSA-34 sensors was over 82 %. The P17 matrix in the MIMOSA-34 sensors had an effective pixel pitch of 27 µm, almost three times larger than that of the A0 pixel matrix. There are two antagonistic effects. The thinner epitaxial layer of the MIMOSA-18-AHR HR sensor shortens the average signal electron path length along the longitudinal axis (thickness) of the sensors; this shortening helps a single pixel collect the electrons more efficiently and should increase the CCE_1 value. However, the shorter distance between adjacent collecting diodes facilitates charge sharing between neighboring pixels, which should reduce the measured CCE_1 value of the individual pixel under examination. Note that the MIMOSA-18 HR A0 pixel matrix had a larger diode surface (14.6 μm^2) and a higher depletion voltage $U_{depl.} \approx 2.5\,\text{V}$) than the MIMOSA-34 P17 matrix, which had a diode surface of 11 μm^2 and a depletion voltage $U_{depl.} \approx 1.8\,\text{V}$.

The difference in the fraction of charge collection shown in Figure 4.4 may also emerge from differences in the epitaxial layers. The improvement in charge collection may be explained by the enhanced epitaxial layer that was used for the MIMOSA-34 sensors. In the next subsection, the active volume is discussed further.

4.2.2 Doping profiles

The signal electrons are guided along these electrical field lines. If the direction of the doping concentration gradient and the electrical field is correct, this results in a shortening of the mean path length to the diode and thus in an improved radiation hardness.

Figure 4.6a shows the doping concentration of the MIMOSA-34 sensors as a function of depth. The following equation calculates the built-in voltage U_{bi} between two layers with different doping concentrations n_1 and n_2 [Dep02, Equations 4-19]:

$$U_{\text{bi}} = \frac{k_{\text{B}}T}{e} \ln\left(\frac{n_{\text{subst.}}}{n_{\text{epi}}}\right) \tag{4.1}$$

U_{bi}	built-in potential
k_{B}	Boltzmann constant, $8.617\,33 \times 10^{-5}\,\text{eV/K}$
T	Temperature
e	electron charge
$n_{\text{subst.}}$	substrate doping concentration
n_{epi}	epitaxial layer doping concentration

To calculate the electrical field at a certain epitaxial layer depth z, the derivative of Equation (4.1) can be found in one dimension along the z-axis:

$$\begin{aligned} E = \frac{\partial U_{\mathrm{bi}}}{\partial z} = \frac{k_{\mathrm{B}} T}{e} \frac{\partial}{\partial z} \ln\left(\frac{n_{\mathrm{subst.}}}{n_{\mathrm{epi.}}(z)}\right) = \\ c \cdot \frac{\partial}{\partial z} \ln\left(\frac{n_{\mathrm{subst.}}}{n_{\mathrm{epi.}}(z)}\right) = -c \cdot \frac{n'_{\mathrm{epi.}}(z)}{n_{\mathrm{epi.}}(z)} \quad \text{, where} \\ c \quad \text{is a constant factor,} \\ n'(z) := \frac{\partial n(z)}{\partial z} \quad \text{and} \\ n_{\mathrm{epi.}}(z) \quad \text{is the doping concentration } n \text{ of the epi at depth } z. \end{aligned} \tag{4.2}$$

In this toy model, which is only valid in the first order in case of full depletion, the electrical field E is proportional to the derivative of the dopant concentration $n'(z)$ and the doping concentration at this point $n(z)$. Figure 4.6b compares the calculated electrical field strength at different epitaxial layer depth for the different doping profiles. The doping profiles in Figure 4.6a are roughly similar in trend but considerably different in the details. For small z-values at the point of origin, the p-well is responsible for the high doping concentration. Then the doping concentration drops sharply for all three sensors. After that point, the doping profiles for the HR18 and HR20 sensors rise monotonously, while the doping profile for the HR28 sensors has a broad minimum. The collecting diode D_{col} is located on the left side of the abscissa in the doping profiles shown in Figure 4.6a. Given the experimental results in Figures 4.4 and 4.2, a monotonously rising doping gradient of the HR18 and HR20 sensors seems beneficial for efficient charge collection. Since the MIMOSA-34 sensors were not fully depleted, the signal charge collection may occur via the global electrical fields of the depleted region and also via local drift fields between different doping concentration layers induced by ionized dopants. The minimum valley in of low dopant concentration in Figure 4.6a of the HR28 sensors indicates no beneficial electrical fields towards the diode in this region. However, the 28 µm sensor is 10 µm thicker than the 18 µm sensor and 8 µm thicker than the 20 µm sensor. Because the depletion voltage is identical for all of the three sensors, a larger fraction of the active volumes of the 18 µm and 20 µm sensors have a CCE_1 over 40 %.

To better account for the different thicknesses of the sensors, the percentage values from Figure 4.4 can be converted into absolute numbers with micrometers as the unit. Under the widely used assumption of a flat PN junction, the different CCE regions are superimposed layers. This simplification reduces the variance of the complex electrical fields in the epitaxial layer to one dimension and is only valid in the first order. By multiplying the values from Figure 4.4 with the corresponding total thickness of the sensor, the thickness of the layer with the corresponding CCE can be determined with this simple one-dimensional model. Table 4.3 compares the thicknesses of the three regions of the different sensors.

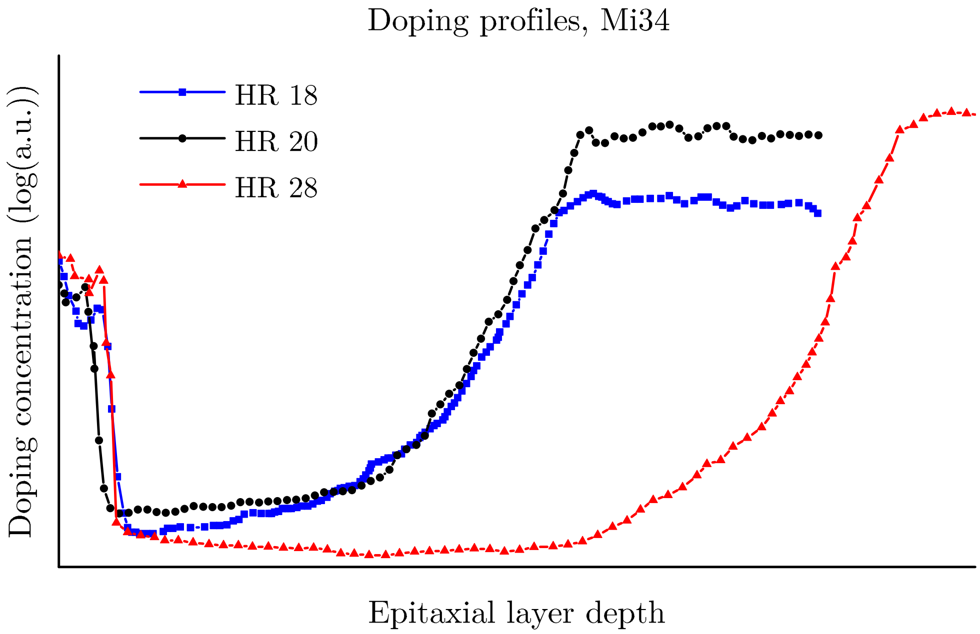

(a) The MIMOSA-34 sensors differ in epitaxial layer thickness and also in doping profile. The ordinate shows the doping concentration on a logarithmic scale, while the abscissa shows the longitudinal position along the epitaxial layer measured from the diode. The data was compiled from [Dev15].

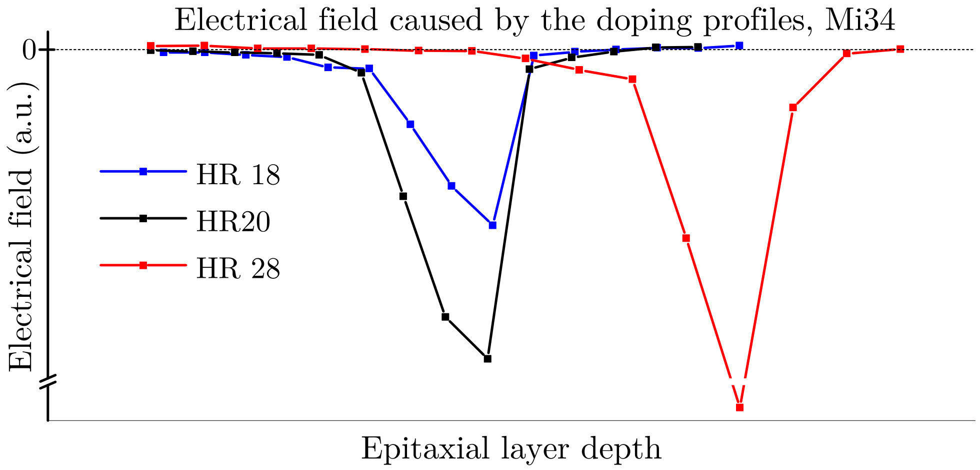

(b) The electrical field strength on a linear scale formed by the doping profiles of the three MIMOSA-34 sensors (Figure 4.6a). The abscissa shows the longitudinal position along the epitaxial layer, as in Figure 4.6a. Calculated using Equation (4.2).

Figure 4.6

Table 4.3 shows that the HR28 sensor has the largest region of low charge collection efficiency $V_<$. Nevertheless, its region of high charge collection is comparable to the other two sensors' region sizes. This finding fits the hypothesis that signal electrons created in deeper regions of the sensor are more likely to be shared between neighboring pixels. Besides this finding, Table 4.3 indicates that the HR18

Table 4.3: Layer thicknesses for differing CCE$_1$ under a simple PN flat junction depletion assumption. Values from Figure 4.4 were multiplied by the thickness of the active volume of the corresponding MIMOSA-34 sensor. The values represent depletion depths under the one-dimensional flat PN junction assumption.

all numbers in µm	HR18	HR20	HR28
$V_{100\,\%}$	2.4	0.9	1.5
$V_{>} + V_{100\,\%}$	14.8	13.1	14.7
$V_{<}$	3.2	6.9	13.4

sensor has the most extensive high charge collection region for non-irradiated chips.

Sr-90 β-source study

Figure 4.7 shows the signal response of non-irradiated MIMOSA-34 chips to a Sr-90 β-ray source. Section 2.5.3 details the relevant methodology. A Landau fit on the seed spectrum was used to determine the MPV of the collected charge. The 18 µm sensor had the thinnest epitaxial layer of the sensors examined and therefore had an MPV of (625.0 ± 30.5) e. The HR28 sensor was 55.6 % thicker than the 18 µm sensor, collected approximately 49.3 % more charge, and had an MPV of (933.0 ± 40.5) e. The 20 µm sensor was 11.1 % thicker epitaxial layer than the 18 µm sensor and collected approximately 11.0 % more charge. This aligns with the calculated theoretical values.

The Sr-90 source used in this experiment was weak, leading to a sizable statistical error in the data. Although data collection for each matrix took 5 (HR20) to 12 (HR18) hours, the entry fluctuations in Figure 4.7 are visible. In addition, the differences in the measured MPVs, especially between the HR18/HR20 and HR28 sensors, are significant.

Another observable is the average collected charge $\langle Q_{\text{coll.}} \rangle$, which is defined as

$$\langle Q_{\text{coll.}} \rangle = \frac{1}{N_{\text{hits}}} \int_{\text{N.b.}}^{\infty} f(Q) Q \, \mathrm{d}Q \quad \text{, with} \tag{4.3}$$
$$N_{\text{hits}} = \int_{\text{N.b.}}^{\infty} f(Q) \, \mathrm{d}Q \quad \text{, where}$$

$\langle Q_{\text{coll.}} \rangle$	is the average collected charge,
N.b.	(noise border) is the threshold value for hits, set to 200 e in Table 4.4,
$f(Q)$	is the collected charge distribution shown in Figure 4.7, and
Q	denotes the collected charge.

Note that the average collected charge $\langle Q_{\text{coll.}} \rangle$ does not necessarily coincide with the collected MPV discussed above. The HR28 sensor was 55.6 % thicker and collected, on average, 36.7 % more charge than the HR18 sensor. The MPV scaled with sensor thickness, but the average collected charge $\langle Q_{\text{coll.}} \rangle$ did not.

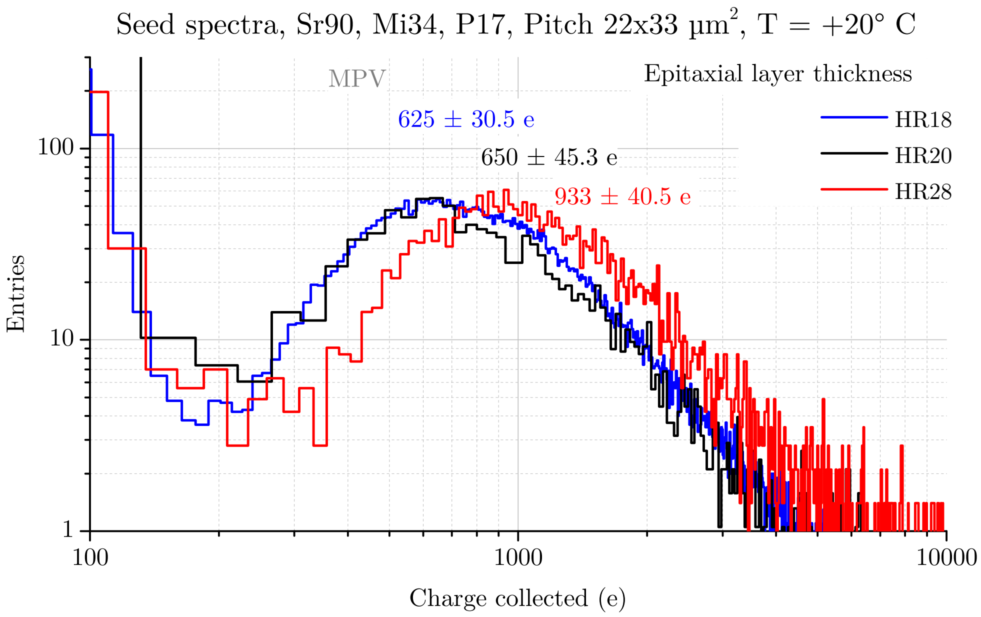

Figure 4.7: The Sr-90 β-ray source signal responses for the three non-irradiated MIMOSA-34 sensors with different thicknesses. The spectra were scaled so that all three had the same number of recorded frames. The MPV of the collected charge in electrons is provided.

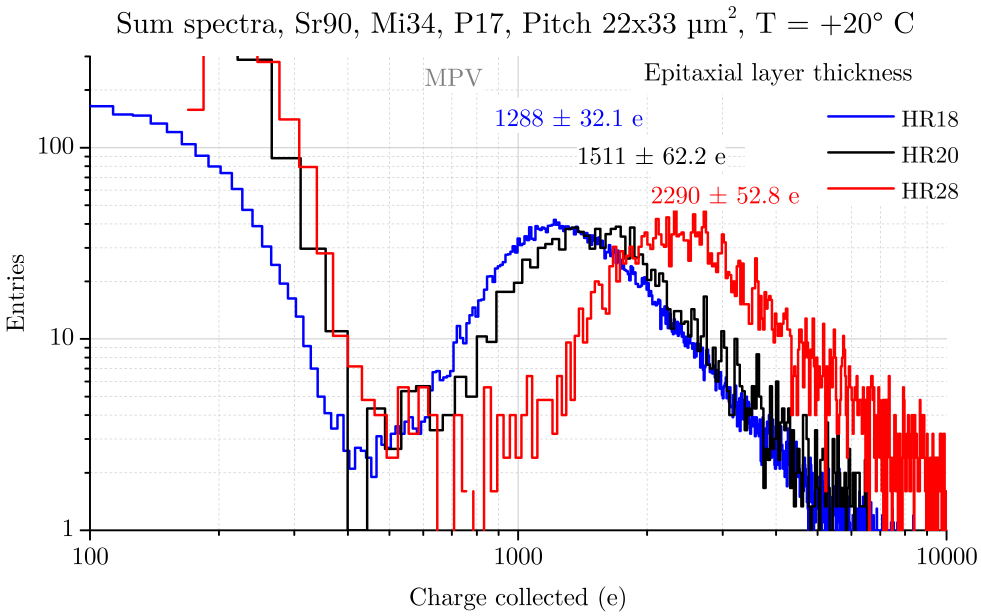

Figure 4.8: The Sr-90 β-ray source signal responses for 5×5 pixel clusters of three non-irradiated MIMOSA-34 sensors with different thicknesses. For the spectra of single pixels, see Figure 4.7.

Table 4.4: Analysis of the Mi34 spectra shown in Figures 4.7 and 4.8.

P17, Sr-90	MPV [e]	Noise [e]	S/N	$\langle Q_{\text{coll.}} \rangle$ [e]	MPV$_{25}$ [e]
HR18	625.0 ± 30.5	11.7	53.4 ± 2.6	1358.3 ± 25.2	1288.0 ± 32.1
HR20	650.0 ± 45.3	11.8	55.1 ± 3.8	1320.8 ± 76.7	1511.0 ± 62.2
HR28	933.0 ± 40.5	12.0	77.8 ± 3.4	1857.3 ± 49.3	2290.0 ± 52.8

Table 4.4 summarizes the findings of the β-source study. The measured noise did not depend on sensor thickness since the sensors were not irradiated. Therefore, the S/N ratio was the highest for the thickest sensor, which collected the most charge. A β particle creates on average 80 electron-hole pairs per one µm of traversed silicon. The $\langle Q_{\text{coll.}} \rangle$ value of (1358.3 ± 252.0) e for the HR18 sensor divided by the 80 electron/hole pairs per µm generated suggests an average traversed β path of (17.0 ± 0.3) µm, which approximately fits with sensor thickness. Some charge sharing occurred, which lowered the average $\langle Q_{\text{coll.}} \rangle$ value. This discrepancy is large for the HR28 sensors. The β particles indicate wrongly a thickness of (23.2 ± 0.6) for the 28 µm thick sensor. The higher charge sharing probably distributed the generated signal electrons to the neighboring pixels. Figure 4.8 shows the collected charge of a whole 5×5 cluster. As expected the cluster collected the missing charge. Table 4.4 summarizes the MPV$_{25}$ values for the cluster. A division of these values by 80 electron-hole pairs per micrometer almost matches the thicknesses of the sensors. The deduced thickness was slightly underestimated for the HR18 and HR20 sensors at (16.1 ± 0.4) µm and (18.9 ± 0.8) µm, respectively, and slightly overestimated for the HR28 sensor at (29.9 ± 0.7) µm. Based on the ratio of MPV to MPV$_{25}$, the thin HR18 sensor proportionally collected the most charge in its seed pixel (MPV/MPV$_{25}$ $= 0.49 \pm 0.03$), as was expected given its higher CCE$_1$. The MPV/MPV$_{25}$ ratio for the HR20 sensor is 0.43 ± 0.03 and the ratio for the HR28 sensor is 0.39 ± 0.02, the lowest of the three. The thick sensor collects the least charge in its seed pixel proportionally, but in terms of absolute charge value, it collects the most.

Summary of studies on sensors with different epitaxial layers

The studies on sensors of varying thicknesses and doping profiles are summarized as follows (see Figure 4.9, as well):

CCE$_1$: The thinnest HR18 sensor, as expected, had the highest CCE$_1$. The signal charge generated by the Fe-55 γ-radiation was, on average, closer to the collecting diode for thinner sensors. Moreover, the HR18 sensor benefited from its ramp doping profile. Therefore, the average signal electron collection time was shorter for the thinner sensor. This caused less charge sharing with neighboring pixels and was measured as a higher CCE$_1$ value. A cluster of 5×5 pixels collected 100 % of the Fe-55 K$_\alpha$ γ-induced electrons for all of the sensors.

MPV: The signal response of charge generated along the β-particle track was studied using a Sr-90 β-source. Each hit should create signal electrons distributed

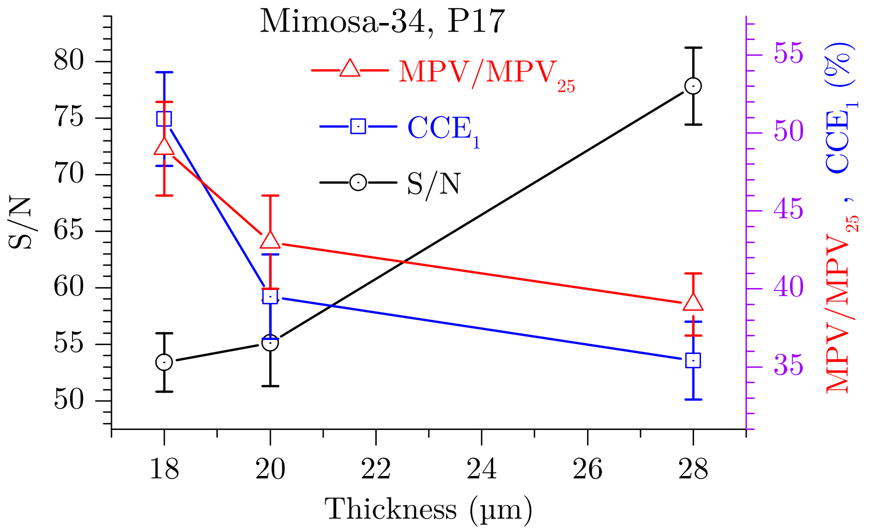

Figure 4.9: A compilation of CCE$_1$ values from the Fe-55 γ-source, as well as the S/N and MPV/MPV$_{25}$ ratios from the Sr-90 studies on MIMOSA-34 sensors of varying thickness. The abscissa shows the sensor thickness. The right ordinate is shared by the CCE$_1$ and MPV/MPV$_{25}$ data. Error bars calculated from error propagation of the standard deviation of the fits.

over the entire thickness of a sensor. The number of electrons generated was solely dependent on the thickness of the epitaxial layer. The MPV was the highest for the HR28 sensor and lowest for the HR18 sensor. Because the noise was almost the same for all of the non-irradiated sensors, the higher signal amplitude indicates a higher S/N ratio. Therefore, the S/N ratio was the highest for the HR28 sensor.

MPV$_{25}$: In general, the 5×5 pixel clusters collected more charge than the single pixels. The MPV/MPV$_{25}$ ratio was the highest for the HR18 sensor. It collected the most charge for a cluster in the seed pixel, which was implied by its high CCE value. The 28 µm sensor spread out the charge within a cluster the most. This was confirmed by the low measured CCE value (see Figure 4.9).

Sensors with an HR18 layer demonstrated a better CCE than sensors with HR20 epitaxial layers. This was especially true in the high signal region, where the HR18 sensor exhibited a swift transition from charge collection via diffusion to charge collection via drift fields. The signatures observed in the spectra may be explained quantitatively using the known doping profiles of the manufacturing processes. Nevertheless, the results remain qualitative, as more detailed discussions would require TCAD simulations. However, gradient fields may slightly improve the non-ionizing radiation hardness of CPS.

Chapter 5

Fast neutrons

> *"I am afraid neutrons will not be of any use to anyone."*
>
> SIR JAMES CHADWICK

In heavy-ion experiments, micro-vertex-detectors are placed near the interaction point, where the sensors will be exposed to very high particle fluxes and high radiation doses. This position is necessary for discriminating short-lived open charm particles from the primary collision point (i.e., the place of particle production) by their secondary decay vertices. These circumstances require detector systems that can withstand the extreme rate capability, momentum, spatial resolution and radiation hardness requirements. Chapter 3 discussed the destructive effect of different particle radiations on matter and silicon sensors. This chapter focuses on fast neutrons, which mostly cause non-ionizing radiation damage (Section 3.2, page 40). This damage scales approximately according to the NIEL model (Figure 3.1 and Equation (3.2)). Other non-ionizing particle damage can be rescaled and compared according to the NIEL model. MIMOSA-34 sensors, introduced in Section 4.2.1, were used for the fast neutron experiments. Table 4.1 summarizes the matrix features of the MIMOSA-34 sensor. In particular, this chapter investigates the dependence of non-ionizing radiation hardness on the following parameters:

1. Epitaxial layer parameters:
   (a) Epitaxial layer thickness and doping profile
2. Pixel parameters:
   (a) Diode size
   (b) Pixel pitch

First, the radiation hardness factors for HR18 and HR20 sensors were compared. Then, the CCE values of the HR18 sensor were compared to those of the HR20 sensor, and the non-ionizing radiation hardness limits were estimated for a 33×33 μm^2 P1 pixel matrix and a 33×66 μm^2 P3 pixel matrix. The chapter ends with an evaluation of the impact of diode size on sensor performance. An optimal compromise must be found between overly small diodes with low noise but poor CCE and overly large diodes with excellent CCE but high noise.

5.1 HR18 vs. HR20

Sensors with an HR18 epitaxial layer have a different epitaxial layer doping profile than sensors with an HR20 layer (Figure 4.6a). This subsection explores the signal responses of these sensors after irradiation with a dose of $10^{13}\,\mathrm{n_{eq}/cm^2}$. Different pixel sizes were chosen to analyze the impact of doping profile and pixel size. The latter was considered because of readout speed gains when using bigger pixels. P17 pixels were the smallest pixels studied, with a pixel pitch of $33 \times 22\,\mu\mathrm{m}^2$; P3 pixels were the largest studied, with a pitch of $33 \times 66\,\mu\mathrm{m}^2$; they are almost twice the size of the P17 pixels. Larger pixel pitches signify longer distances between collecting diodes. This results in longer diffusion paths, which means signal electrons can diffuse into neighboring pixels more easily. This dispersion reduces the CCE_1.

Prior to irradiation, the single pixel CCE (CCE_1) for the P17 pixel matrix was estimated at 50.9 % for the HR18 sensor and at 36.6 % for the HR20 sensor (figure 4.2 on page 53). For the P1 pixel matrix, the unirradiated CCE_1 was 40.5 % for the HR18 and 34.6 % for the HR20 sensor. For the larger P3 pixel, the CCE_1 was estimated at 36.0 % for the HR18 sensor and at 32.6 % for the HR20 sensor. The HR18 epitaxial layer had a higher CCE overall. Figure 4.2 shows that the pixels of the P17 matrix in the HR18 sensor had a higher CCE_1 than the P17 matrix in the HR20 sensor. This is in agreement with the unirradiated epitaxial layer studies in Section 4.2.1. The sum of CCE values for a 5 × 5 pixel cluster (CCE_{25}) was 100 % for all unirradiated matrices, regardless of their pixel pitch. Tables 5.1 and 5.2 summarize the findings.

Table 5.1: Before irradiation — After $10^{13}\,\mathrm{n_{eq}/cm^2}$

	Before irradiation			After $10^{13}\,\mathrm{n_{eq}/cm^2}$	
HR18	P17	P1	P3	P1	P3
T (°C)	21	20	21	-63	-63
$\mathrm{Pitch}_{eff.}$ (µm)	26.9	33	46.7	33	46.7
CCE_1 (%)	50.9	40.5	36.0	36.1	28.4
CCE_{25} (%)	100	100	100	88.4	70.8
Noise (e)	11.7	11.8	11.7	11.6	10.7

Table 5.2: Before irradiation — After $10^{13}\,\mathrm{n_{eq}/cm^2}$

	Before irradiation			After $10^{13}\,\mathrm{n_{eq}/cm^2}$		
HR20	P17	P1	P3	P17	P1	P3
T (°C)	-15	-15	-12	-15	-15	-15
$\mathrm{Pitch}_{eff.}$ (µm)	26.9	33	46.7	26.9	33	46.7
CCE_1 (%)	36.6	34.6	32.6	34.7	29.0	23.4
CCE_{25} (%)	100	100	100	88.5	77.6	60.0
Noise (e)	15.3	11.6	10.8	15.7	12.0	11.5

After the sensors are irradiated with $10^{13}\,\mathrm{n_{eq}/cm^2}$, the CCE decreases. This is likely because signal electrons become unavailable through recombination with defects created by the fast neutron radiation. The $\mathrm{CCE_1}$ and $\mathrm{CCE_{25}}$ values in Table 5.2 imply that the HR18 layer performs better than the HR20 layer. This indicates that the HR18 sensor has fewer vulnerabilities to signal charge loss than the HR20 sensor. Figure 5.1 depicts a zone share of the total active volume of the irradiated P17 matrix which illustrates these findings.

Only measurements at about 20 °C were available for the unirradiated HR18 sensors, but at −63 °C for the irradiated HR18 sensors. To separate temperature effects from radiation damage effects, Figure 5.2 presents the raw signal response spectra at these temperatures for the closely related HR20 layer. The temperature reduced the $\mathrm{CCE_1}$ by $(4.5 \pm 0.8)\,\%$, while radiation damage reduced the $\mathrm{CCE_1}$ by $(7.8 \pm 0.7)\,\%$.

5.2 Non-ionizing radiation dose limit

Since the HR18 layer performed better than the other layers, I focus on maximizing sensor non-ionizing radiation hardness with this epitaxial layer and with no external higher depletion voltage. Chapter 6 addresses sensors with a depletion voltage above 1.8 V.

A detector is assumed to be sufficiently radiation-hard if it has a S/N ratio > 15. Noise and β spectra were measured before and after irradiation to calculate the S/N ratio. It is important that no hits are lost, as this could produce a higher S/N ratio than is accurate. Therefore, it was checked that the number of hits before and after irradiation were about the same and that these hits were not caused by background noise. The noise spectrum was recorded separately for this purpose.

MIMOSA-34 sensors (THR) with HR18 epitaxial layers were exposed to non-ionizing radiation doses of 10^{13}, 5×10^{13} and $10^{14}\,\mathrm{n_{eq}/cm^2}$.

5.2.1 $10^{14}\,\mathrm{n_{eq}/cm^2}$ dose for the P1 pixel matrix

Figure 5.4 shows the recorded single pixel signal response spectrum for a Sr-90 β-source. The no-source spectrum was subtracted to study the effects of differing threshold borders. The S/N ratio of the P1 pixel matrix of the MIMOSA-34 sensor was 23 after irradiation with $10^{14}\,\mathrm{n_{eq}/cm^2}$ (see Figure 5.4 and 5.3). To confirm that no hits were lost due to the high irradiation, the integral of the recorded β spectrum was calculated. The integral over the collected charge distribution corresponds to the number of detected hits and is calculated using a fixed value to prevent noise hits from being counted as hits. This threshold value can be used as a hit trigger level in digital readouts.

Two independent measurements were made for each sensor to study the background noise and the signal separately. One measurement was taken with the

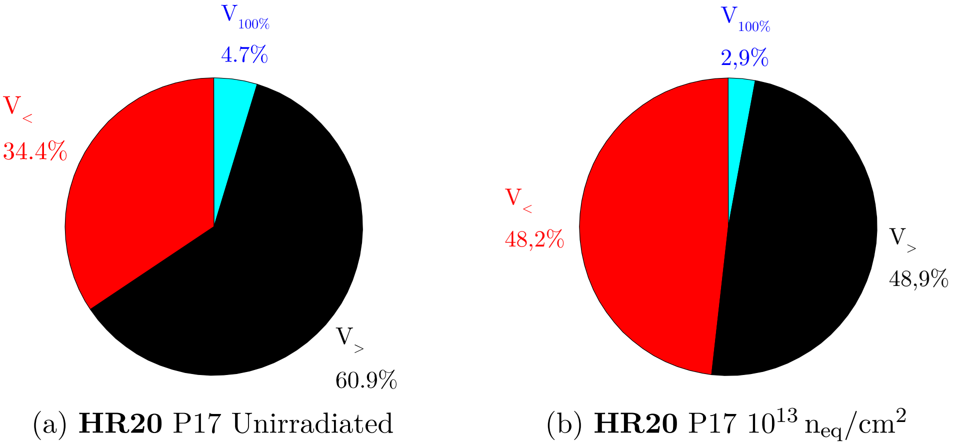

(a) **HR20** P17 Unirradiated (b) **HR20** P17 $10^{13}\,\mathrm{n_{eq}/cm^2}$

Figure 5.1: Zones share of the total active volume for the HR20 P17 matrix ($\mathrm{Pitch}_{eff.} = 26.9\,\mu\mathrm{m}$) of MIMOSA-34 sensors with different irradiation. (a) is taken from figure 4.4 for comparison.

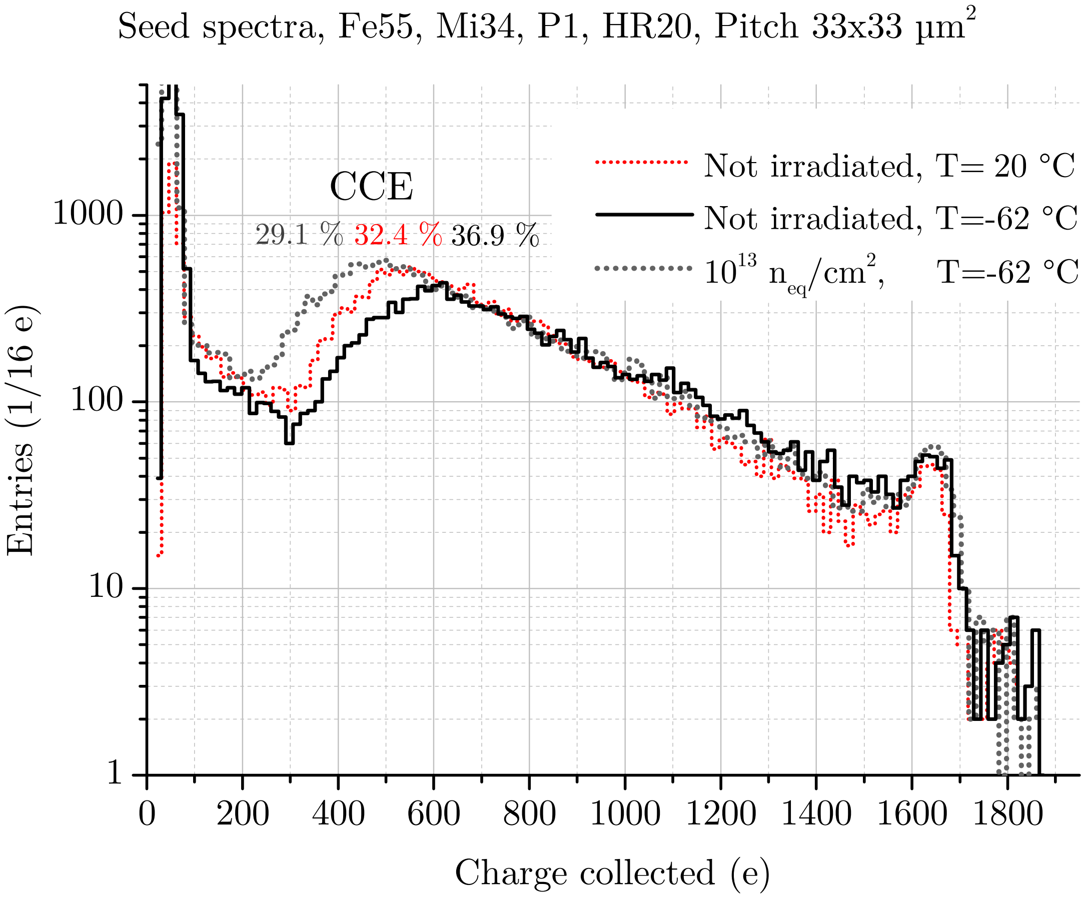

Figure 5.2: A calibrated Fe-55 HR20 spectrum. The percentage numbers next to the peaks denote the CCE_1 values.

Sr-90 source, and the other measurement was taken under similar conditions, but without any artificial source to record the noise only. With the Sr-90 source, the noise spectrum was assumed to be mixed into the full recorded spectrum. To ensure that the noise did not mimic any hits, the measurement without the Sr-90 source was defined as the noise background and subtracted from the Sr-90 spectrum. All hits from the background spectrum were considered fake hits, and any hits remaining after noise subtraction were considered signal hits. The subtraction allowed for study of how the percentage of signal and noise hits depended on the threshold border. If the threshold border was set too high, there was a significant number of undetected signal hits, but if the threshold border was set too low, there was a significant number of fake hits. Therefore, the threshold must be correctly selected for a strongly irradiated sensor when the S/N separation gap becomes smaller. In Figure 5.4, the fixed threshold was set to 92.4 e (i.e., the estimated noise border). Only about 1 % of all recorded hits appeared to be below this limit, and the fake hit rate was 4.3×10^{-6} with this threshold.

Figure 5.5 summarizes the rate of fake hits and lost signal hits for varying threshold values. It indicates that the number of detected hits does not depend heavily on the selected threshold in the range of 77 e to 123.2 e. In this range, the detection efficiency is close to 100 %. Figure 5.5 also shows how detection efficiency drops rapidly when the threshold value is set above about 200 e for the $10^{14}\,\mathrm{n_{eq}/cm^2}$ irradiated sensor. The non-irradiated sensor had good detection efficiency for threshold values of up to about 700 e. This threshold-dependance underlines the importance of carefully choosing an appropriate threshold value for heavily irradiated CPS.

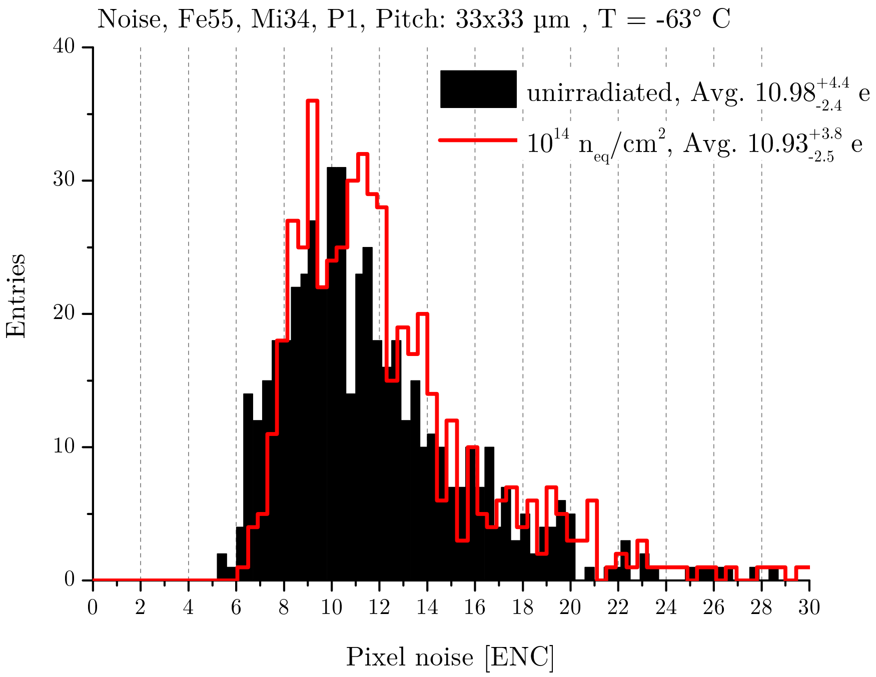

Figure 5.3: A comparison of the noise per pixel distribution of non-irradiated and $10^{14}\,\mathrm{n_{eq}/cm^2}$ irradiated P1 pixels.

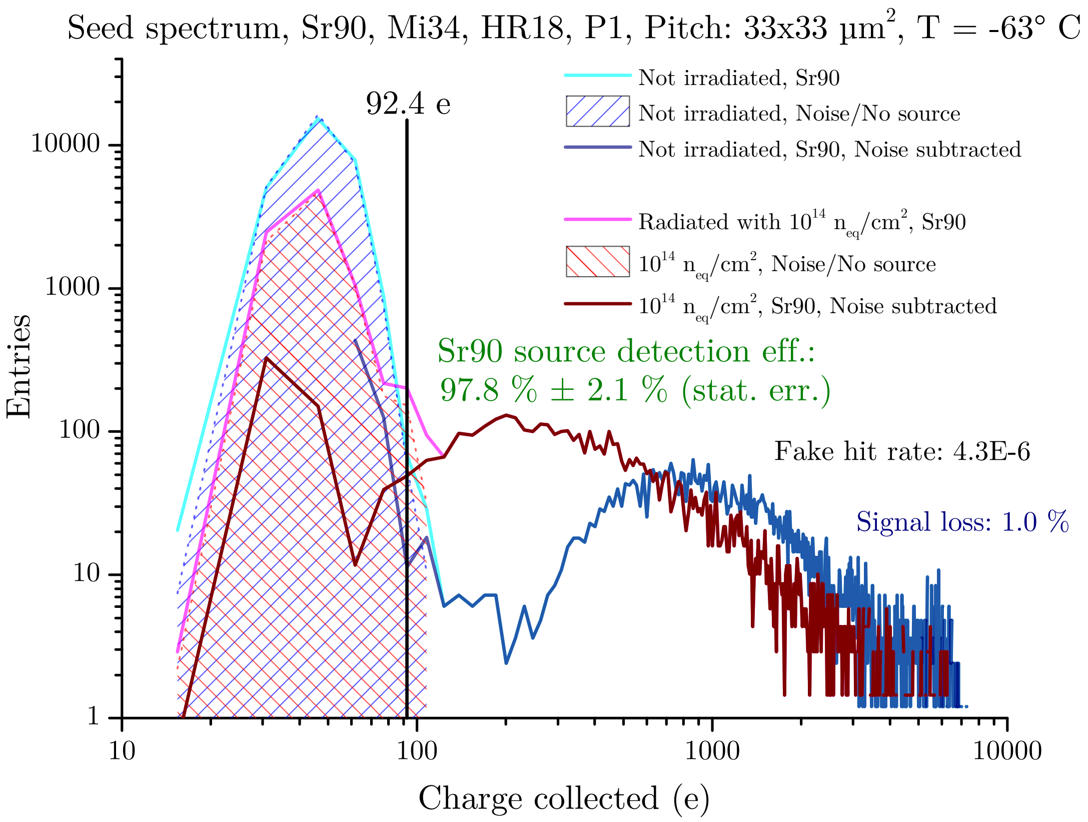

Figure 5.4: β-spectra for non-irradiated and $10^{14}\,\mathrm{n_{eq}/cm^2}$ irradiated P1 pixels. The "Noise/No source" spectra are used for background subtraction to measure the fake hit rate, it is recorded under same conditions, but with no signal source. The fixed noise threshold is set to 92.4 e.

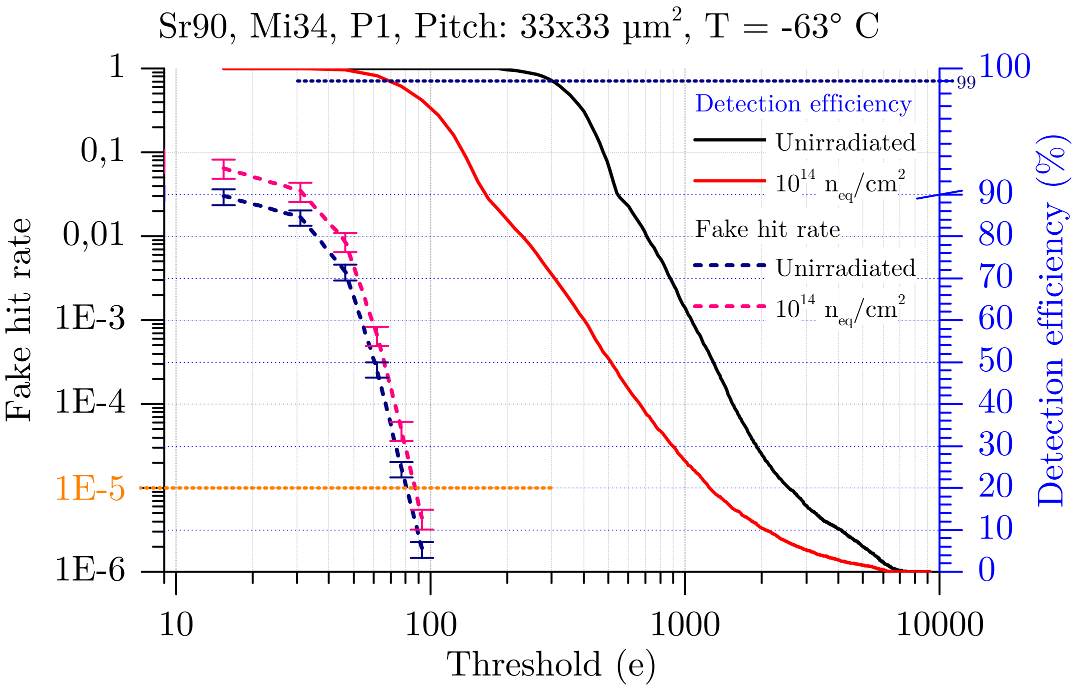

Figure 5.5: Detection efficiency vs. fake hits as a function of noise threshold value for non-irradiated and $10^{14}\,\mathrm{n_{eq}/cm^2}$ irradiated P1 pixels.

5.2.2 $5 \times 10^{13}\,\mathrm{n_{eq}/cm^2}$ dose for the P3 pixel matrix

The largest pixel on the MIMOSA-34 sensor has a size of $33 \times 66\,\mu\mathrm{m}^2$ (see Table 4.1). Size affects the non-ionizing radiation hardness limit because a larger pixel size implies a longer average collection path for the signal charge electrons. A longer collection path increases the chance of recombination with radiation-damage-induced defects in the crystal lattice of the sensing volume. Recombined signal electrons become unavailable in a given time frame.

The results show that the MIMOSA-34 P3 pixel had a maximal non-ionizing radiation hardness limit $\leq 5 \times 10^{13}\,\mathrm{n_{eq}/cm^2}$. The S/N ratio was 22.9, see Figure 5.6. At a higher irradiation dose ($10^{14}\,\mathrm{n_{eq}/cm^2}$), the measured detection efficiency dropped to $(77.5 \pm 0.7)\,\%$ for a threshold of 110 e, and the S/N ratio dropped below 15. Table 5.3 shows the effect of the threshold choice on detection efficiency for a dose of $5 \times 10^{13}\,\mathrm{n_{eq}/cm^2}$. As already seen in Figure 5.5, a compromise must be found between signal sensitivity and noise acceptance.

5.2.3 Summary on the non-ionizing radiation limit

This section illustrated that, in the MIMOSA-34 HR18 sensor cooled to $-63\,^{\circ}\mathrm{C}$, the smaller P1 pixel matrix could withstand non-ionizing radiation doses of up to $10^{14}\,\mathrm{n_{eq}/cm^2}$ and the larger P3 pixels could withstand a dose of $5 \times 10^{13}\,\mathrm{n_{eq}/cm^2}$. The results suggest that MIMOSA-34 sensors have a radiation tolerance about one order of magnitude higher than similar AMS-0.35 µm sensors [Doe15]. Figure 4.1 displays the data for the non-ionizing radiation hardness of MIMOSA-34 sensors (blue band with an uncertainty interval). Increasing the resistivity of the epitaxial layer substantially above $1\,\mathrm{k\Omega\,cm}$ had a positive impact on the non-ionizing radiation tolerance of the sensors.

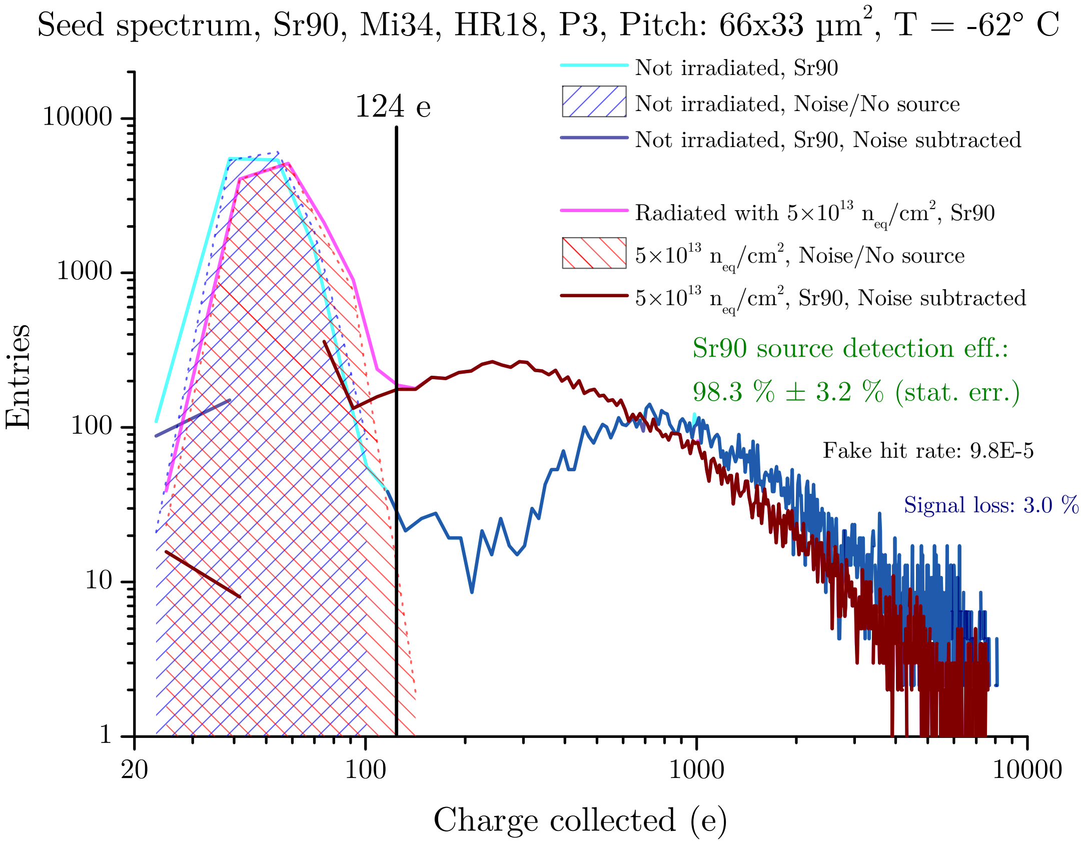

Figure 5.6: As in Figure 5.4, but for the larger P3 pixel matrix and a non-ionizing radiation dose of $5 \times 10^{13}\, \mathrm{n_{eq}/cm^2}$. The threshold is set to 124 e. For other values, see Table 5.3.

Table 5.3: The threshold dependence of the MIMOSA-34 HR18 P3 Sr-90 β-source signal response at a non-ionizing radiation dose of $5 \times 10^{13}\, \mathrm{n_{eq}/cm^2}$. Depending on the chosen threshold value, the total number of detected hits changed. The percentages of undetected hits and fake hits varied. The yellow highlighting indicates the values corresponding to Figure 5.6.

Signal threshold [e]	Sr-90 β-source detection eff. [%]	Signal loss [%]	Fake hits [%]	Fake hit rate per pixel [%]
83	105.3 ± 5.8	0.8	6.5	6.35×10^{-5}
92	101.1 ± 5.6	1.0	2.4	2.34×10^{-5}
108	99.9 ± 5.1	1.8	1.3	1.27×10^{-5}
124	98.3 ± 4.2	3.0	0.1	0.1×10^{-5}
133	98.0 ± 3.6	5.7	0	$<10^{-6}$
141	95.0 ± 2.4	6.4	0	$<10^{-6}$

5.3 Diode size and CPS performance

The S/N study described in the previous section was repeated for other pixel matrices with other diode sizes using sensors manufactured with TowerJazz-0.18 µm technology. The size of the n-doped implementation significantly influenced overall pixel performance. This is reasonable considering the crucial role of n-doped implementation in charge collection. In general, smaller diodes experience less noise but collect charge less efficiently, while larger diodes experience more noise but have more efficient charge collection. An optimal operations-specific compromise should be found.

Systematic measurements of sensor performance using identical pixel pitches and epitaxial layers as a function of diode surface were performed to find this optimum. Measurements with a Sr-90 source were taken to extract the S/N ratio. Unfortunately, it was not possible to vary the diode size completely independently of other pixel parameters. Nevertheless, a trend can be deduced. Figure 5.7a displays a plot of the results, and Table 5.4 provides all of the pixel parameters.

As Table 5.4 shows, the P23, P20 and P17 matrices have the same pixel size. The P27 has a slightly larger pitch but had the smallest diode; the P8 and P19 pixels are significantly larger in pitch. The P19 matrix also has a larger diode footprint to accommodate its large diode. These pixels represent a selection of the most suitable pixels for a diode size study using MIMOSA-34 sensors (see Table 4.1).

Table 5.4: An overview of the matrices used to study the effect of the diode size on the S/N ratio. It was impossible to study diode size in isolation. Therefore, pixels with less suitable parameters were also analyzed to fill the gaps. Less suitable measurements are indicated in gray.

Matrix	$\text{Pitch}_{eff.}$ [µm]	Diode surface [μm^2]	Footprint of diode [μm^2]	S/N
P27	31.1	1	11	59.2
P23	26.9	2	11	92.4
P8	38.1	5	11	80.6
P20	26.9	8	11	95.1
P17	26.9	11	11	67.4
P19	38.1	15	15	54.6

No measurements are available for diode sizes between 2 and 8 μm^2 with comparable pixel matrices. The closest match was the P8 pixel matrix, which was evaluated. It has an unirradiated S/N ratio of 80.6. This is a high S/N value when considering that the P8 pixels has an effective pixel pitch of 38.1 µm, which is nearly twice the size of the P17, P20, and P23 pixels. Other studies (e.g., [Doe+13a]), have found that S/N ratio depends heavily on pixel pitch, as shown in Figure 5.7b. For example, P3 and P1 have the same relationship as P8 and P17; P3 has twice the pixel area of P1 ($\text{Pitch}_{\text{eff.}} = 46.66$ µm vs. 33 µm), and P8 has twice the pixel area of P17 ($\text{Pitch}_{\text{eff.}} = 38.1$ µm vs. 26.94 µm). Other parameters do not differ

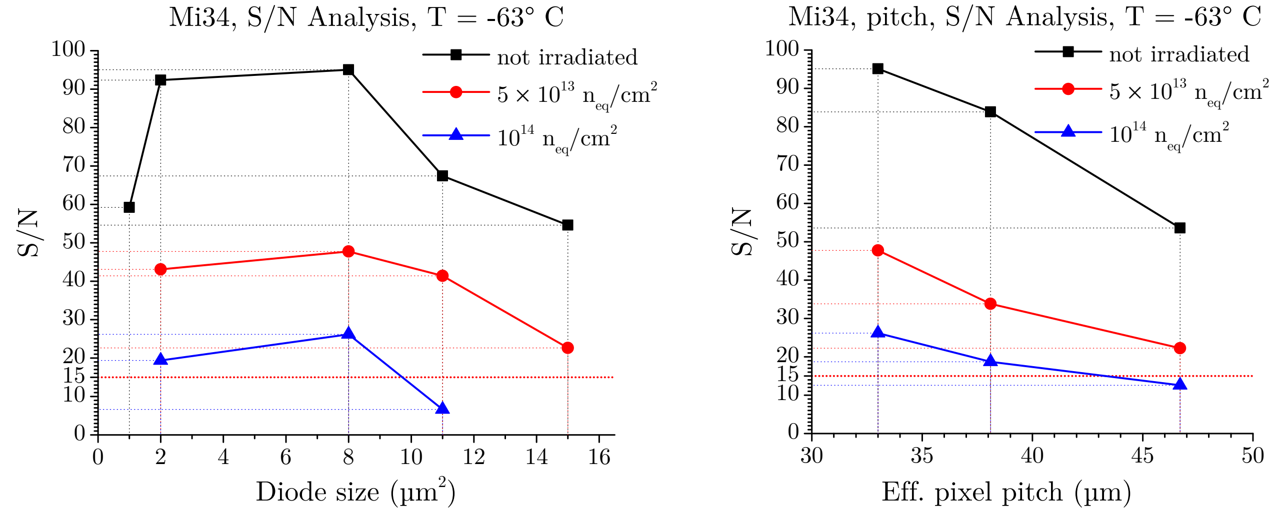

(a) The effect of diode size and induced non-ionizing radiation damage on the S/N ratio of a MIMOSA-34 sensor. The P23, P20, P17, and P19 matrices were used in this study. P23, P20, and P17 only differ in diode sizes, while the P19 pixels (15 µm^2 diode size) are twice the size in the x-direction and have a larger diode footprint. Please refer to Table 4.1 for a full parameter description, as well as Section 5.3 of the text.

(b) S/N ratio depends strongly on pixel pitch; larger pixels have lower the S/N ratios. However, a larger pixel pitch contributes to faster readout speed and less heat dissipation, which is beneficial in a heavy-ion experiment. The P1, P2, and P3 matrices are compared here. A dedicated pitch study can be found in [Doe+13a].

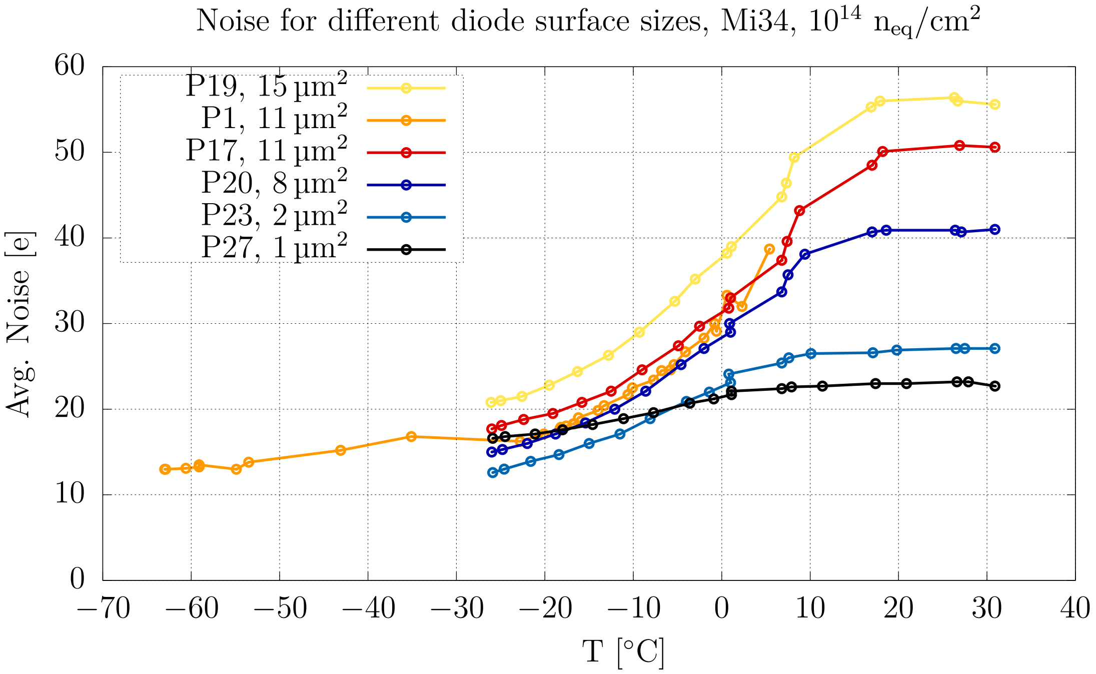

(c) A temperature scan of differing pixel matrices in a MIMOSA-34 sensor. The measured average pixel noise varied with temperature and diode size. Note that diode size and other parameters had to be modulated (see Table 4.1).

Figure 5.7

between these matrices. The S/N ratio of the pixel of the P1 matrix is 95, while the S/N ratio of the P3 matrix is 53.6 (approximately 44 % lower). Given a S/N ratio of 80.6 for the P8 pixel, an estimated S/N ratio ≈ 143 can be calculated for a pixel matrix with an effective pitch of 26.94 µm (the same as P17, P20, and P23) and a diode of 5 μm^2.

The relation between diode size and S/N ratio can also be seen in strongly irradiated chips, see Figure 5.7a. The effects of radiation damage shift the unirradiated curve toward lower S/N values, as expected.

Another study was performed to evaluate the noise of different diode sizes. The average noise of a pixel matrix was measured as a function of the cooling temperature. Six different pixels with varying diode sizes were evaluated. Figure 5.7c displays the average noise of $10^{14}\,n_{eq}/cm^2$ irradiated MIMOSA-34 pixels in relation to temperature and diode size. Note that, due to the design of the pixel matrices, multiple pixel parameters changed simultaneously (see Table 4.1). Therefore, the effect of diode size was not studied in isolation, and leakage current is assumed to be a property of the depleted volume of the diode and the preamplifier. Nevertheless, clear tendencies can be deduced:

1. Higher temperatures cause more noise,
2. Larger diodes have more noise, and
3. The noise of large diodes is mostly influenced by temperature.

The average noise depicted in Figure 5.7c is highly temperature-dependent. From −63 °C to about −20 °C, the noise stays almost constant and rises very gradually. From approximately −20 °C to ≈10 °C, the noise rises exponentially and then saturates at around 20 °C, as can be seen from the other pixel matrices. This behavior can be explained by the thermal excitation of bulk noise and saturation due to charge clearing of the diode. One should note, that the integration time for all MIMOSA-34 measurements in this thesis was 32 µs. As the noise approaches a certain level and the clearing constant matching this integration time, charge clearing (depicted in figure 2.11) begins to dominate the behavior. The noise collected by the pixel is cleared by the forward-biased diode before readout. In SB-Pixels, the diode usually resets the pixel potential between two hits. The more charge a pixel collects, the faster the forward-biased diode resets the pixel potential. At some point, this reset process becomes faster than the constant pixel readout time and charge clearing occurs – the collected charge and noise is cleared before it is collected. This effect leads to the observed noise level saturation in highly irradiated MIMOSA-34 chips at temperatures above 10 °C, as seen in Figure 5.7c. This effect is described in more detail in Section 2.5.1 and [Dev19, chapter 5.1.2].

5.4 Summary

In this chapter, the radiation hardness factors of HR18 and HR20 sensors were estimated. The HR18 sensor outperformed the HR20 sensor. The non-ionizing radiation hardness limit was estimated for P1 and P3 pixel matrices. The non-ionizing radiation hardness limit of an HR18 sensor cooled to $-63\,^{\circ}\mathrm{C}$ was $10^{14}\,\mathrm{n_{eq}/cm^2}$; the P3 matrix had a limit of $5 \times 10^{13}\,\mathrm{n_{eq}/cm^2}$. Therefore, the estimated limits, after including a safety margin, are $5 \times 10^{13}\,\mathrm{n_{eq}/cm^2}$ for the P1 matrix and $10^{13}\,\mathrm{n_{eq}/cm^2}$ for the P3 matrix (See **blue** dots in Figure 4.1). An analysis of the relation between sensor performance and diode size, shows that the optimum diode size was estimated at $(5 \pm 2)\,\mathrm{\mu m^2}$.

Chapter 6

Depletion

> *"Efficiency is doing better*
> *what is already being done."*
>
> Peter Drucker
> Economist and former student of
> the Goethe University Frankfurt

Another strategy to increase the radiation hardness of CMOS MAPS is to increase the region free of charge carriers, which has a very efficient charge collection, called the depleted volume. As discussed in detail in Section 2.3.1, applying a reverse-bias voltage to the collecting diode enlarges the region with no free charge carriers in the sensing volume around the diode. An electrical field forms in this region and guides the generated signal charge to the diode, where the charge can be collected and processed further. This charge collection is much shorter than collection by thermal diffusion. Faster charge collection is beneficial, especially for irradiated sensors, because faster collection times minimize the probability of a signal electron recombining with a defect in the active volume.

Because a larger depletion region is beneficial for signal electron collection, it should be maximized. The volume of the depleted region depends on three parameters:

1. the depletion **voltage** applied,
2. the **dopant concentration** of the p-type epitaxial layer,
3. the **geometry** of the region.

However, the CMOS process restricts the choice of these parameters. For example, as described in Section 4.2.1, only low-resistivity epitaxial layers were initially accessible. Once wafers with high-resistivity epitaxial layers and therefore low dopant concentration were developed, the depleted volume in MAPS increased. These first-generation high-resistivity sensors, produced with the AMS-0.35 µm manufacturing process, could not reach their full radiation hardness potential because there were no pixels with an active depletion option. Eventually, in-pixel discriminators became available and were used for a zero suppression logic and

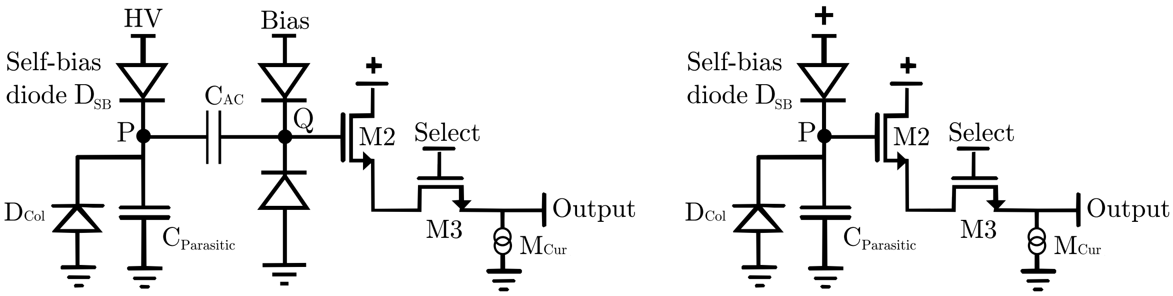

(a) SB-AC

(b) SB

Figure 6.1: Circuit diagram of an AC-coupled SB-Pixel (left) and a standard SB-Pixel (right).

therefore a faster sensor readout. In 2012, it became possible to design sensors with the TowerJazz-0.18 µm [Tow13] manufacturing process. (see [Deg+12]). This novel process allows for high-ohmic epitaxial layers (1 - 5 kΩ cm) [Win11] and has a transistor size of 0.18 µm, much smaller than its predecessors. It also and has other benefits described below.

The smaller, 0.18 µm structure permits a higher integration density and, consequently, more logic on the pixel; it also allows for thinner oxide layers, which improve the ionizing radiation hardness [Doe+13b]. The high-resistivity epitaxial layers, which have doping concentrations up to one order of magnitude below the established standard for AMS-0.35 µm sensors, further increase the depletion depth. Nevertheless, full depletion has not been observed for sensors with depletion voltages <5 V (see the MIMOSA-34 results, f.e. in Figure 6.4). The decoupling and usage of SB-pixels overcome the low voltage restriction of the readout transistors [Bal+08][Sta11] and bias the sensing diode with voltages >10 V, more than the nominal maximum voltage of the process.

An AC[1] coupling capacitor can decouple the low-voltage readout transistors from the collector diode, which ideally operates at higher voltages. Figure 6.1 compares schematics for a standard SB-Pixel and an AC-coupled SB-Pixel. The AC-coupling capacitor is denoted as C_{AC}. The capacitor C_{AC} shields the M2 and M3 transistors from the high-DC biasing voltage. Fluctuations in the potential at point P, which are due to possible signal electrons, are transferred to point Q. Here, the voltage divider consists of two diodes and sets the ground level such that the M2 transistor can register fluctuations in Q. The capacitor C_{AC} acts as a high pass filter; only rapid changes in potential at point P are forwarded to point Q, and the potential offset from the high voltage HV is shielded from the sensitive readout transistors.

6.1 PN junction depletion

The width of the depletion around the collecting diode in the epitaxial layer is one of the major performance parameters for charge collection. Usually, this

---

[1] **A**lternating **C**urrent

thickness is derived by assuming an abrupt PN junction between the n-type doped diode and the p-type doped epitaxial layer. The Poisson equation solution of a one-dimensional photodiode yields a space-charge region width of [Lut07]:

$$d = \sqrt{\frac{2\epsilon_\mathrm{r}\epsilon_0}{e}\left(\frac{1}{n_\mathrm{A}} + \frac{1}{n_\mathrm{D}}\right)(U_\mathrm{bi} - U_\mathrm{depl.})}$$

d	depletion depth
$\epsilon_\mathrm{r}\epsilon_0$	permittivity of Si[a]
e	electron charge
$n_\mathrm{A}, n_\mathrm{D}$	p-type and n-type dopant concentration
U_bi	built-in voltage
$U_\mathrm{depl.}$	externally applied depletion voltage

---

[a] $\epsilon_\mathrm{r}\epsilon_0 = 11.68 \times 8.854\,187 \times 10^{-12}\,\mathrm{F/m}$

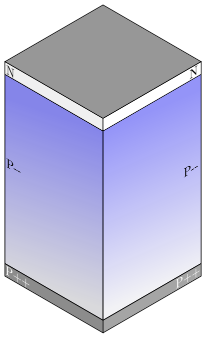

Equation 6.1: An abrupt PN junction is a simple geometry that is not suited to describe the depletion of CMOS MAPS.

According to Equation (6.1), the thickness d of the depleted volume can reach several tens of micrometers. However, this equation is derived for a flat abrupt PN junction and does not accurately approximate the depletion of real pixels of CPS. In typical CMOS MAPS, the n-type region and the p-type region do not resemble a parallel-plate capacitor; they more closely resemble a spherical capacitor. Cross-sections of each of the equally distributed n-type implementations are typically a few square micrometers, while the adjacent p-type region of the active volume is 10-30 µm thick and extends several millimeters or centimeters in the planar direction. The distance between two neighboring n-type implementations is about 20-30 µm². This distance corresponds to the pixel pitch of a sensor. In contrast to Equation (6.1), a three-dimensional solution of the geometry that assumes a single point-like diode model exhibits a mutual sixth-root dependence between the depletion radius R and the depletion voltage U, see Equation (6.2). A detailed

$$R = \sqrt[3]{\frac{3n_\mathrm{D}}{4n_\mathrm{A}} r^3 \left(\sqrt{1 + \frac{8\epsilon_r\epsilon_0}{n_\mathrm{D} r^2 e} \cdot (U_\mathrm{bi} - U_\mathrm{depl.})} - 1\right)}$$

variables as in Equation (6.1) and

R	depletion radius
r	diode radius

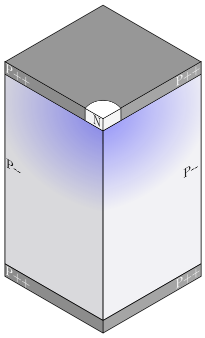

Equation 6.2: A more complex geometry results in a more complex dependence between the depletion volume and the applied voltage. This formula is denoted as "LinRadialFit" for theoretical comparison to experimental results in Figure 6.5. For a deduction see Appendix A.

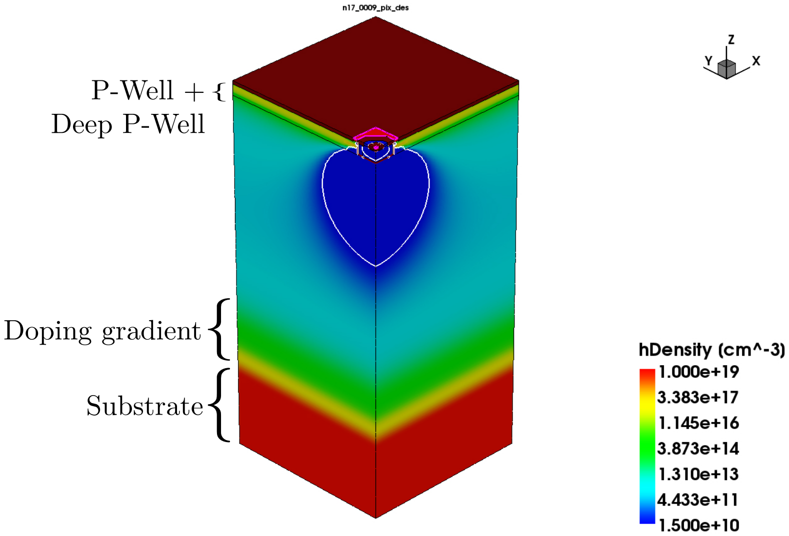

Figure 6.2: A TCAD simulation of hole density in the MIMOSA-34 pixel epitaxial layer with a depletion voltage of $U_{depl.} = 10\,\mathrm{V}$. The maximum hole concentration of the non-depleted substrate was approximately 10^{19}. The simulation was performed, using realistic doping profiles, at the IPHC by [Hey18].

derivation of this equation and an explanation of the measurement technique are attached in Appendix A on page 113. Increasing the depletion voltage U does not greatly increase the depleted volume; which may be misinterpreted as saturation and hereby full sensor depletion.

Equations (6.1) and (6.2) are valid in their respective domains. However, both geometric assumptions are too simplistic to fully describe the depletion behavior in MAPS. The complex geometry of the sensor, realistic doping profiles of the materials used, and the overlapping electrical fields of the individual n-type implementations are neglected in the analytical solutions above. Experimental measurements and detailed numerical simulations were used to determine the size of the depleted region. A realistic 3D TCAD simulation of one of the studied sensors was performed at the IPHC [Hey18] (see Figure 6.2). The results were obtained by utilizing the full MIMOSA-34 pixel schema with all known doping concentrations and simplifying the simulation to a quarter of a single pixel, assuming an axial symmetry in the x- and y-directions. The results of this simulation were compared to experimental measurements (see Figure 6.5, Section 6.3.1).

6.2 Depletion measurements

Fully depleted CMOS MAPS have only recently become available. Since then, tools and observables for measuring the effect of depletion have been developed. This section introduces some of the tools used in such analyses and discusses their validity. The properties studied were the following:

Capacity: The peak positions observed in the charge spectra of CMOS sensors are, among other things, dependent on the capacitance of the pixel, which is dependent on the size of the depleted volume. A change in the size of the depleted volume affects the capacitance of the diode. Changes in the peak positions were observed and deductions were made about the changes in the depleted volume. The observed peaks in the spectra also depend on the gain and CCE.

Charge sharing and cluster size: Depletion has a significant impact on the CCE of a single pixel; it also has a major impact on the average cluster size of a hit. Cluster sizes become smaller as depletion increases. Hit clusters are important for separating real hits from fake hits and can be used to calculate the hit position via the center of mass calculation. Therefore, the average cluster size is an important parameter.

Volume estimates: The sensors were illuminated with an Fe-55 source. The number of hits with 100 % CCE in the seed spectra was counted and compared to the total number of recorded hits (found by integrating the sum spectra). From this information, the size of the depleted volume could be estimated. If depletion increases, the single-pixel CCE and therefore the number of wholly collected hits also increases.

Leakage current: [Lin03] shows that the bulk leakage current of differently doped silicon is proportional to the amount of non-ionizing radiation received and the size of the depleted volume. Conversely, for a known radiation dose and leakage current, the depleted volume can be estimated. [Bus19] conducted a dedicated study regarding the effects of depletion on the leakage current of MIMOSA sensors.

Depth scans with Sr-90: The Sr-90 β source allows a scan of the epitaxial layer of a CMOS sensor along its depth. Since the sensors under study deplete the pixel from the side on which the diode resides, depletion is not evenly distributed over the full sensor depth. The Sr-90 β-source provides some insight into how β-rays create signal electrons along their trajectory in silicon.

Capacity

Various studies have measured depletion using C-U (capacitance-applied voltage) curves. The capacitance of the depleting diode shrinks as the depletion progresses. At a certain point, the maximum depletion is reached, and no further decrease in capacitance is observed. This can be interpreted as an indicator of full depletion. However, as discussed in Section 6.1, a less steep capacitance curve may also indicate a more gradual increase of the depleted volume without achieving full depletion, especially when using a smaller diode (see Equation (6.2)).

For this thesis, the capacitance of the depleting diode could not be measured directly because the gain factor of the readout chain g was not known (see Equation (2.1)). Nevertheless, the position of the calibration peak $U_{\text{cal.}}$, which depends on the capacitance C, the collected charge Q, and an amplification factor g, was accessible.

$$C = \frac{Q \cdot g}{U_{\text{cal.}}} \tag{6.3}$$

If the internal amplification factor g and the collected charge are constant, an increase in capacitance C causes a shift of the calibration peak position $U_{\text{cal.}}$ toward lower values. A reduction in this shift indicates a saturation of the capacitance C and an increase in depletion voltage. This assumption is valid if the collected charge Q is the overall charge created by a single photon. Therefore, only photons that converted directly in the depleted area of the diode were used for calibration and (indirect) capacitance measurements. To calibrate the measurements, the sensing diode was assumed to collect all of the generated electrons – for example, 1640 electrons when a K_α Fe-55 photon converts into silicon. This method was used to analyze the depleted area of MIMOSA-34 and Pipper-2 sensors.

One drawback of this method is that the effects of depletion are only measured indirectly. Furthermore, systematic uncertainties occur while measuring the calibration peak position and by assuming a constant amplification factor g. Moreover, a saturation of the resulting *C-U* curve does not necessarily signify full depletion. Even partially depleted sensors may indicate saturation due to rapid flattening of the *C-U* curve. There is a theoretical discussion of this topic in Section 6.1 and Figure A.3a. Moreover, an absolute value for the depleted volume cannot be obtained.

For planar PN transitions, the reciprocal of the capacity depends linearly on the depletion depth d [Lut07]:

$$\frac{1}{C} = \frac{d}{\epsilon\epsilon_0} \tag{6.4}$$

Combining equation (6.1) and the capacitance of an abrupt PN junction produces:

$$\frac{1}{C} \propto \sqrt{U_{\text{depl.}}}$$

Since the depleted zones of MAPS have complex geometry, the PN transition is not planar. For this reason, the special case discussed above does not apply; the relationship will be different than expected. For example, inserting a spherical geometry into Equation (6.2) indicates a sixth-root dependence.

Volume estimates

To measure the depleted volume, the pixels in the MIMOSA-34 sensor were illuminated with an Fe-55 K_α γ-source. On average, these 5.9 keV X-rays create 1640 electron-hole pairs in silicon sphere with a diameter ≈1 µm. If conversion occurs in the depleted volume $V_{\text{depl.}}$ of the diode, all of the generated signal electrons are collected by an individual pixel diode. If charge generation occurs elsewhere, the signal charge diffuses and is collected by several pixel diodes in a pixel cluster. The number of hits collected in the depleted volume $N_{\text{depl.}}$ can be distinguished from the total number of hits N_{all} by the seed spectra (see Section 2.5.2). A uniform illumination of the constant full pixel volume V_{pixel} was assumed. Therefore, the size of the depleted volume $V_{\text{depl.}}$ should scale with the number of registered hits in that area. The fraction of volume that had a CCE of 100 % was calculated, and the total depleted volume was found by assuming the pixel volume V_{pixel} was fixed by its known pixel pitch $x_{\text{eff. pitch}}$ and the epitaxial layer thickness h_{epi}:

$$V_{\text{depl.}} = \frac{N_{\text{depl.}}}{N_{\text{all}}} \cdot V_{\text{pixel}} = \frac{N_{\text{depl.}}}{N_{\text{all}}} \cdot h_{\text{epi}} \cdot x^2_{\text{eff. pitch}} \tag{6.5}$$

6.2.1 Observed effects of depletion on sensor performance

Depletion has a significant impact on major sensor performance characteristics. In general, an initial increase in depletion voltage causes the following changes:

- increased gain (shift of most probable value in non-calibrated spectra),
- increased CCE_1,
- more entries in the calibration peaks,
- decreased, but still non-negligible charge sharing.

These effects will be discussed using the experimental results. The first measurements carried out at the IKF on sensors with AC-coupled readout chains were taken using the P13 pixel matrix in a MIMOSA-34 sensor. This sensor features many other pixel matrices that do not host AC-coupled diodes but that share the same epitaxial layer (see Table 4.1); it is very well suited to study the effects of depletion on standard observables. These early depletion studies are presented in Section 6.3.

A sensor dedicated entirely to studying the effects of depletion and the resulting radiation hardness was introduced in 2014 and named Pegasus [KD14]. The findings on these sensors are reported in Section 6.4. The successor and most recently developed sensor studied in this thesis is the Pipper-2 sensor [Kac+16]. Results for the Pipper-2 are discussed in Section 6.5.

6.3 Depletion studies with MIMOSA-34

The P13 pixel matrix used have a pixel pitch of 33×33 µm^2, a diode size and footprint of 11 µm^2, and an AC-coupled readout. Figure 6.1b provides a schematic of the pixel. It can be actively depleted with up to about 9 V. An intrinsic built-in voltage of 0.6 V was anticipated and added to the values shown in this thesis. To exclude any external voltage fluctuations and ensure a steady voltage, batteries connected in series were used to deplete the sensor.

The sensors were operated at room temperature in a dark chamber to minimize external influences. The signal response spectrum was recorded as described in Section 2.5.2. Depleted volume hits were isolated by identifying instances in which the central pixel of a cluster showed a significant signal charge ($Q_{\text{signal}} \geq 5 \cdot Q_{\text{noise}}$) but each neighboring pixels did not ($Q_{\text{neighbor}} < 5 \cdot Q_{\text{noise}}$). For a visualization of this "veto spectrum" technique, please see Figure 2.12a and Section 2.5.2 on page 34.

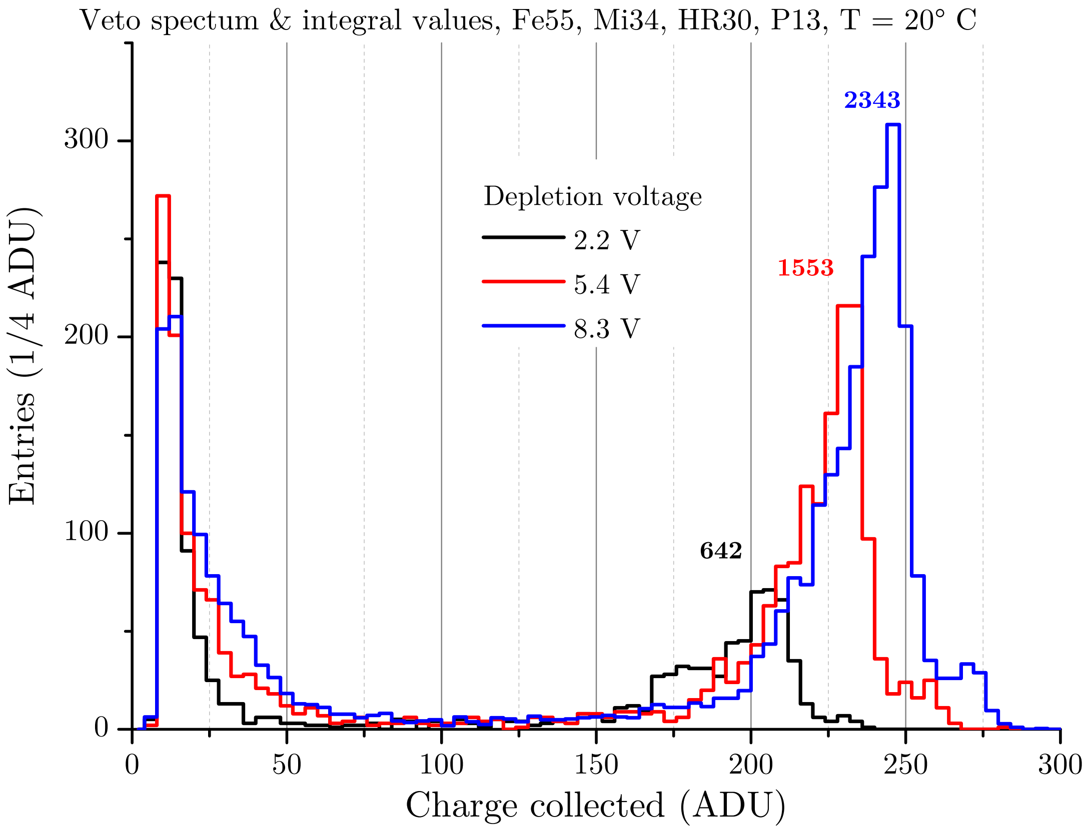

Figure 6.3: The veto spectrum of a MIMOSA-34 prototype sensor. The numbers over the peaks show the integral values without noise, these values were obtained using the technique described in Section 2.5.2.

Figure 6.3 shows the related amplitude "veto" spectrum for increasing depletion voltages. The peak created by the hits in the depleted volume is located between 200-250 ADU. Its position shifted toward higher values for higher depletion voltages. Figure 6.4b shows the sum spectrum that contains all hits and displays the accumulated collected charge per hit of a 5×5-pixel cluster. The sum spectra also show peaks between 200 and 250 ADU, which indicates that the summed charge collected by diffusion from the active pixel volume of a cluster had a CCE_{25} value close to 100 %. The small number of hits with a collected charge amplitude between 30 and 150 ADU is associated with hits that occurred close to but outside of the active volume, such as in the substrate. In this case, only a fraction of the

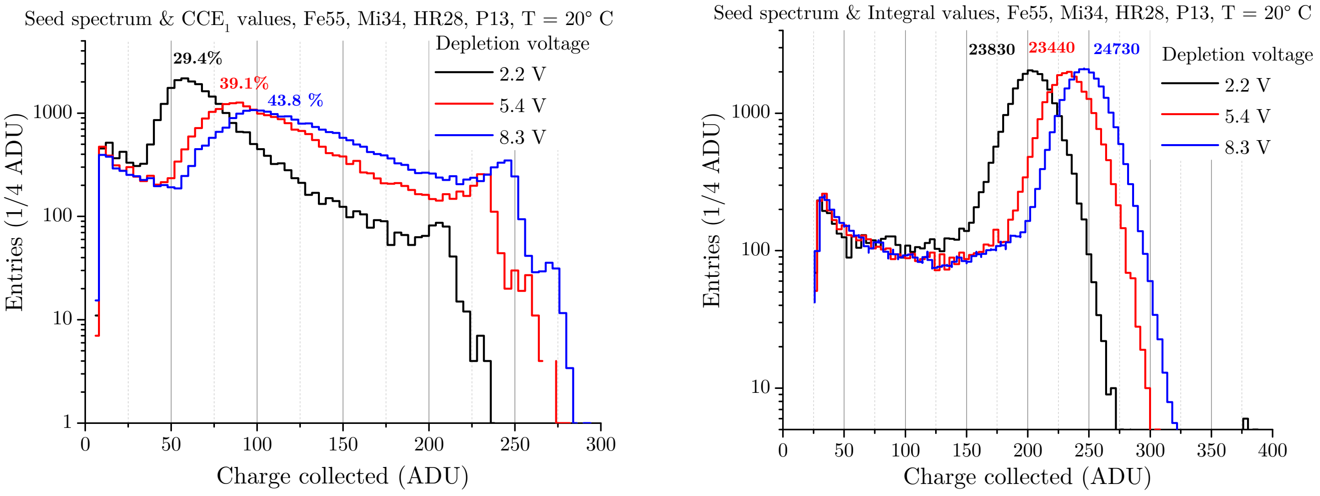

(a) Signal response spectra for different depletion voltages for one pixel. As depletion voltage increased, the gain also increased, and the calibration peak became more pronounced, while the signal for hits in the area with less than 100 % charge collection became smaller. CCE is given in percent.

(b) The summed signal of a 5×5 cluster around the most significant pixel. The numbers above the peaks represent the integral values. Those values are approximately constant, which implies a 5×5 cluster collects all charges independently of the applied depletion voltage.

Figure 6.4: Depletion studies with a MIMOSA-34 sensor.

deposited charge diffused into the active volume and was available for collection. Those hits are ignored in the following analysis.

The number of hits $N_{\text{depl.}}$ and N_{all} were measured by integrating the peaks in the veto and sum spectra. The uncertainty of the lower integration limit of the peaks was accounted for and estimated. The number of hits in the depleted region $N_{\text{depl.}}$ increased with voltage. This reflects the increase of the depleted volume with voltage. In contrast, N_{all} is constant for different depletion voltages. This value is the sum of the hits that occurred in both the depleted and non-depleted areas of the active volume. The total sensitive volume remains constant, even if the depleted area is increasing. This method also demonstrates that the sensor reliably detected hits over the whole sensitive volume, even if no additional drift fields are present.

The total pixel volume V_{pixel} was given by the MIMOSA-34 HR28 pixel design ($V_{\text{pixel}} = 28\,\mu\text{m} \times 33\,\mu\text{m} \times 28\,\mu\text{m}$). The attenuation of X-rays in silicon of this thickness is not negligible, so a calculated correction factor was applied to N_{all}.

The X-ray source was placed at a vertical angle above the sensors, so a homogeneous distribution of photons in the x-y-plane can be assumed. However, the intensity of the X-rays decreased exponentially with penetration depth. Therefore, a homogeneous illumination of the sample can only be assumed in the x-y plane. An attenuation factor was calculated.

Photon mass attenuation coefficients are given in [HS95]. This coefficient characterizes how easily a material can be penetrated. It is defined as $^{\mu}/_{\rho}$, where μ is the attenuation coefficient usually in SI units of $1/m$ and ρ is the density in units of kg/m^3. The probability that a photon survives after traversing a distance l can be expressed as

$$I/I_0 = \exp\left(-\mu \cdot l\right)$$

with l being the length over which the attenuation takes place. μ has a value of $342.51\,\mathrm{cm}^{-1}$ for silicon and a photon energy of 5.9 keV. The photon flux at the penetration depth l is therefore:

$$I(l) = I_0 \exp\left(-342.51\,\mathrm{cm}^{-1} \cdot l\right) \tag{6.6}$$

By integrating Equation (6.6) over the thickness of the sensor, the effective attenuation over the full sensor thickness can be calculated.

$$\int_{0\,\mu\mathrm{m}}^{28\,\mu\mathrm{m}} 100\,\% \cdot \exp\left(-\mu \cdot l\right) \mathrm{d}l = 100\,\% \cdot \left[-\frac{1}{\mu}\exp\left(-\mu \cdot l\right)\right]_{0\,\mu\mathrm{m}}^{28\,\mu\mathrm{m}} \approx 18.006\,\% \cdot \mu\mathrm{m}$$

Now we calculate the correction factor for the HR28 MIMOSA-34 sensor through division by the sensor thickness:

$$\frac{18.006\,\% \cdot \mu\mathrm{m}}{28\,\mu\mathrm{m}} \approx 64.31\,\%$$

Therefore, the average attenuation of K_α photons for a sensor of this thickness is ≈35.69 %, and N_{all} was divided by 64.31 % to account for the attenuation. The depleted zone is expected to be shallow relative to the overall sensing volume, and its geometry is unknown. As such, the correction is not applied for $N_{\mathrm{depl.}}$. The depleted volume $V_{\mathrm{depl.}}$ has some systematic uncertainty due to this. The depletion depth r_{d} is calculated by assuming a hemispheric depleted region and by using

$$r_{\mathrm{d}} \approx \sqrt[3]{\frac{3}{2\pi} V_{\mathrm{depl.}}} \tag{6.7}$$

The depletion depth r_d was then compared to theoretical predictions, which assumed both a flat abrupt PN junction (see Equation (6.1)) and a more realistic diode geometry (see Equation (6.2)). Figure 6.5 displays the results. The realistic models on the depleted volume agreed with the experimental results. A slight mismatch between the TCAD simulations and the measurement was observed for depletion voltages above 6 V. In addition to the more complex theoretical formula derived in Chapter A, a more straightforward “rule of thumb” empirical fit was presented. The empirical fit suggested an abscissa-shift of $(0.7500 \pm 0.0043)\,\mathrm{V}$ and an increase in the depletion depth $\propto \sqrt[m]{U_{\mathrm{depl.}}}$, where $m = 3.850 \pm 0.058$.

Capacity

The relation between capacity and applied depletion voltage was also estimated. The pixel diode capacity could be estimated because the charge collected by the diode in a MIMOSA-34 sensor is stored in its capacity. The related voltage drop $U_{\text{signal}} = Q_{\text{signal}}/C$ is amplified. Therefore, the abscissa-positions of the peaks in Figure 6.4a increased as capacity decreased, which provides a measure of the capacity. In an abrupt PN junction, the capacity is expected to drop quickly and steeply as the depletion voltage increases. After an increase in the depletion voltage of a few volts, the capacity should remain mostly constant as the full pixel volume becomes depleted. According to the model in Equation (6.2), a smaller diode should experience a slow 10 % decrease in capacity, which should generate a proportional increase in the peak position in Figure 6.5a. Indeed, the abscissa-position of the peaks increased by roughly 12 %, which is consistent with the small diode predictions.

6.3.1 Comparison to TCAD simulations

The theoretical and measured results were also compared to TCAD simulations [Hey18]. The TCAD simulation setup was varied to understand the interaction between pixel design and the depletion mechanics. To do so, a 3D-model of a quarter of a pixel was simulated. The layout of the n-well creating the diode and the pixel dimension were chosen to match the MIMOSA-34 P13 pixel geometry. A realistic doping profile (as provided by the CMOS manufacturer) was used for the epitaxial layer simulation.

Figure 6.5 presents two different TCAD simulations. For the realistic simulation, the fully detailed pixel layout was used. This realistic model did not indicate full depletion and matched the empirical observations within the margin of error.

A simplified TCAD simulation was conducted using an epitaxial layer with a constant p-doping of $3 \times 10^{11}\,\text{cm}^{-3}$; there was no p-well on top of the pixel and no substrate material. The simulation indicated full depletion of the pixel after a few volts were applied to the potential of the n-well [Hey18]; this is not shown in Figure 6.5. Thus, the results contradict the empirical findings. Most likely, the model oversimplified the problem. A similar result was obtained once a 10 nm thick grounding structure was placed on the top around the n-well of the diode.

To understand the discrepancy between the realistic model and the other simulations, another simplified setup was evaluated. A thicker 1 µm P++ layer was added to the top and bottom of a constantly doped active layer. The top layer was grounded, and the bottom layer was left floating. However, the bottom layer mostly remained at ground, as the leakage current was predominantly delivered from the top of the P++ layer located near the n-well implantation. This model used a more realistic P++ layer thickness of 1 µm. The results indicated a depletion depth that mostly matched the values obtained from the realistic simulation and the empirical measurements (see Figure 6.5, P++ 1 µm). Because the naive approach used a 28 µm epitaxial layer with a constant doping concentration of $3 \times 10^{11}\,\text{cm}^{-3}$ and matched the simulation with the realistic doping gradient, the exact doping profile is not crucial for depletion simulations of MIMOSA-34 sensors.

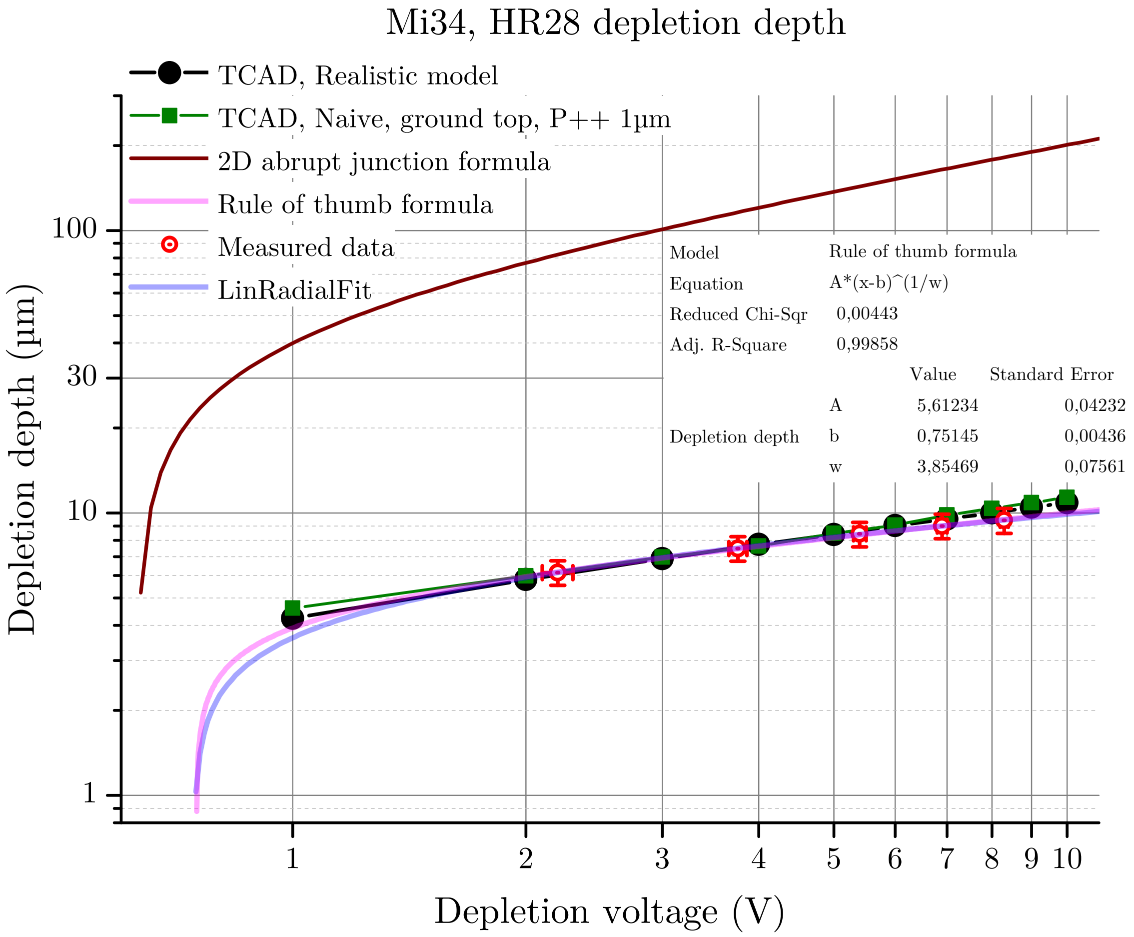

Figure 6.5: A comparison of the experimentally obtained depletion depth using Equation (6.7) (red circles with error bars), the TCAD simulation (black and green line) [Hey18], and the theoretical prediction based on the analytical Equation (6.2) (blue line). The fit parameters and the equation for a simplified root "rule of thumb" formula (pink line) are shown in the box.

However, it is essential to include the p-well, the grounding, and the surrounding substrate.

6.3.2 Conclusion

The epitaxial layers of CPS are usually thin to maximize the S/N ratio. As such, a low-noise pre-amplifier is needed. To attain this, the pixel capacity is generally reduced by minimizing the size of the n-well implantation of the collecting diode. The results show that this small implantation generated a depleted volume that behaved approximately like a hemispherical geometry. The "rule of thumb" empirical fit suggests an abscissa-shift of $(0.7500 \pm 0.0043)\,\mathrm{V}$ and a hemisphere radius $r_\mathrm{d} \propto \sqrt[m]{U_\mathrm{depl.}}$, where $m = 3.850 \pm 0.058$.

The more complex analysis "LinRadialFit", derived in Appendix A, suggests $r_\mathrm{d} \propto \sqrt[m]{U_\mathrm{depl.}}$, where $m = 6$. The fit assumes a simplified geometry of a MAPS pixel cell, as shown in equation (6.2). The diode has the shape of a small cylinder

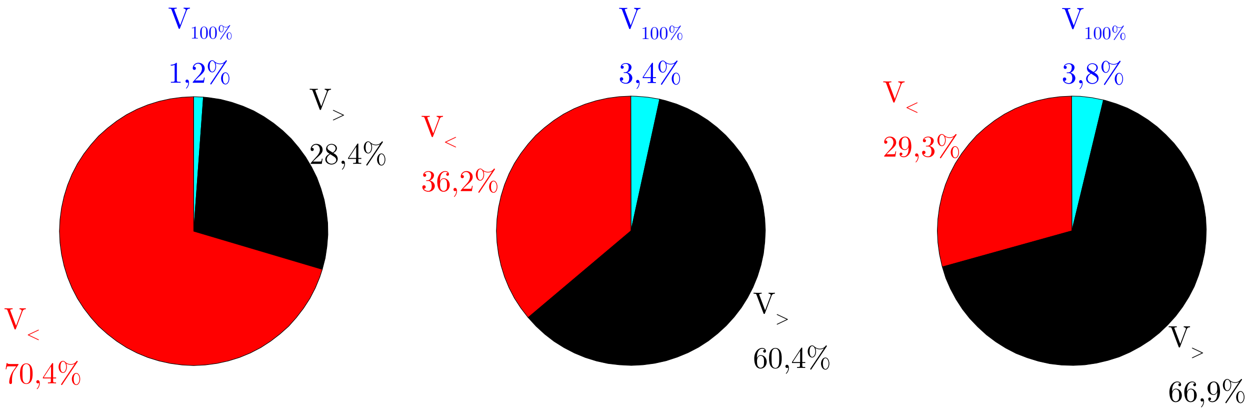

(a) 2.2 V (b) 5.4 V (c) 8.3 V

Figure 6.6: Zone shares of the total active volume for different depletion voltages of the HR28 MIMOSA-34 P3 pixel matrix ($\text{pitch}_{eff.} = 33\,\mu\text{m}$). Zone shares were calculated using data from Figure 6.4a.

and is highly n-doped. The capacity of the diode toward possible structures above the top SiO_2 layer (e.g., metal layers) is neglected. Electrical fields radiated from the n-well implementation toward the adjacent highly p-doped p-wells are also neglected. Table A.1 provides the values used in the model for the doping concentrations, the diode sizes, and the pixel shapes; these values were taken from the technical specifications [IPH18] when possible.

The impact of a depletion voltage on the depleted volume of a MIMOSA-34 sensor was substantially smaller than anticipated for an abrupt PN junction where the volume scales with $r_{\text{d}} \propto \sqrt[2]{U_{\text{depl.}}}$. Moreover, for an n-doped implantation that is sufficiently small compared to the overall epitaxial layer depth, the capacity and the depletion depth appeared to saturate long before the pixel was fully depleted in the MIMOSA-34 sensor.

6.3.3 Further MIMOSA-34 results

Figure 6.4 shows the analog signal response of the MIMOSA-34 P13 pixel matrix with a 28 µm epitaxial layer to an Fe-55 γ-source as a function of the applied depletion voltage $U_{\text{depl.}}$. As expected, a higher depletion voltage improved charge collection. An analysis similar to the one for the zone share study in Section 4.2.1 (Figure 4.4) was applied to the MIMOSA-34 sensor from this chapter in order to compare the two studies. Figure 6.6 shows the zones shares of the total active volume for the HR28 sensor at different depletion voltages. As anticipated, the $V_<$ share decreased, while the $V_>$ share increased with a higher depletion voltage. Note that the AC-coupled P13 pixel matrix had a pixel pitch of $33 \times 33\,\mu\text{m}^2$, while the P17 pixel studied in Figure 4.4 had a slightly smaller pixel pitch of $33 \times 22\,\mu\text{m}^2$. The surface and footprint of the diodes were identical.

6.4 Pegasus sensor

Pegasus sensors are manufactured with the TowerJazz-0.18 µm manufacturing process. Its epitaxial layer has a resistivity above 1 kΩ cm and is 18 µm or 28 µm thick. The collecting diode is AC coupled to the amplifier, like the P13 pixel of the MIMOSA 34 sensor mentioned previously. The pixel size is $25{\times}25\,\mu\text{m}^2$. A matrix has 32 columns and 56 rows [Kac+16].

Moreover, the Pegasus sensor is designed to work with depletion voltages above 10 V. This is made possible by decoupling the readout circuit from the sensor circuit with the sensing diode via a complex AC-coupled capacitance. Figure 6.7a displays an exemplary Pegasus spectrum. The sensor was optimized for depletion, and the diode was enlarged. The trend for the AC-coupled P13 pixel in the MIMOSA-34 sensor (presented in Figure 6.4a and described in Section 6.3.3) continued. The calibration peak became more pronounced, while the CCE peak mostly vanished. In Figure 6.4a, the area from 30-150 ADU has the most entries. Taken together, these findings imply that the charge is shared between neighboring pixels for most hits; the MIMOSA-34 sensor collects its charge mostly by diffusion. In contrast, the Pegasus sensor had a much more pronounced 100 % CCE calibration peak, as seen in Figure 6.7a, which signifies that the Pegasus sensor collects charge mostly with a single pixel. Such behavior is expected if an electrical field within the depleted area guides the charge to the collecting diode. Figure 6.7b shows sum spectra for a 5×5 pixel cluster. Unlike in the MIMOSA-34 sensor, the Pegasus pixel cluster did not collect more charges on average than the single pixel. As a result, the spectrum lost some quality, and the spectral peaks became broader and less pronounced.

The seed and sum spectrum peaks in Figure 6.7a and 6.7b are both at 160 ADU. The volume of the Pegasus sensor was calculated with the same method used for the MIMOSA-34 sensor. The veto peak integral was determined, with correction for attenuation, and then divided by the sum peak integral. This resulted in a $\frac{N_\text{depl.}}{N_\text{all}}$ value $\approx (101 \pm 2)\,\%$. This value was placed into Equation (6.5), which results in a fully depleted volume $V_\text{depl.} = \frac{N_\text{depl.}}{N_\text{all}} \cdot V_\text{pixel} = 101\,\% \cdot V_\text{pixel}$. Substituting this value into Equation (6.7) produced a depletion depth r_d of 17.6 µm. The specified epitaxial layer was 18 µm, so Equation (6.7) indicates that the depleted depth was ≈97.7 % of the full depth. The results demonstrate that the sensor was fully depleted.

As the chip was irradiated with $10^{14}\,\text{n}_\text{eq}/\text{cm}^2$, the 100 % CCE calibration peak became displaced and wider (see Figure 6.7a). While the non-irradiated sensor collected 100 % of the charge with a single pixel, the irradiated sensor had a lower amplitude, producing a broader peak. Furthermore, the irradiated chip was not depleted as well as the non-irradiated. This was first observed with Pegasus sensors and was further investigated with Pipper-2 chips.

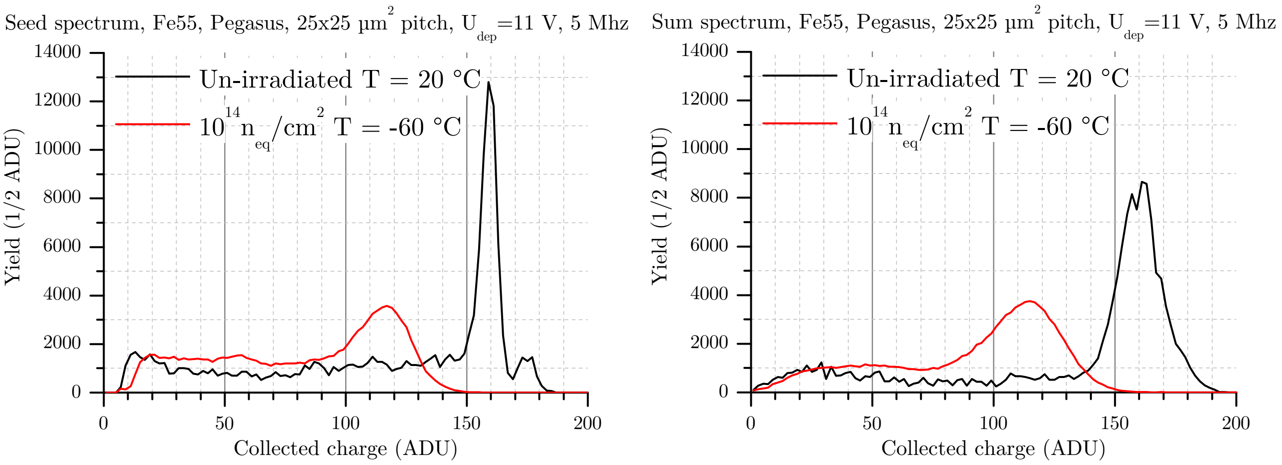

(a) Seed pixel signal response spectrum.

(b) The summed signal of a 5x5 cluster around the most significant pixel.

Figure 6.7: Raw Fe-55 spectra of an unirradiated and irradiated Pegasus sensor are shown. The sensor is depleted with $U_{\mathrm{depl.}} = 11\,\mathrm{V}$.

6.5 Pipper-2 sensor

The Pipper-2 sensor prototype is designed to study the effects of depletion in detail. The Pipper-2 pixel studied here were $22{\times}22\,\mu\mathrm{m}^2$ in size, were manufactured with the TowerJazz-0.18 µm process, and had a p-type epitaxial layer with a thickness of 18 µm. The sensor had four independent sub-matrices, each with $8{\times}128$ pixels. The matrices were read out using a rolling-shutter mode by an independently connected output. In this thesis, only the first matrix, which had a round n-well collecting diode with a diameter of 5 µm, was studied. This diode was AC-coupled to a source follower transistor using a 21 fF capacitor [Hey18, p. 65]. The capacitor was optimized to withstand voltage > 20 V.

The Pipper-2 sensor was depleted with up to 20 V to study changes in the signal response to Fe-55 γ-particles (Figure 6.8). The capacitance C decreased, the CCE increased, and the charge collection peak disappeared as depletion voltage increased; this was observed in the MIMOSA-34 P13 pixel studies with lower voltage (Section 6.3.3). Please note that the reference sensor was irradiated with $10^{13}\,\mathrm{n_{eq}/cm^2}$ since no completely unirradiated sensor was available for this study. However, sensor tolerance to bulk damage was found to be high enough that this weakly irradiated sensor was used, with caution, as a reference in the following.

6.5.1 Charge clearing

Figure 6.9 depicts sensor performance after a non-ionizing radiation dose of $5\times10^{14}\,\mathrm{n_{eq}/cm^2}$. The calibration peaks widened and shifted to lower abscissa-axis values. This change may be explained by the effects of charge clearing introduced in Equation (2.3). To calculate the time constant τ in the charge clearing Equation (2.3), $Q_{\mathrm{S}} = Q_{\mathrm{Phys}} \cdot \exp\{(-t/\tau)\}$, the leakage current of the sensor was mea-

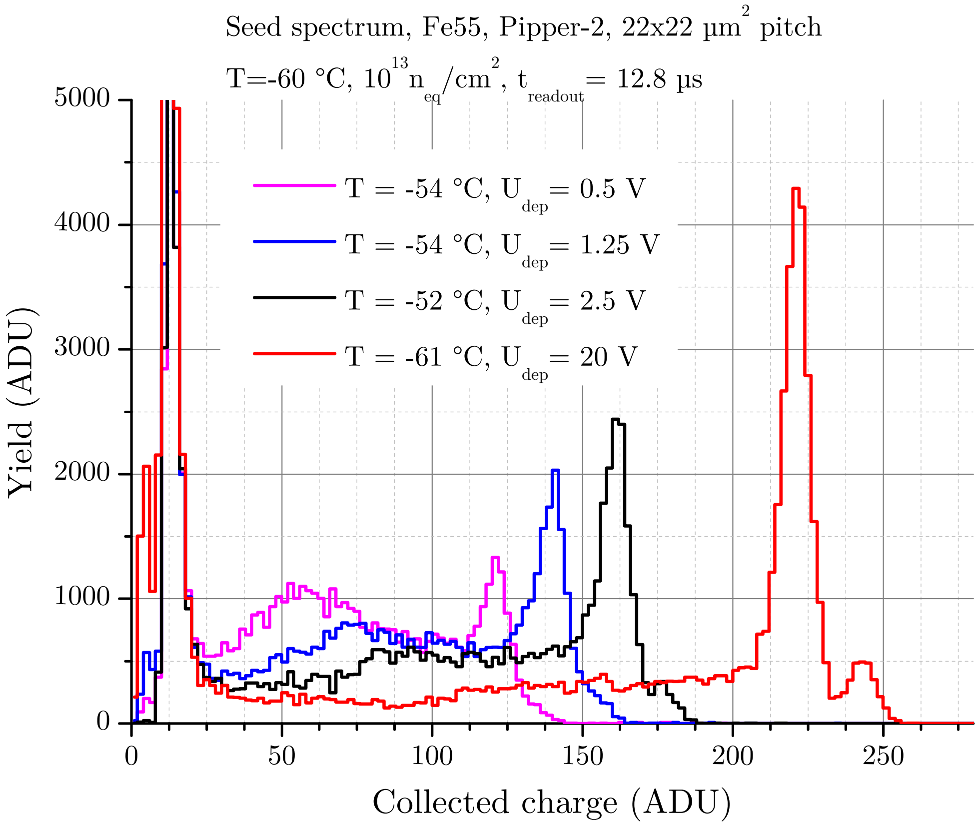

Figure 6.8: The Fe-55 spectra of a Pipper-2 sensor with respect to the applied depletion voltage. The sensor is designed for depletion voltages above 10 V.

sured in relation to radiation dose and temperature. Figure 6.10 demonstrates that leakage current increases as depletion voltage and temperature increase. A Pipper-2 sensor irradiated with $5 \times 10^{14}\,\mathrm{n_{eq}/cm^2}$ at a temperature of $-5\,°\mathrm{C}$ and a depletion voltage of 20 V had a leakage current $I_{\text{leak tot.}} \approx 0.058\,\mu\mathrm{A}$. The leakage current was measured for the whole sensor, which had 6144 diodes [Bus19]. Therefore, the leakage current per diode was assumed to be $I_{\text{leak}} = 0.058\,\mu\mathrm{A}/6144 \approx 9.44\,\mathrm{pA}$. Then, τ can be calculated using the values provided in [Hey18, p. 65] and inserting them into [Dev19, p. 32]:

$$\tau \approx \frac{k_B T C}{e} \frac{1}{I_{\text{leak}}} = \frac{8.617 \times 10^{-5}\,\mathrm{eV/K} \cdot 268\,\mathrm{K} \cdot 21\,\mathrm{fF}}{e \cdot 9.44\,\mathrm{pA}} \approx 51.4\,\mu\mathrm{s} \quad .$$

The calculated τ value was approximately $51.4\,\mu\mathrm{s}$, which was the same order of magnitude as the sensor rolling-shutter readout speed ($t_{\text{r.o.}} = 12.8\,\mu\mathrm{s}$). As a result, rapid charge collection and extensive cooling are necessary to reduce the effects of charge clearing; the Pipper-2 sensors studied here were cooled to up to $-60\,°\mathrm{C}$ to reduce the leakage current as much as possible.

6.5.2 Capacity

The x-positions of the calibration peaks in Figures 6.8 and 6.9 can be used to estimate the capacity of the pixel in arbitrary units. Pixel capacity decreases

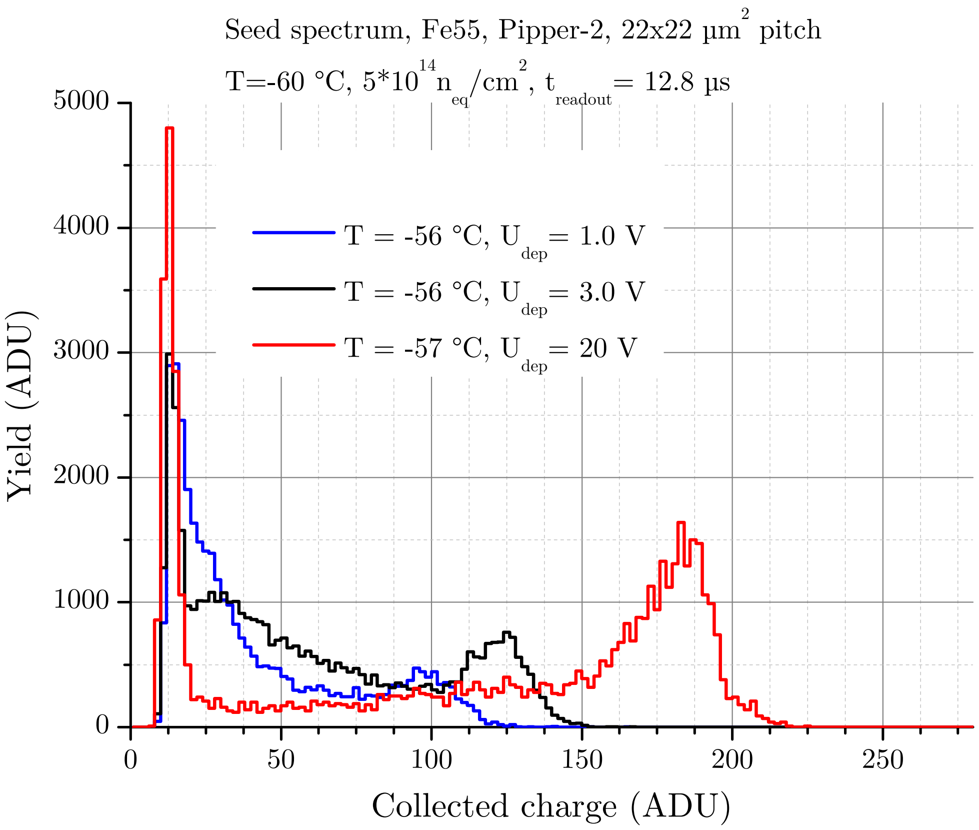

Figure 6.9: The raw signal spectra of a $5 \times 10^{14}\,\mathrm{n_{eq}/cm^2}$ irradiated Pipper-2 sensor. Compared to the unirradiated spectra (Figure 6.8), the CCE shifted to lower values for the depletion voltages studied.

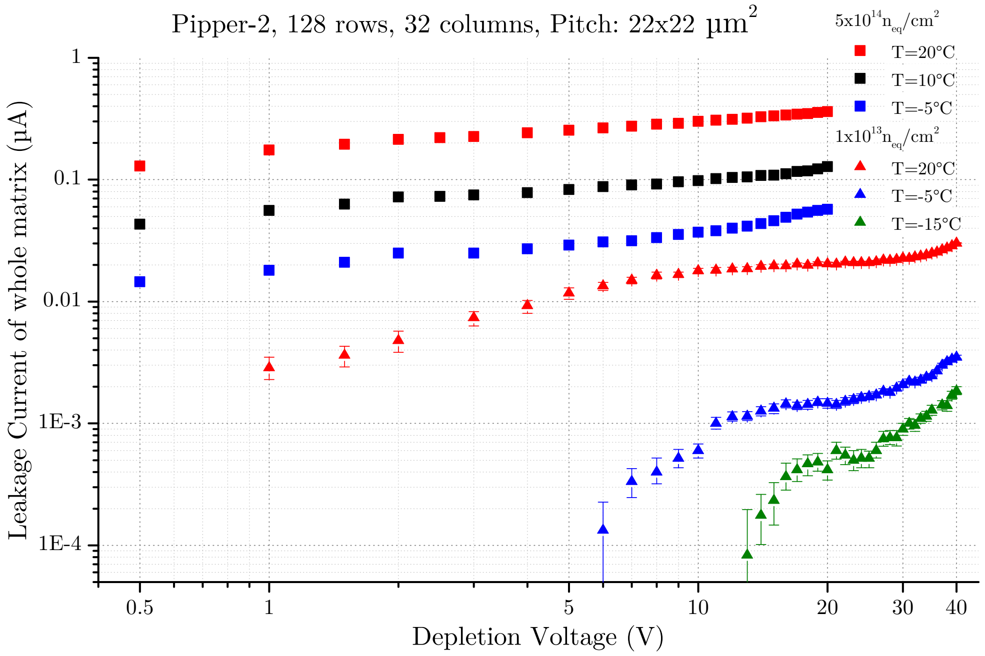

Figure 6.10: The measured leakage current of a whole pixel matrix in a Pipper-2 sensor in relation to the applied depletion voltage, temperature, and non-ionizing radiation dose.

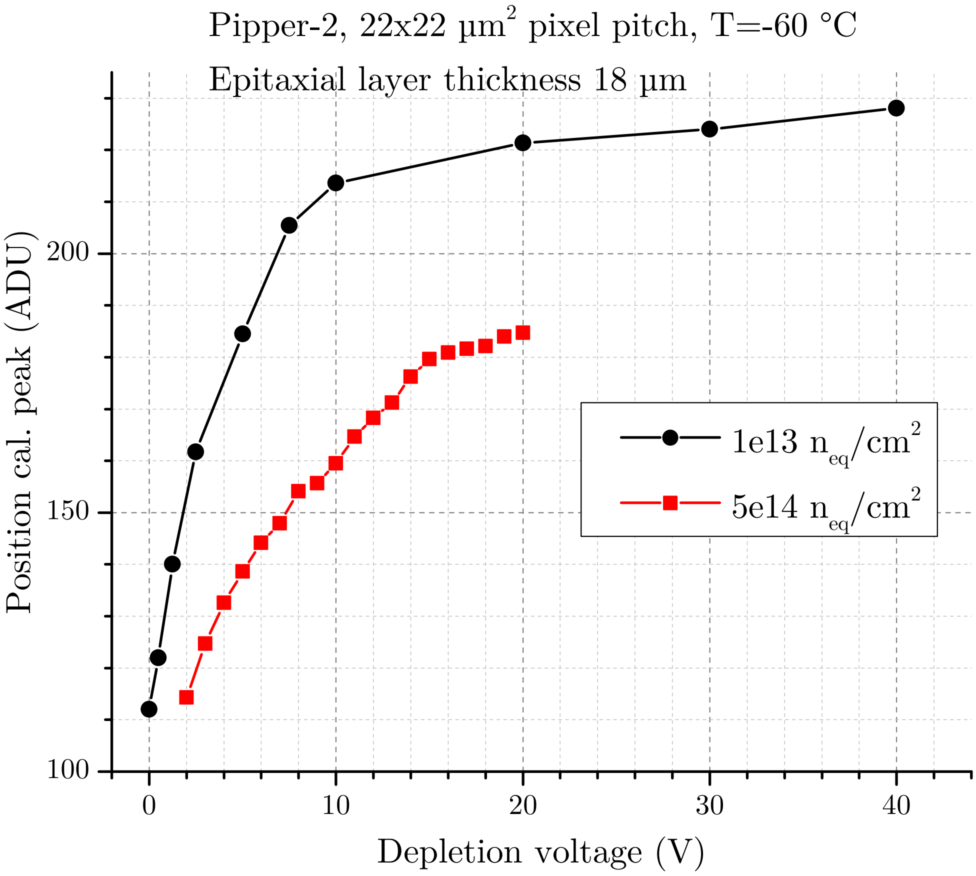

Figure 6.11: Measured position of the calibration peak produced by the K_α-photons from an Fe-55 source in relation to the irradiation level of the Pipper-2 sensor as a function of applied depletion voltage.

as depletion voltage increases (see Equation (2.1)). Figure 6.11 shows a plot of the results. The calibration peak position began to exhibit saturation after a certain point. For the weakly irradiated sensor, saturation appeared to start at around ≈10 V, while for the strongly irradiated sensor, saturation appeared to start at 15 V. Nevertheless, the capacity does not provide a quantitative result of the depletion depth because multiple parallel sources of capacity exist (e.g., side capacities, the AC capacity), which hamper a detailed analysis of capacity. The relation between capacity and depletion depth is highly non-trivial; no simple analytical formula for the relation was found.

6.5.3 Charge sharing

The weakly irradiated sensor should have a higher second-pixel firing rate (i.e., probability that a second pixel will fire in a 3×3 cluster) than the highly irradiated sensors. The radiation damage should alter cluster formation and reduce cluster multiplicity. One of the aims of this experiment was to investigate if a high depletion voltage can enhance charge collection in an irradiated sensor and counteract the radiation damage effects. For this analysis, an Fe-55 source was used to strongly and weakly irradiate the sensors independent of one another under the same conditions at a controlled temperature of −60 °C. By definition, a pixel fires if its collected charge Q_S is five times higher than its average noise σ_mean (see Figure 2.8 for an illustration). Algorithm 1 provides the implemented analysis logic.

```
foreach recorded frame do
    foreach pixel in sensor matrix do
        if $Q_S \geq 5\sigma_{mean}$ then
            /* A pixel fired                                          */
            $totalFiredPixelCounter{+}{+}$;
            foreach immediate neighbor pixel around the fired pixel do
                if $Q_{\mathrm{S}_{neighbor}} \geq 5\sigma_{mean_{neighbor}}$ then
                    /* A second pixel fired                           */
                    $secondPixelCounter{+}{+}$;
                    break;
                end
            end
        end
    end
end
$probabilityForSecondFiredPixel = {}^{secondPixelCounter}/_{totalFiredPixelCounter}$;
```

Algorithm 1: Pseudo-code to calculate the probability of a second fired pixel in a 3×3 pixel cluster (see Figure 2.8 for an explanation of the abbreviations). Results are plotted in Figure 6.12.

Figure 6.12 shows the measured effect of depletion on charge sharing. Note that the strongly radiated sensor ($5 \times 10^{14}\,\mathrm{n_{eq}/cm^2}$) exhibits fundamentally different behavior than the weakly unirradiated sensor ($10^{13}\,\mathrm{n_{eq}/cm^2}$) in the region of low depletion voltages from 0-10 V.

The graphs in figure 6.12 show that the charge sharing in a depleted pixel depends on the applied voltage and the bulk damage of the sensor, especially in the lower depletion voltage region below 10 V. In this region, CPS collect their charge via diffusion and via electrical fields generated by differences in doping concentration. In addition, the two differently irradiated sensors perform very differently in the low depletion voltage region. The weakly irradiated sensor exhibited a high probability that a second pixel would fire, while the highly irradiated senor had a substantially lower probability. Note that for depletion voltages of 10-20 V, both sensors had roughly the same probability (about 30 %) of a second pixel firing.

Interestingly this probability seems to converge and does not fall below a value ≈22 %, as can be seen from the available measurements. Given its pixel dimensions of $22 \times 22\,\mu\mathrm{m}^2$ and thickness of 18 µm, the Pipper-2 pixel matrix can be considered small. Fe-55 γ-rays are expected to convert to signal electrons by chance between neighboring pixels. The resulting localized signal electron cloud, with a radius of about 1 µm, would be collected by multiple pixels simultaneously.

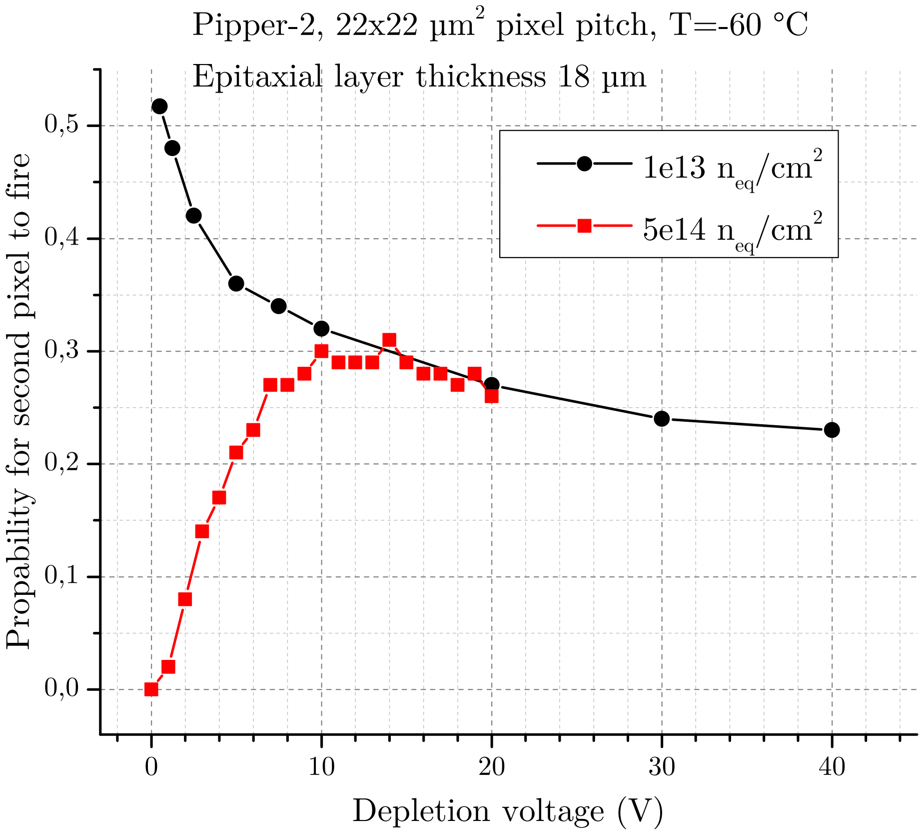

Figure 6.12: Probability of a second pixel to accumulate enough charge to detect a hit, hereby forming a two-pixel cluster with the more prominent seed pixel. Plotted in dependence of the applied voltage and radiation level of a Pipper-2 sensor.

This effect would persist even for fully depleted pixels and be more pronounced for smaller pixel pitches.

6.5.4 Radiation hardness tests using a beta source

A Sr-90 source was used to measure the amplitude spectrum of a Pipper-2 sensor illuminated by a β-source. The overall integral and the number of recorded hits were approximately the same for the strongly irradiated and weakly irradiated sensors. The indicated detection efficiency for β-rays was $(109 \pm 10)\,\%$ (see Figure 6.13). The measurements were made at $-55\,°\mathrm{C}$, and the noise threshold was set to 220 e. The MPV of the $5 \times 10^{14}\,\mathrm{n_{eq}/cm^2}$ irradiated sensor was reduced by one-third; the noise increased by 17.6 % compared to the weakly irradiated sensor (see Figure 6.14). The S/N ratio of the strongly irradiated sensor was 31.3. The weakly irradiated ($10^{13}\,\mathrm{n_{eq}/cm^2}$) sensor had a S/N ratio of 55.6. The optimal S/N value was achieved with a depletion voltage of 20 V, which was the highest voltage applied. We conclude, that that Pipper-2 sensors withstands a radiation dose of at least $5 \times 10^{14}\,\mathrm{n_{eq}/cm^2}$, when cooled properly.

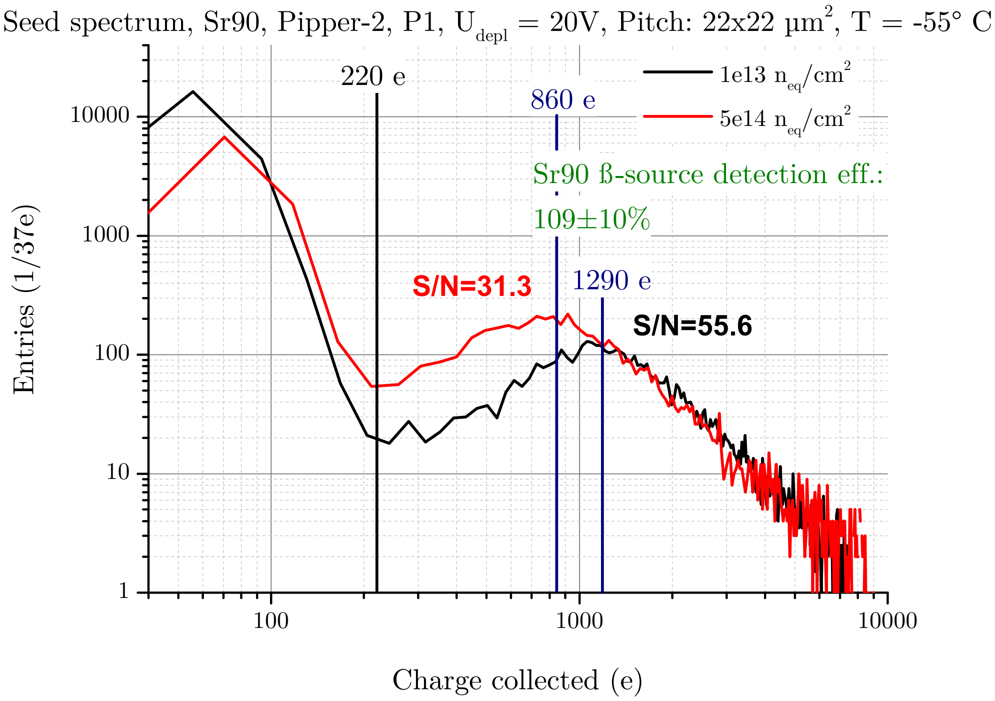

Figure 6.13: The signal response spectrum of a Pipper-2 sensor exposed to a Sr-90 β-source. A highly radiated sensor was compared to a weakly irradiated sensor. The threshold for the β-source detection efficiency calculation was set to 220 e. The S/N values were calculated using the noise measured in Figure 6.14. Published in [LDB17] and [BDL17].

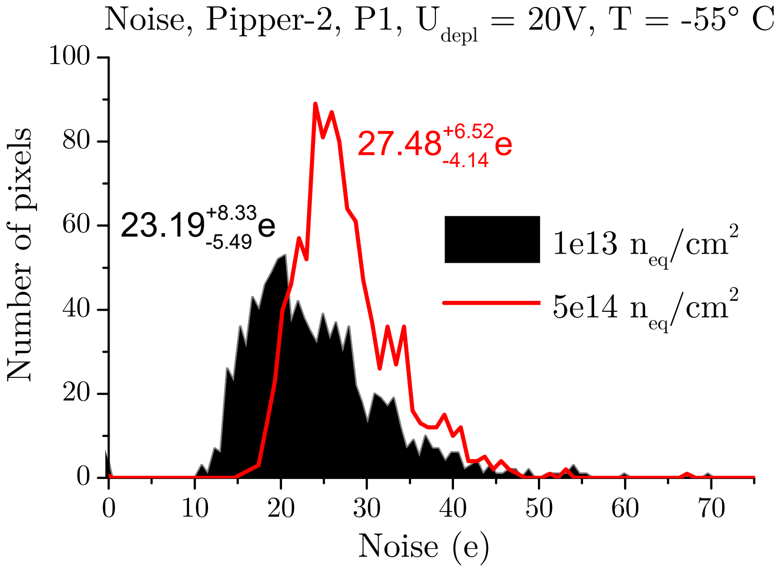

Figure 6.14: The noise of strongly and weakly irradiated Pipper-2 sensors. The related β-source detection efficiency measurements are in Figure 6.13.

Chapter 7

Cold neutrons

> *"The splitting of the atom has changed everything except for how we think."*
>
> ALBERT EINSTEIN

This chapter was published as part of [Lin+17].

The NIEL model [Vas97] assumes that crystal damage caused by massive particles scales with their non-ionizing energy loss (see Section 3.2). The energy deposit is normalized to multiples of 1 MeV neutrons (n_{eq}), under the assumption that the sensor is pure silicon. This assumption is not accurate for p-doped silicon, which contains boron dopants.

Additional NIEL may be generated in p-type boron-doped silicon by neutron-induced fission of the boron dopants through the reaction

$$\mathrm{n} + {}^{10}\mathrm{B} \rightarrow {}^{7}\mathrm{Li} + {}^{4}\mathrm{He} + 2.8\,\mathrm{MeV}$$

Early radiation studies using n-p-n transistors realized in the DMILL process [Man+04][Man+03] suggested that this additional damage is sizable and may exceed the damage expected from 1 MeV neutrons. The standard NIEL model considers such damage negligible.

To exclude the possible impact of thermal neutrons on safe CBM-MVD operation, the radiation damage caused by thermal neutrons in MAPS was studied via estimation of the additional radiation damage caused by fission within the NIEL model framework. In addition, a MAPS prototype was irradiated and tested for radiation damage.

7.1 NIEL caused by neutron-induced boron fission, a theoretical estimate

A theoretical estimate of the impact of neutron-induced boron fission is presented in [Yaz19] and [Lin+17] and is summarized here. Natural boron consists of 19.8 % ^{10}B and 80.2 % ^{11}B. The neutron capture cross-section of ^{11}B is negligible, but it is $\approx$ 3840 b for ^{10}B for thermal neutrons ($E = 0.025\,\mathrm{eV}$, see Figure 7.1a). For the following, it is assumed that manufacturers of standard CMOS electronics use natural boron. The number of boron fissions per volume $n_{\mathrm{reactions}}$ for monoenergetic neutrons with energy E is given by:

$$n_{\mathrm{reactions}} = \sigma(E) \cdot I \cdot N_{\mathrm{P}} \cdot \mathit{\Phi}_{\mathrm{neutron}} \tag{7.1}$$

Here $\mathit{\Phi}_{\mathrm{neutron}}$ is the integrated neutron flux in units of 1/cm^2, N_{P} the doping concentration. $I = 19.8\,\%$ is the isotopic factor of ^{10}B and $\sigma(E)$ represents the energy-dependent cross-section for the n + ^{10}B $\rightarrow^{7}$Li + ^{4}He + 2.8 MeV reaction. The energy of the impinging neutron and the frequent formation of a γ-ray with 478 keV are neglected. Fission energy is 2.8 MeV and provides $E_{\mathrm{Li}} = 1.1\,\mathrm{MeV}$ and $E_{\mathrm{He}} = 1.7\,\mathrm{MeV}$ to the fission products. The range of the ions was simulated with SRIM[1] [ZZB10] and found to amount 6 µm for He and 3 µm for Li in silicon. Most energy is deposited in a Bragg peak at the end of the ion trajectory.

The ions deposit the majority of their energy through ionizing interactions. To estimate non-ionizing energy deposits, the number of crystal vacancies caused by ions were simulated with SRIM and compared to the corresponding number for 10 MeV protons, which have a known hardness factor [Fre+02]. It was assumed that the number of vacancies scales with the hardness factor of the particles. This assumption was tested for several proton energies between 100 keV and 10 MeV and was considered correct, based on an observed standard deviation of 7 %. In the simulation, the helium and lithium ions created an average of 280 and 510 vacancies per ion, respectively; the total number of vacancies per boron fission (VB) was 790. For 10 MeV protons, the hardness factor $k_{\mathrm{p}} = 3.9\,\mathrm{n_{eq}}$ [SB93]; penetrating a 10µm silicon target resulted in $V_{\mathrm{P}} = 684$ vacancies per cm trajectory.

According to the NIEL model, the number of vacancies scales with the magnitude of the non-ionizing energy deposit. If the SRIM simulation is valid, the number of vacancies can be compared to estimate the NIEL of the fission products D_{B} with units of 1 MeV $\mathrm{n_{eq}}$/cm^2. This produces the following equation:

$$D_{\mathrm{B}} = \frac{V_{\mathrm{B}} \cdot k_{\mathrm{P}}}{V_{\mathrm{P}}} \cdot \sigma(E) \cdot I \cdot N_{\mathrm{P}} \cdot \mathit{\Phi}_{\mathrm{neutron}} = 4.5\ \mathrm{cm} \cdot \sigma \cdot I \cdot N_{\mathrm{P}} \cdot \mathit{\Phi}_{\mathrm{neutron}}$$

---

[1] **S**topping Powe**r** of **I**ons in **M**atter

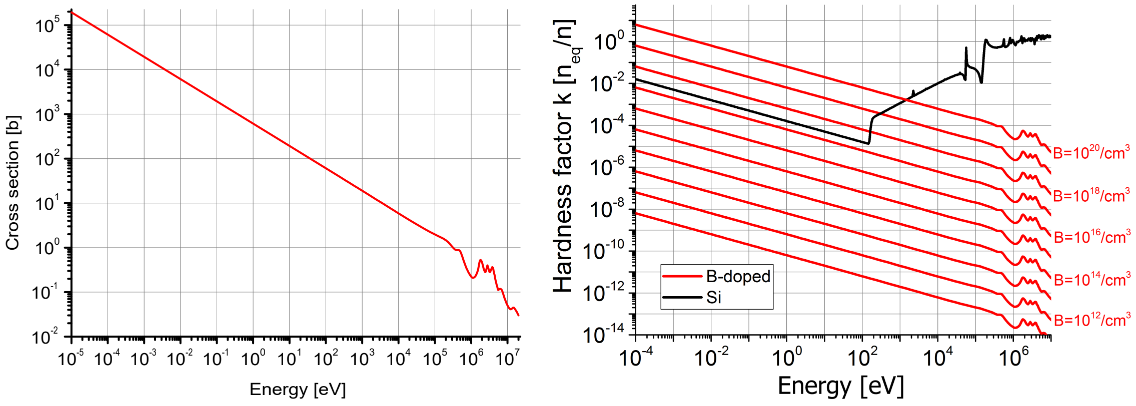

(a)

(b)

Figure 7.1:
(a) Cross section for the n+^{10}B→ ^{7}Li+^{4}He +X reaction. Data from [PS08].
(b) Estimated hardness factor for neutrons impinging pure silicon (black, data from [VL00a]), and predicted damage due to boron fission (red). Data do not support this prediction (see text).

The fission-induced hardness factor for neutrons of a given energy is:

$$k_{\mathrm{B}} = 4.5\ \mathrm{cm} \cdot \sigma \cdot I \cdot N_{\mathrm{P}}$$

Figure 7.1b compares k_{B} of different doping concentrations with the hardness factor of pure silicon. The NIEL from boron fission approached the expected NIEL of pure silicon for doping concentrations above about $\sim 10^{17}/\mathrm{cm}^3$.

The epitaxial layers of typical CMOS sensors have a doping concentration below $10^{15}/\mathrm{cm}^3$; the wells may have a doping concentration $\approx 10^{17}/\mathrm{cm}^3$, and the substrate typically shows a doping $\approx 10^{19}/\mathrm{cm}^3$. Therefore, boron is not expected to cause additional radiation damage to MAPS in the first order, but fission ions created in highly doped structures may travel toward the epitaxial layer and cause bulk damage. Consequently, there may be an increase in diode leakage currents and a decrease in sensor CCE.

7.2 Effects of cold neutrons on CMOS sensors

To investigate the effects of boron fission, MIMOSA-19 sensors were obtained from the PICSEL group of IPHC Strasbourg and irradiated at the FRM II research reactor in Garching. The sensors were manufactured in a 0.35 µm CMOS technology and featured a 14 µm thick epitaxial layer with an anticipated B-doping of a few $10^{15}/\mathrm{cm}^3$. The 196 × 196 3T-Pixels with a pitch of 12×12 µm^2 pitch have L-shaped diodes with 39.6 µm^2 surface. The anticipated doping of the substrate of the p-well is $\approx 10^{19}/\mathrm{cm}^3$.

The chips were irradiated with fast neutrons at the MEDAPP beamline [Bre+08]; the neutrons had a direct fission spectrum with a peak at $E_{\mathrm{neutron}} = 2\,\mathrm{MeV}$, a

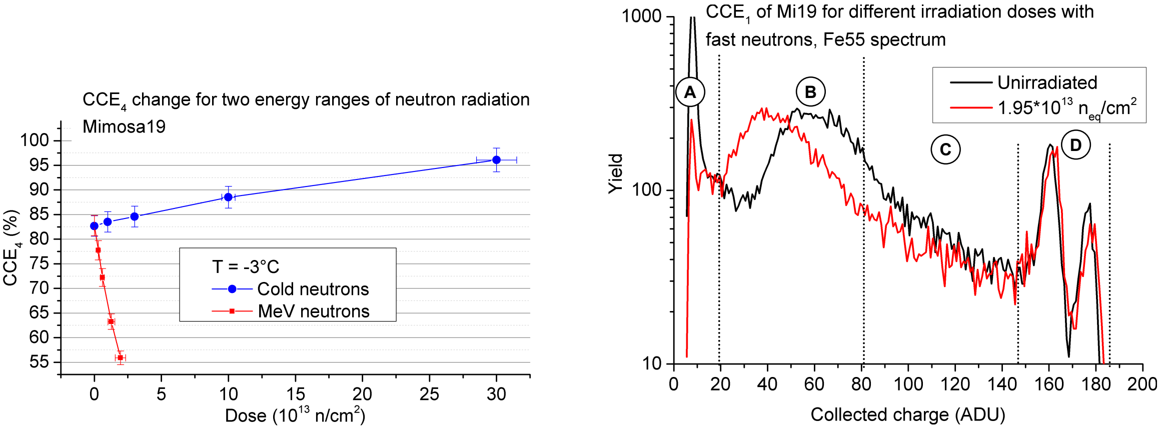

(a) The charge collection efficiency for the four most significant pixels in a 5x5 cluster.

(b) Amplitude spectrum of a reference sensor and a sensor irradiated with fast neutrons.

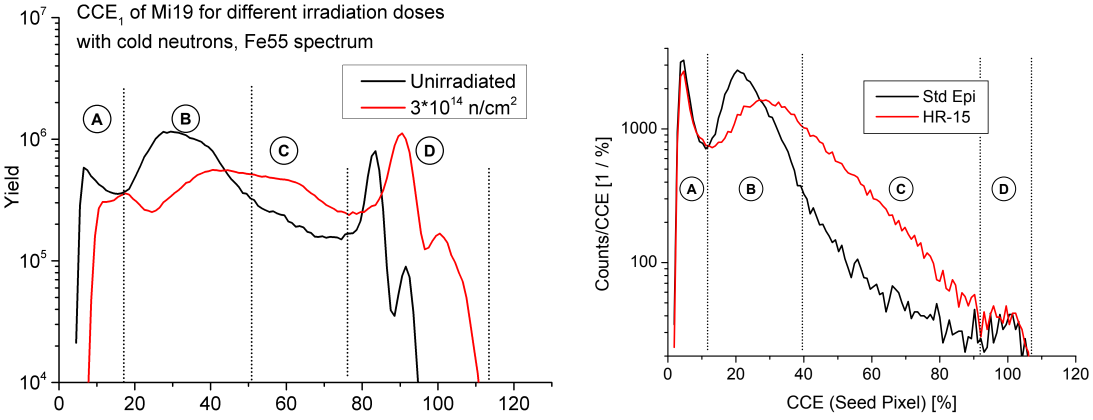

(c) Amplitude spectrum of a reference sensor and a sensor irradiated with cold neutrons.

(d) Comparison of the amplitude spectrum of a MIMOSA-26 sensor with highly (Std Epi) and lowly (HR-15) doped epitaxial layer. From [Dev+11].

Figure 7.2: Charge collection of neutron-irradiated MAPS. The amplitude spectra for intermediate doses follow the trend and were removed from panel 7.2b and 7.2c for the sake of clarity.

hardness factor $k \approx 1\,\mathrm{n_{eq}/cm^2}$ for pure Si, and an energy $E_\mathrm{neutron} > 100\,\mathrm{keV}$ for 99 % of the neutrons. Unwanted γ-rays produced an ionizing dose of $\lesssim 100\,\mathrm{kRad}$ per $10^{13}\,\mathrm{n_{eq}/cm^2}$. Other sensors were irradiated with cold neutrons at the PGAA beam line [Rev15]; the neutrons had an average energy $E_\mathrm{neutron} = 1.8 \times 10^{-3}\,\mathrm{eV}$, a corresponding hardness factor[2] $k = 0.003\,\mathrm{n_{eq}/cm^2}$, and an unknown ionizing dose. The irradiation was performed at room temperature. Although the sensors remained unpowered during irradiation, the ionizing radiation damage likely determined leakage current after irradiation. See Figure 3.3 and Section 3.4.1 for more detail on the neutron beams.

---

[2] As obtained from folding the spectrum given in [Kud+08] with hardness factors according to [VL00a].

The sensors were bonded and illuminated with X-ray sources (^{55}Fe→ 5.9 keV, ^{109}Cd→ 22.1 keV), and their amplitude spectra were recorded according to the standard protocol (see Section 2.5). The summed amplitude spectra for groups of four pixels in X-ray clusters are a good relative measure of the CCE of neutron-irradiated sensors. Previous studies found that the CCE of MAPS with 3T-Pixels was not significantly impacted by ionizing radiation damage (see e.g., [Dev08], section 5.3.3, and 5.3.4.3). A comparison of CCE measurements taken with ^{55}Fe and ^{109}Cd was deemed appropriate due to the linear response from the sensor.

The results from the experiment are displayed in Figure 7.2a. The average CCE of sensors irradiated at MEDAPP *decreased* as radiation dose increased, which matches the results of other studies (e.g., [Dev+11]). In the sensors irradiated at PGAA, the CCE unexpectedly *increased*. As such, the slope of the CCE depended on the neutron energy, which cannot be explained within the NIEL model.

To further investigate this effect, the amplitude spectra of the sensors were closely analyzed, and spectra showing the charge deposited in the seed pixels of the hit clusters were employed. Such a spectrum can be subdivided into four regions (see Figure 7.2b). Region (B) signifies X-rays, which hit the non-depleted epitaxial layer. Region (C) shows hits in an intermediate zone near the depleted volume of the diodes, and region (D) indicates the sensor response to direct hits in the depleted volume. The low-energy region (A) can be ignored here

For sensors irradiated with fast neutrons at MEDAPP (see Figure 7.2b), region (D) remained unchanged (within an acceptable level of uncertainty) after irradiation. Therefore, the properties of the depleted volume were considered unchanged, as well. The peak in (B) shifted to a lower ADU value after irradiation, indicating partial recombination of the diffusion signal charge due to bulk damage.

For the sensor irradiated with cold neutrons at PGAA (see Figure 7.2c), region (B) was mostly depleted after irradiation, and the remaining peak shifted to a higher ADU value. Most of the entries missing in (B) were found in (C). This indicates that the pixel diode had improved CCE for charge created in the nearby epitaxial layer and that there was no significant charge recombination after irradiation. The number of entries in region (D) increased significantly after irradiation. This may imply that the depleted volume of the pixel diode was extended, which would explain the previous observation. Moreover, the peak in (D) shifted toward a higher ADU value; which suggests a reduced diode capacity caused by an extended depleted volume.

The findings cannot be explained by radiation-induced gain modification of the gain for the readout chain amplifiers. A linear modification would shift the peaks in (D) as observed, but the number of entries in the peaks would remain constant, which does not match the observations. Radiation-induced, non-linear modification of the amplifier response curve also cannot explain the modified shape of the spectrum. In this scenario, the peaks in region (D) would be smeared out[3], which was not observed.

A plausible explanation involves substantial, radiation-induced acceptor removal, which would reduce doping of the epitaxial layer and increase the size of the depleted zone of the diode. The number of entries in the peaks of region (D) increased by a factor of slightly over two. For flat PN junctions, this would result in a decrease in doping by a factor of about five.

The presence of acceptor removal is supported by the results of previous studies [Dev+11], which compared the spectra of MIMOSA-26 sensors with highly (Std Epi, few 10^{15} P/cm^3) and lowly doped (HR-15, few 10^{13} P/cm^3) epitaxial layers [Bau+09]. Figure 7.2d illustrates modifications in amplitude spectrum similar to those reported in these studies; the changes were likely caused by reduced doping in regions (B) and (C). There was no significant increase of the depleted volume in region (D), which may be a consequence of the small size and low depletion voltage of the diode in the MIMOSA-26 sensor.

Note that, unless isotope-enriched boron was used for doping, the strong acceptor removal observed cannot be explained solely by the physical destruction of ^{10}B atoms; this is because natural boron contains 80.2 % ^{11}B, which has a small fission cross-section and should remain mostly stable. Transmutation n-doping (i.e., phosphorus production by thermal neutrons in silicon, $n + {}^{30}\text{Si} \rightarrow {}^{30}\text{P} + e + \overline{\nu}_e$) was a possible explanation for these findings, but the number of ^{30}P atoms produced was about three orders of magnitude smaller than the number of missing acceptors, implying this scenario is unlikely.

7.3 Summary and conclusion

The response of B-doped silicon sensors to thermal radiation has been studied using theoretical and experimental methods. Computations based on the NIEL model predicted that the neutron-induced fission of boron dopants in silicon ($n + {}^{10}\text{B} \rightarrow {}^{7}\text{Li} + {}^{4}\text{He} + 2.8\,\text{MeV}$) would add significant bulk damage for a doping concentration $p = 10^{17}/\text{cm}^3$. Ions created in the p-wells and the substrate were expected to damage the active volume of the MAPS, which is too lowly doped to accumulate significant additional damage on its own. Therefore, it was expected that exposure to cold neutrons would reduce the CCE of the sensors. Observations of sensors irradiated with cold neutrons demonstrated that this expectation was incorrect. There was excessive acceptor removal in the sensors irradiated with cold neutrons, which increased the sensors' CCE. However, excessive acceptor removal was not observed in sensors irradiated with fast neutrons and increases the CCE of the sensor; this suggests that cold and fast neutrons generate traps with different properties. The traps created by fast neutrons reduce

---

[3] The dark signal of the pixels (before performing correlated double sampling) is widely spread. A non-linear amplifier response would thus turn into a sizable spread of gain from pixel to pixel. The formation of the peaks observed requires the pixels to show an identical gain.

the lifetime of charge carriers. The traps created by thermal neutrons produce substantial acceptor removal, and any reduction in the lifetime of charge carriers is either negligible or counteracted by the faster charge collection in the lowly doped epitaxial layers.

The sensor reacted to slow and fast neutrons in fundamentally different ways. Therefore, the NIEL model may be ill-suited for parametrizing or predicting radiation damage induced by slow neutrons. Since MIMOSA-19 sensors do not allow for direct access to the doping concentration via methods like C-V measurements of the diode, the findings presented here remain somewhat qualitative; the study should be repeated with suitable test structures.

Chapter 8

Heavy ions

> *"Don't trust atoms,*
> *they make up everything."*
>
> Unknown author

In fixed target heavy-ion experiments like the CBM, vertex detectors are exposed to potentially high doses of relativistic heavy ions from the beam halo and nuclear fragments. If a beam steering fails, the sensors may to face a direct beam impact. A precise understanding of the radiation damage caused by such an event is essential for effectively managing the consequences of this type of exposure.

In silicon, the total ionizing energy deposition of heavy ions can be estimated with the Bethe-Bloch-equation (Figure 2.4). Based on this equation, energy deposition is caused by a beam ion, which scales with the square of its charge ($E_{\text{deposit}} \propto Z^2$). Therefore, a heavy ion can deposit over four orders of magnitude more energy than a proton. Because single event effects introduced by the ions must be studied separately, this forms a valid starting point for estimating the related total ionizing dose (TID).

The total NIEL for heavy ions is not well known – minimal theoretical and empirical knowledge is available. Nuclear nonelastic mechanisms contribute to the NIEL for protons and helium ions at energies above 100 MeV per nucleon. For heavier ions, these non-Coulombic interactions become even more critical. [Xap+04] and [Mes+03] calculated the NIEL for high-energy heavy ions with an atomic number Z of up to 26 (Fe/iron) and with an energy of 200 MeV to 2.1 GeV per nucleon in silicon. The authors focused on radiation studies for natural ion spectrum of cosmic radiation, where "the flux of ions with Z greater than 26 falls off rapidly with increasing Z" [Xap+04]. The results of [Xap+04] are shown in Figure 8.1. The authors compared the damage effects with and without nuclear disintegration and concluded that fragmentation effects become more important at high ion energies. Furthermore, the contribution of primary ion fragmentation to NIEL is negligible, while target fragmentation can become important for incident ions with Z values less than about 10. For protons, target fragmentation contributes

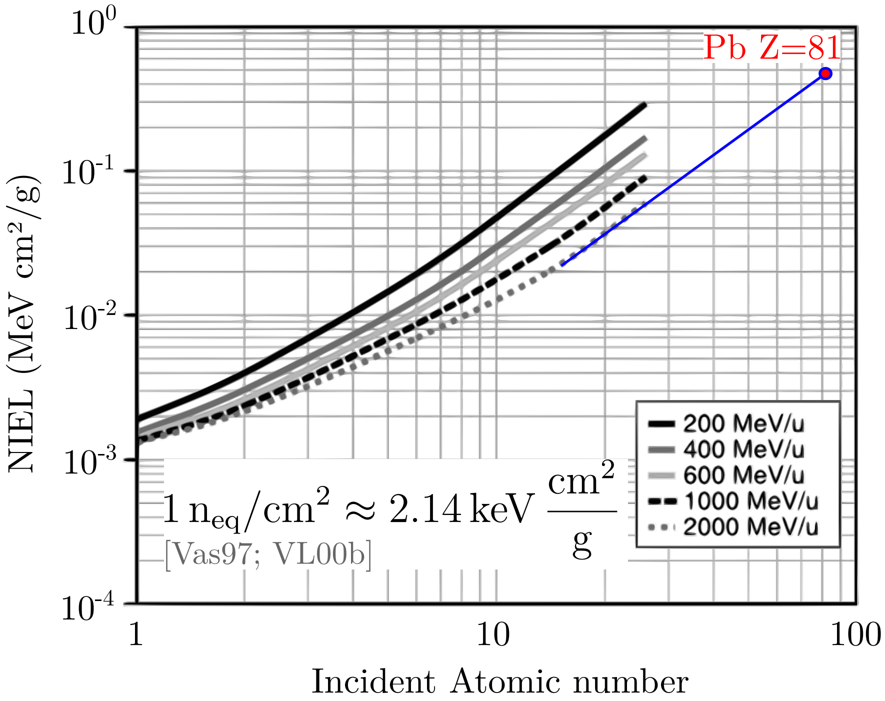

Figure 8.1: Non-ionizing energy loss (NIEL) as a function of the atomic number Z and energy of the ion. An extrapolating line is added in blue. Plot taken from [Xap+04]. The conversion formula for n_{eq}/cm^2 to keV cm^2/g was taken from [Vas97][VL00b].

significantly to the overall NIEL, while for heavier ions with high atomic numbers, the NIEL scales with Z^2 and is dominated by the Coulombic component but not the nonelastic component. The theoretical NIEL curve for high-energy low-Z ions (Figure 3.1) requires a correction due to target fragmentation. However, the NIEL estimated by [Xap+04] for heavy-ion energies much higher than 1 AGeV appears to decrease as particle energy increases, as is suggested by the NIEL tables for protons used in Figure 3.1. A naive extrapolation of the calculations for higher Z values performed by [Xap+04] (see Figure 8.1) suggests that the NIEL of a lead ion (Z=81) with an energy above 2 GeV per nucleon should be lower than a few 100 n_{eq}/cm^2.

8.1 Setup

To test the above estimate experimentally, four MIMOSA-34 THR CPS were exposed to primary 30 AGeV Pb ions at the CERN-SPS beamline [Con16][LDB16][Adu16]. The sensors were covered with aluminum foil and were mounted on a tailored plastic holding structure. For the first tests, the sensors were placed 200 m away from the target of the NA61/SHINE experiment. The flux of ions was estimated by an ion-sensitive 4×4 mm^2 scintillator. PMT signals from the scintillator were forwarded to the counting house, and the dosimetry was performed by counting individual ions. Over the course of two weeks, an ion flux of 1.2×10^{10} Pb ions per cm^2 was measured. The irradiated sensors were bonded at IPHC and illuminated

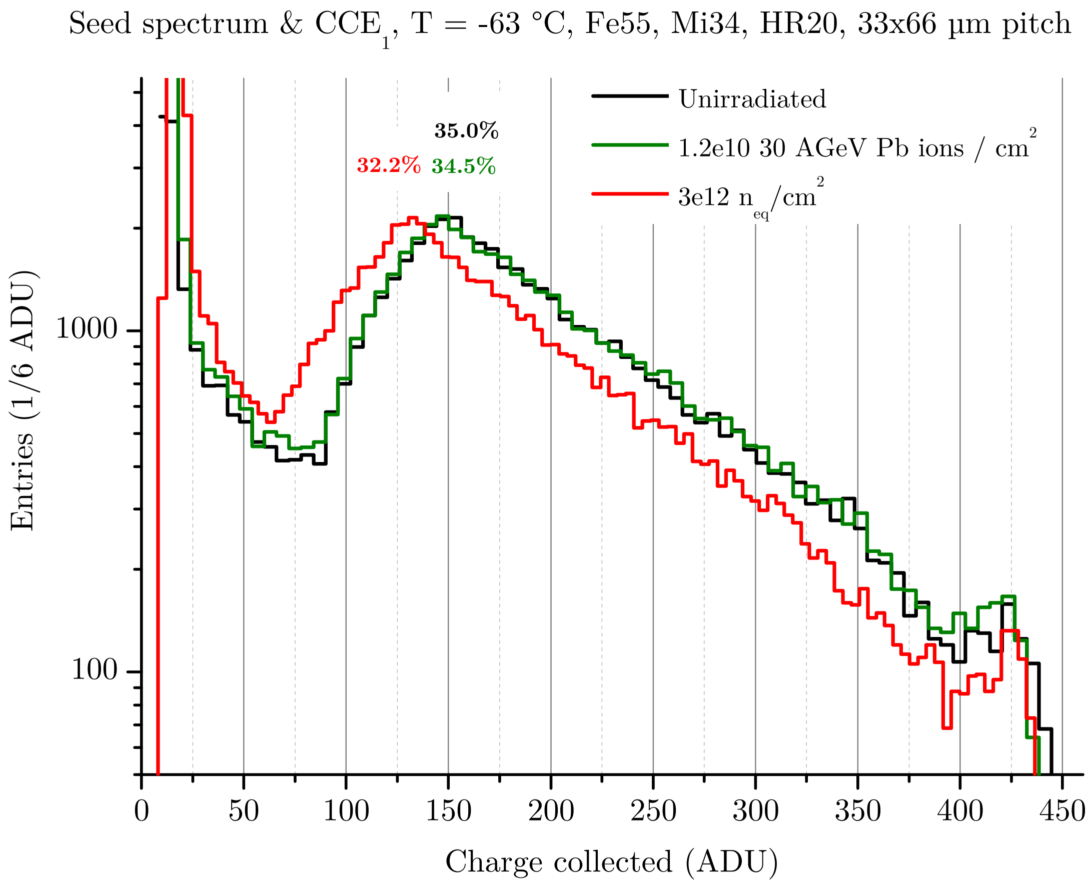

Figure 8.2: One pixel seed spectrum for different temperatures and irradiation levels. The percentages denote the CCE$_1$ of all the sensors. For comparison, a seed spectrum of a neutron-irradiated $3 \times 10^{12}\,\mathrm{n_{eq}/cm^2}$ sensor is also shown. Its CCE$_1$ value is lower than that of the lead irradiation sensors.

with X-rays from an Fe-55 source at the IKF. To determine the radiation damage, the extracted CCE$_1$ and CCE$_{25}$ values were compared to those of a non-irradiated sensor of the same type.

8.2 Results

The aim of this experiment was to estimate the integrated, non-ionizing radiation damage caused by the heavy ions. To do so, the CCE was measured. Leakage current occurs as a result of ionizing radiation damage, but this was not the area of interest, so the sensors were cooled to suppress leakage currents and exclude the effect of ionizing radiation-produced shot noise. The most ion-irradiated sensor was compared to identical MIMOSA sensors with known bulk damage. It was assumed that a comparable CCE corresponds to a comparable dose of non-ionizing irradiation.

Figure 8.2 shows the uncalibrated Fe-55 CCE$_1$ spectrum for the most irradiated MIMOSA-34 sensor. The sensor CCE was compared to that of an unirradiated

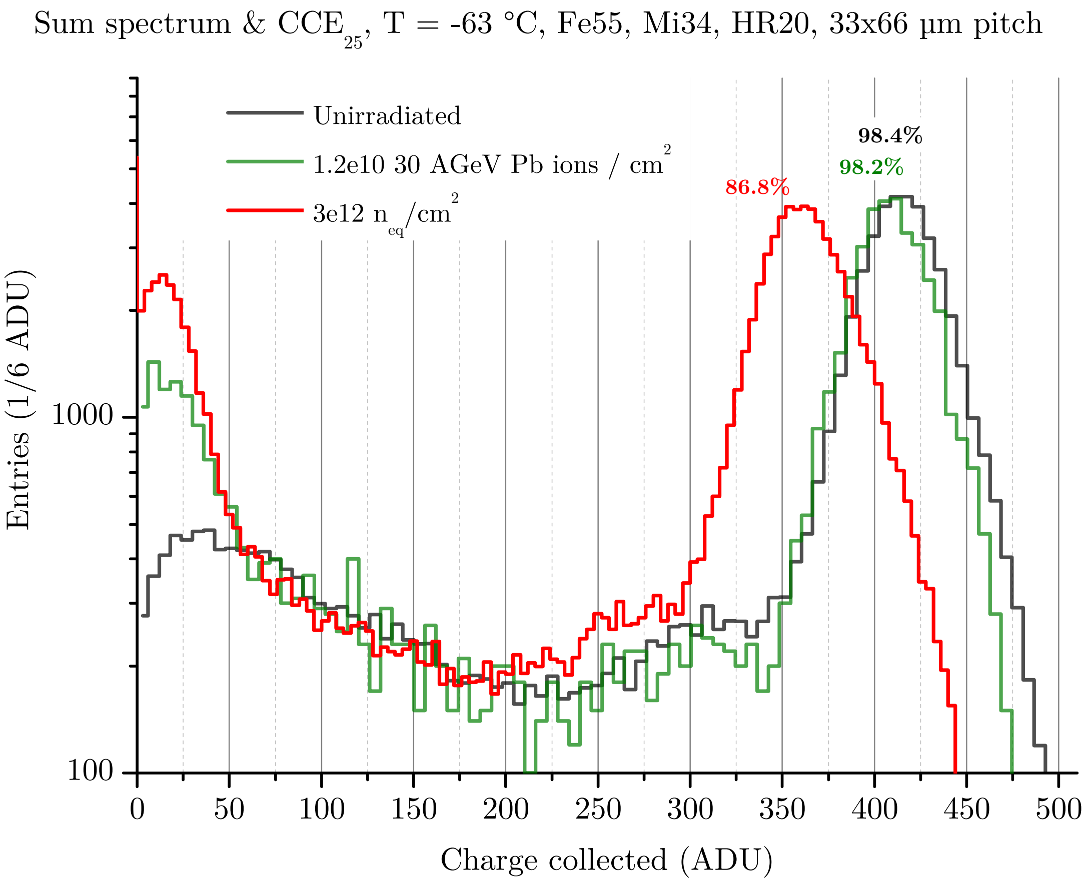

Figure 8.3: Spectra for 5×5 pixel clusters at different temperatures and irradiation levels. The percentages denote the CCE$_{25}$ of the irradiated sensors.

sensor at a temperature of −63 °C. A pixel with a pitch of $33 \times 66\,\mu\text{m}^2$ was chosen for this analysis, as it is the biggest, and therefore the most radiation-soft, pixel on the MIMOSA-34 sensor. Table 4.1 provides the exact pixel properties. The SB-Pixel diode size is $8\,\mu\text{m}^2$, and the diode footprint is $15\,\mu\text{m}^2$. The high-resistivity epitaxial layer of the compared sensors is 20 µm thick and is denoted as HR20 in this thesis.

The CCE$_1$ value at −63 °C for the 1.2×10^{10} 30 *A*GeV Pb ions/cm^2 irradiated MIMOSA-34 sensor was 33.6 %; the CCE$_1$ value of the non-irradiated sensor was 31.6 %. Figure 8.3 reports the CCE$_{25}$ values, which are the summed CCE values of a 5×5 pixel cluster, and the sum spectra for the sensors. The irradiated sensor had a CCE$_{25}$ value of 98.2 %, performing slightly worse than the non-irradiated sensor, which had a CCE$_{25}$ value of 100 %. The uncalibrated raw spectra indicate that there was almost no shift in the gain. The average pixel noise distributions of the reference sensor and the lead-irradiated sensor were also compared at 20 °C. There was no significant increase due to irradiation.

Overall, the discrepancy between the values is close to the uncertainty of the measurement procedure when considering statistical and systematic errors. The position of the signal peaks around 425 ADU, as well as the changes in signal amplitude and CCE values 5 %, depends only marginally on the radiation dose. As such, the irradiation dose used likely does not impair sensor performance. Previous studies (see Chapter 5) have shown significant damage to this type of sensor at non-ionizing radiation doses of $10^{13}\,\mathrm{n_{eq}/cm^2}$. However, first signs of radiation damage have been observed at doses $\approx 3 \times 10^{12}\,\mathrm{n_{eq}/cm^2}$. Based on these findings, it can be concluded that 1.2×10^{10} 30 AGeV lead ions do not cause significant radiation damage; the upper limit for the hardness factor of 30 AGeV Pb ions is therefore $k_{\mathrm{ion}} \leq 300\ \mathrm{n_{eq}}$. These results were published as part of [Dev19] and presented in [Lin+17].

Chapter 9

Summary

> *“The limits of the possible can only be defined by going beyond them into the impossible”*
>
> ---
>
> Arthur C. Clarke

This thesis explores the effect of non-ionizing radiation damage on different generations. For each generation, different aspects of sensor design were the area of focus. The 3T-pixels of the MIMOSA-19 sensors allow for a detailed study of leakage current, and leakage current was used to study the effects of neutron-induced fission on boron dopants induced by slow neutrons. There was excessive acceptor removal, an effect not seen in sensors irradiated with fast neutrons. In those sensors, CCE increased. The MIMOSA-34 sensors have 30 sub-matrices per chip, each with a different combination of parameters. This made these sensors particularly well suited to investigate sensor performance as a function of design properties and identify the optimal set of parameters experimentally. IPHC designed these sensors with different epitaxial layers, which allowed for the study of sensor performance counters dependent on the epitaxial layer used. The HR18 layer showed the most promising results and was the epitaxial layer used in subsequent designs. MIMOSA-34 THR sensors were exposed to 1.2×10^{10} $30\,A\mathrm{GeV}$ lead ions to estimate possible damage by beam ions in a heavy ion experiment. This dose did not cause significant radiation damage. I studied the effects of depletion using the P13 matrix on a MIMOSA-34 sensor and on sensors more specialized for depletion (Pegasus and Pipper-2 sensors). Measurements, theoretical calculations, and TCAD simulations suggested that the MIMOSA-34 sensor does not reach full depletion. A study using 20 V on a Pipper-2 sensor showed that active depletion helps the sensor reach a non-ionizing radiation hardness of $5 \times 10^{14}\,\mathrm{n_{eq}/cm^2}$.

In this thesis, progress was made toward a better understanding of the effects of non-ionizing radiation damage and CPS depletion. Such an understanding will help to better utilize CPS in future detectors.

Appendices

Appendix A

Computations for small-diode depletion

A.1 Assumptions

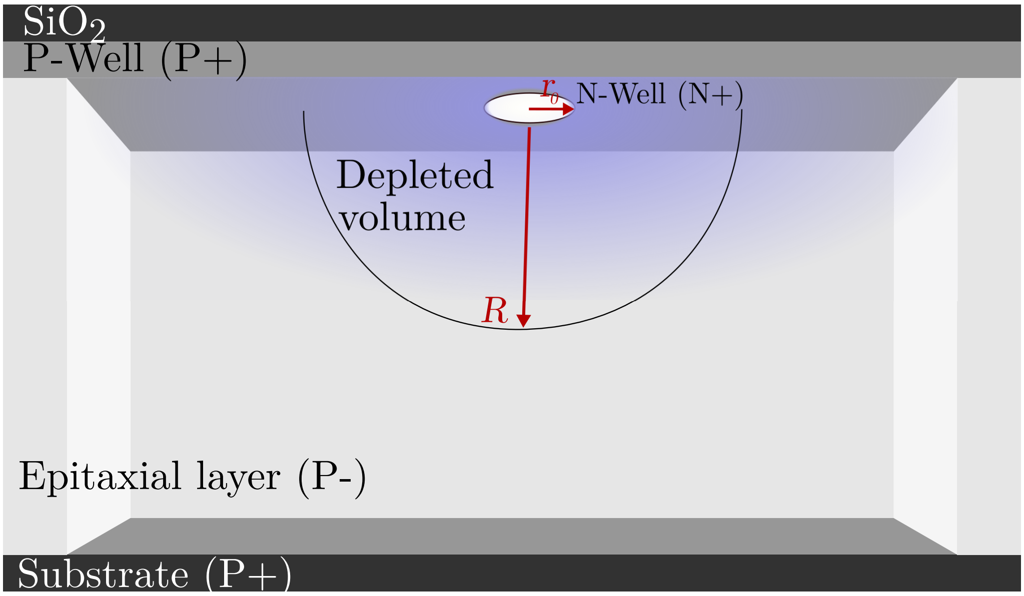

Figure A.1: Three-dimensional schematic of an open cut pixel. A cylindrical n-well is embedded in the p-well, which represents the N-doped depletion diode.

In the following computation, a simplified geometry for a MAPS cell is assumed, as shown in Figure A.1. The cell pictured above has four layers. The top layer is non-conductive SiO_2. The next layer is a strongly p-doped (boron) p-well with an implanted n-well that represents a small collection diode. The n-well is cylindrical, with a radius r and height h, and is highly n-doped, with a doping concentration N_{D}. The third layer is an active medium made from a weakly p-doped epitaxial layer; it has a thickness d_{epi} and a doping concentration N_{A}. The capacity of the diode toward possible structures above the SiO_2 layer (e.g., metal layers) was neglected. Electrical fields radiating from the n-well toward

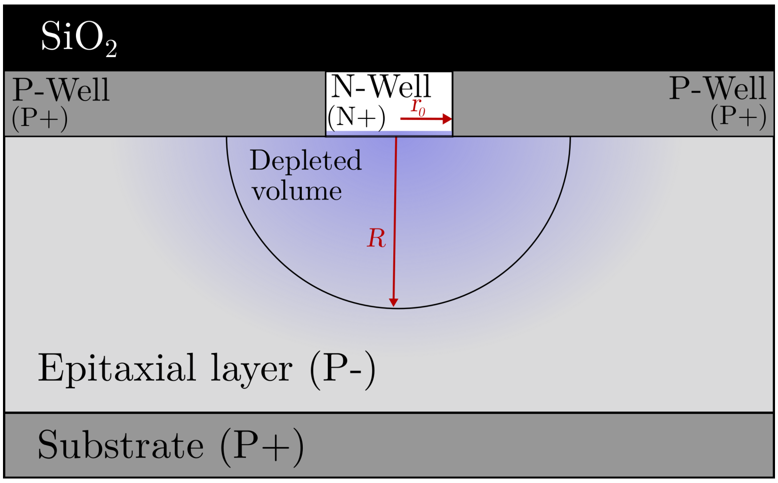

Figure A.2: Side view of an pixel. The depleted area is assumed to form a hemisphere with a radius R inside the epitaxial layer.

the adjacent, highly p-doped p-wells were also neglected. These fields effectively reduce the n-well radius r_0. Furthermore, it was assumed

$$N_\mathrm{D} \gg N_\mathrm{A} \quad .$$

This assumption is based on the fact that the p-doping concentration N_A is usually around the order of $10^{12} - 10^{15}\,\mathrm{cm}^{-3}$, while the n-doping concentration N_D is usually of an order greater than $10^{16}\,\mathrm{cm}^{-3}$. From these assumptions, the depletion depth and the capacity of this small junction was computed. This small junction which acts as a diode in CMOS MAPS. This calculation does not claim to describe real conditions accurately, it just shows that simple assumptions can lead to depletion behavior very different from that of an abrupt PN junction. Section 6.1 compares this equation to TCAD simulations, the abrupt PN junction hypothesis, and measured data.

A.2 Diode charge

As discussed in Section 2.3, the depleted zone of a PN junction does not contain majority charge carriers; these charge carriers have been moved to the oppositely doped side of the junction. Consequently, each side of the diode has a total charge of

$$Q = \pm V_\mathrm{depl.} \cdot N_\mathrm{eff} \cdot e$$

Here, $V_\mathrm{depl.}$ denotes the depleted volume at either the p- or n-doped side of the PN junction, and N_eff is the number of dopants per cubic centimeter on that side; the equation must be positive for the ndoped region and negative for the p-doped region. The charge of the junction emanates from the highly n-doped structure. Therefore, only a thin skin around the cylindrical n-well is depleted. The volume of this depleted thin skin is approximately

$$V_{\mathrm{Ndepl}} \approx d \cdot 2\pi r_0^2, \quad \text{where}$$

d is the depletion depth of the n-well and
$2\pi r_0^2$ is the surface of the circular cylinder.

Therefore, the charge in the depleted region of the n-side is

$$Q = -V_{\mathrm{Ndepl}} \cdot N_{\mathrm{D}} \cdot e, \quad \text{where} \tag{A.1}$$

N_{D} is the n-doping concentration of the n-well and
e is the electron charge.

The depletion volume of the epitaxial layer is assumed to be a hemisphere with radius R, and the volume is given by

$$V_{\mathrm{Pdepl}} = \frac{2}{3}\pi R^3, \quad \text{where}$$

R is the radius of the depleted hemisphere in the epitaxial layer (see Figure A.2). As such, the charge on the p-side is given by

$$Q = V_{\mathrm{Pdepl}} \cdot N_{\mathrm{A}} \cdot e \quad \text{,where} \tag{A.2}$$

N_{A} is the p-doping concentration of the epitaxial layer. Note that the sign of Equation (A.2) is opposite the sign of Equation (A.1). The charges on the p-side and n-side of the diode must be opposite in sign and equal in quantity. Therefore Equation (A.2) and A.1 can be equated:

$$\frac{2}{3}\pi R^3 \cdot N_{\mathrm{A}} \cdot e = d \cdot 2\pi r^2 \cdot N_{\mathrm{D}} \cdot e \quad .$$

This equation can be solved for the thickness d of the depleted zone in the n-well or for the radius R of the depleted hemisphere in the p-doped epitaxial layer:

$$\begin{aligned} d &= \frac{2}{3}\frac{N_{\mathrm{A}}}{N_{\mathrm{D}}}\frac{R^3}{r^2}, \\ R^3 &= \frac{3}{2}\frac{N_{\mathrm{D}}}{N_{\mathrm{A}}} r^2 d \end{aligned} \tag{A.3}$$

On the n-side of the junction, the electric field is given by:

$$E_{\mathrm{N}}(z) = \int_{-d}^{z} \frac{eN_{\mathrm{D}}}{\epsilon}\,\mathrm{d}z' = \frac{eN_{\mathrm{D}}}{\epsilon} z, \quad \text{where}$$

ϵ is the electric constant in silicon.

The maximum field strength can be calculated by inserting the thickness d of the depleted zone into the equation:

$$E_{\mathrm{N}}^{\mathrm{max}} = \frac{eN_{\mathrm{D}}}{\epsilon} d \quad . \tag{A.4}$$

Accounting for Equation (A.3) the maximum field amounts:

$$E_{\mathrm{N}}^{\mathrm{max}} = \frac{eN_{\mathrm{D}}}{\epsilon} \frac{2}{3} \frac{N_{\mathrm{A}}}{N_{\mathrm{D}}} \frac{R^3}{r^2} = \frac{2}{3} \frac{eN_{\mathrm{A}}}{\epsilon} \frac{R^3}{r^2} \quad . \tag{A.5}$$

The voltage drop over the n-side of the implementation is

$$\begin{aligned} U_1 &= \int_0^d E_{\mathrm{N}}(z)\,\mathrm{d}z = \int_0^d \frac{eN_{\mathrm{D}}}{\epsilon} z\,\mathrm{d}z = \frac{eN_{\mathrm{D}}}{2\epsilon} z^2 \\ &= \frac{2}{9} \frac{e}{\epsilon} \frac{N_{\mathrm{A}}^2}{N_{\mathrm{D}}} \frac{R_{max}^6}{r^4} \quad . \end{aligned}$$

The n-implementation should emit a spherical, symmetrical field into the epitaxial layer. The magnitude of the field and the density of the field lines decrease proportionally with the inverse square of the distance r from the small n-well implementation. To model the transition from the linear field in the n-well to the radial behavior in the p-doped epitaxial layer, it is assumed that the the electrical flux $\mathit{\Phi} = A \cdot E_{\mathrm{N}}^{\mathrm{max}}$ is always conserved. A is the traversed area, while $E_{\mathrm{N}}^{\mathrm{max}}$ is defined by Equations (A.4) and (A.5). At the n-side of the transition region, the flux $\mathit{\Phi}_{\mathrm{N}}$ is characterized by the circular surface of the n-doped implementation ($A_{\mathrm{N}} = \pi r_0^2$). On the p-side, I assumed the electric field lines traverse a hemisphere with radius r ($A_{\mathrm{P}} = 2\pi r_0^2$). From $\mathit{\Phi}_{\mathrm{P}} = \mathit{\Phi}_{\mathrm{N}}$, it can be concluded that

$$E_{\mathrm{P0}}(r_0) = \frac{1}{2} E_{\mathrm{N}}^{\mathrm{max}} \quad .$$

Field strength at the outermost points of the epitaxial layer is reduced according to the r^2 law:

$$E_{\mathrm{P0}}(r > 0) = \frac{r_0^2}{r^2} E_{\mathrm{P0}}(r_0) = \frac{r_0^2}{r^2} \frac{1}{3} \frac{eN_{\mathrm{A}}}{\epsilon} \frac{R^3}{r_0^2} \quad .$$

On the p-side ($r_0 < r < R$), the electric field strength is given by:

$$\begin{aligned} E_{\mathrm{P}}(r) &= E_{\mathrm{P0}}(r) - \frac{eN_{\mathrm{A}}}{\epsilon r^2} \int_{\mathrm{r}_0}^{r} r'^2 \,\mathrm{d}r' \\ &= E_{\mathrm{P0}}(r) - \frac{eN_{\mathrm{A}}}{\epsilon r^2} \frac{r^3 - r_0^3}{r^2} \\ &= \frac{1}{3} \frac{eN_{\mathrm{A}}}{\epsilon} \frac{R^3}{r^2} - \frac{eN_{\mathrm{A}}}{3\epsilon} \frac{r^3 - r_0^3}{r^2} \\ &= \frac{eN_{\mathrm{A}}}{3\epsilon} \frac{R^3 - r^3 + r_0^3}{r^2} \\ &\approx \frac{eN_{\mathrm{A}}}{3\epsilon} \frac{R^3 - r^3}{r^2} \quad . \end{aligned}$$

The voltage drop over the p-side of the implementation, namely of the epitaxial layer, is given by:

$$\begin{aligned}
U_2 &= \int\limits_{r_0}^{R} E_{\mathrm{p}}(r)\,\mathrm{d}r \\
&= \frac{eN_{\mathrm{A}}}{3\epsilon} \int\limits_{r_0}^{R} \frac{R^3 - r^3}{r^2}\,\mathrm{d}r \\
&= \frac{eN_{\mathrm{A}}}{6\epsilon} \frac{(r_0 - R)^2 (r_0 + 2R)}{r_0} \\
&\approx \frac{eN_{\mathrm{A}}}{3\epsilon} \frac{R^3}{r_0} \quad .
\end{aligned}$$

The total voltage drop is a potential and is therefore additive:

$$\begin{aligned}
U &= \int E(r)\,\mathrm{d}r \\
&= U_1 + U_2 \\
&= \frac{2}{9} \frac{e}{\epsilon} \frac{N_{\mathrm{A}}^2}{N_{\mathrm{D}}} \frac{R^6}{r_0^4} + \frac{eN_{\mathrm{A}}}{3\epsilon} \frac{R^3}{r_0} \\
&= AR_3^2 + BR_3, \quad \text{where} \qquad \text{(A.6)} \\
A &:= \frac{2}{9} \frac{e}{\epsilon} \frac{N_{\mathrm{A}}^2}{N_{\mathrm{D}} r_0^4}, \\
B &:= \frac{eN_{\mathrm{A}}}{3\epsilon r_0} \quad \text{and} \\
R_3 &:= R^3 \quad .
\end{aligned}$$

Solving the quadratic Equation (A.6) for the cubic maximum radius R_3 gives:

$$\begin{aligned}
R_3 1 &:= \frac{\sqrt{B^2 + 4AU} - B}{2A} \\
R_3 2 &:= -\frac{\sqrt{B^2 + 4AU} + B}{2A}
\end{aligned}$$

For $U = 0\,\mathrm{V}$, $R_3 2(U)$ yields a negative radius of $-B/A$ since A and B are both always positive. Therefore, only $R_3 1(U)$ has a physical solution, with $R_3 1(U = 0\,\mathrm{V}) = 0$, which is reasonable. $R_3 := R_3 1$ is used hereafter. Using the expressions for A and B and transforming the terms leads to the following result:

$$\begin{aligned}
R_3 &= \frac{\sqrt{B^2 + 4AU} - B}{2A} \qquad \text{(A.7)} \\
R_3 &= \frac{B}{2A} \left(\sqrt{1 + \frac{4A}{B^2} \cdot U} - 1 \right) \\
R_3 &= \frac{3N_{\mathrm{D}}}{4N_{\mathrm{A}}} r_0^3 \left(\sqrt{1 + \frac{8\epsilon}{N_{\mathrm{D}} r_0^2 e} \cdot U} - 1 \right) \\
R &= \sqrt[3]{\frac{3N_{\mathrm{D}}}{4N_{\mathrm{A}}} r_0^3 \left(\sqrt{1 + \frac{8\epsilon}{N_{\mathrm{D}} r_0^2 e} \cdot U} - 1 \right)} \qquad \text{(A.8)}
\end{aligned}$$

N_D	$10^{16}\,\mathrm{cm}^{-3}$,
N_A	$10^{14}\,\mathrm{cm}^{-3}$,
e	$1.602\,176\,620\,8 \times 10^{-19}\,\mathrm{C}$,
r_0	$1\,\mu\mathrm{m}$,
ϵ	$11.68 \cdot 8.854\,187\,817 \times 10^{-12}\,\mathrm{Fm}^{-1}$.

Table A.1: Physical parameter values used in this section if not stated otherwise.

Equation (A.8) shows that the radius R of the hemispherical depleted volume grows with the sixth-root of the depletion voltage U. Equation (A.8) can be approximated by using the physical parameters of CMOS. Realistic values of the parameters were chosen (see Table A.1). These parameters show that B^2 is generally much larger than $4AU$ due to the difference in doping concentrations N_A and N_D:

$$\begin{aligned} 4AU \propto A \propto N_\mathrm{A}^2/N_\mathrm{D} &\quad \text{, and} \\ B^2 \propto N_\mathrm{A}^2 &\quad \text{; therefore,} \\ \frac{B^2}{4AU} \propto \frac{1}{N_\mathrm{D}} \ll 1 &\quad . \end{aligned}$$

With $B^2 \gg 4AU$ one can approximate Equation (A.7) as

$$\begin{aligned} R_3 &= \frac{\sqrt{B^2 + 4AU} - B}{2A} = \frac{B \cdot \sqrt{1 + \frac{4AU}{B^2}} - B}{2A} \approx \frac{B + \frac{2AU}{B} - B}{2A} = \frac{U}{B} \\ R &= \sqrt[3]{\frac{3\epsilon r_0}{e N_\mathrm{A}} U} \end{aligned} \tag{A.9}$$

Figure A.3a compares the approximation to the full solution for doping concentrations $N_\mathrm{D} = 10^{16}\,\mathrm{cm}^{-3}$ and $N_\mathrm{A} = 10^{14}\,\mathrm{cm}^{-3}$. For small values of U, the approximation slightly overestimates the depletion radius. The estimation is better for more divergent values of N_D and N_A. Figure A.3b provides a graphical comparison of different doping concentration values N_D and N_A. As expected, lower values of N_A in the epitaxial layer significantly affect the depletion volume. Nevertheless, it is hard to deplete CMOS sensors with small collection diodes. Section 6.1 discusses this challenge and uses this theoretical formula.

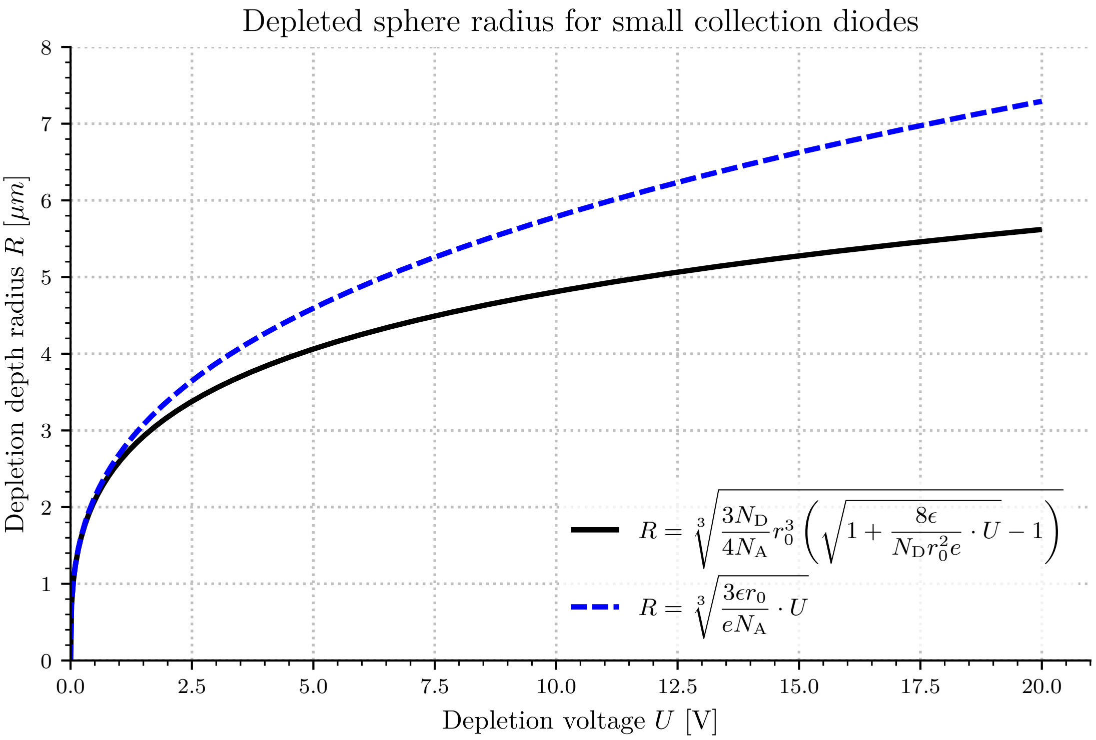

(a) Comparison of Equation (A.8) and the approximation given in Equation (A.9). The parameters used in this graphic are given in Table A.1.

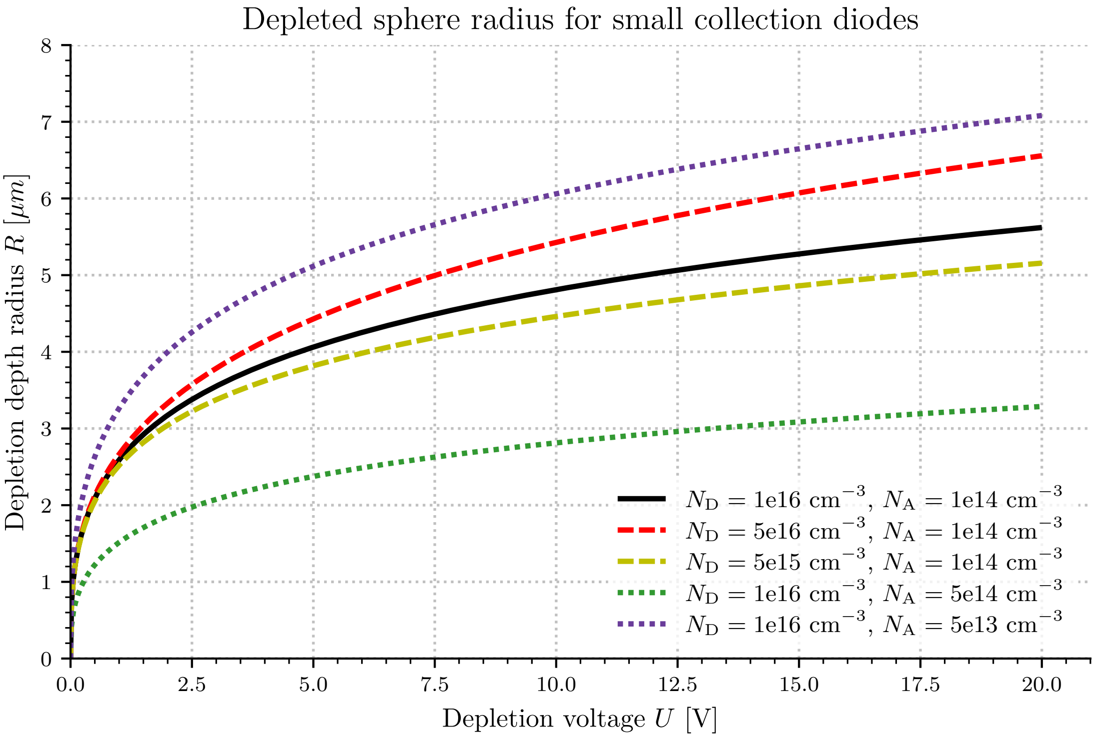

(b) Relation between depletion radius R and depletion voltage U with regard to doping concentration values (N_A and N_D). The black line is plotted using the default values shown in Table A.1. The dashed lines are for varying values of N_D, and the dotted lines are for varying values of N_A. Higher values of N_D and lower values of N_A resulted in steeper depletion curves $R(U)$. Changing N_A had a greater influence on the depletion depth R than changing N_D.

Figure A.3

Appendix B

MABS

A dedicated software package was developed and tested to complete the various tasks and experiments described in this thesis. The software package consists of the following components:

- a relational MySQL database with a search-able web interface
- an automated test stand control system used to take data (MABS)
- a CERN ROOT based analysis framework used for analysis (MABS Run Analyzer)

Each component can interact with the others to store and retrieve test results. The automated setup and the concept were presented at the DPG[1] 2014 and were awarded the third poster prize [Lin14a].

The tools available at the beginning of this thesis were not sophisticated enough and were ill-suited for an efficient analysis of hundreds of different data samples with high statistics. As such, a software package named "MABS Run Analyzer" was written in C++ [Str13] using the CERN ROOT framework in version 6.17/01 [BR97]. The class-driven 11 000-line code connects directly to a MySQL database and to the file system where the automated test stand stores the meta-data and raw data. The software can read and write observables to a searchable database, making it easier to manage thousands of different data measurements. It is maintained with source control and a more complete documentation can be found online at [Lin14b]. Within a three month long measurement campaign on MIMOSA-34 an active measurement time of 72 % could be achieved. In total, 1.6 Tbyte of data could be recorded during this 1700 h measurement campaign. MABS was also used by previous studies [Doe15][Yaz19][Bus19].

This code was used to obtain most of the findings described in this thesis, so a short introduction into the code structure and analysis logic is provided here.

---

[1] **D**eutsche **P**hysikalische **G**esellschaft

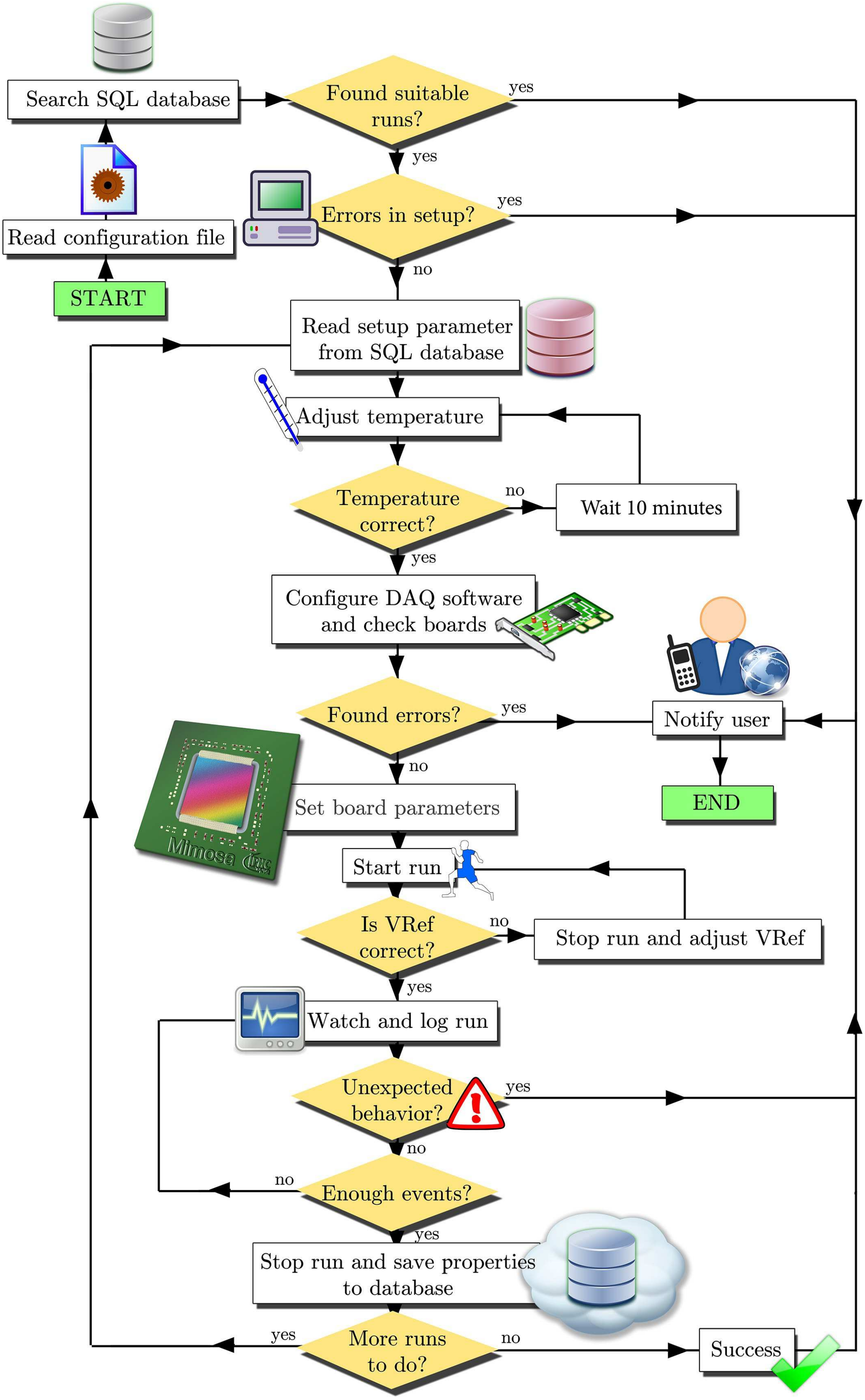

Figure B.1: A simplified logic sketch used to perform the automated measurements under continuously monitored stabilized conditions.

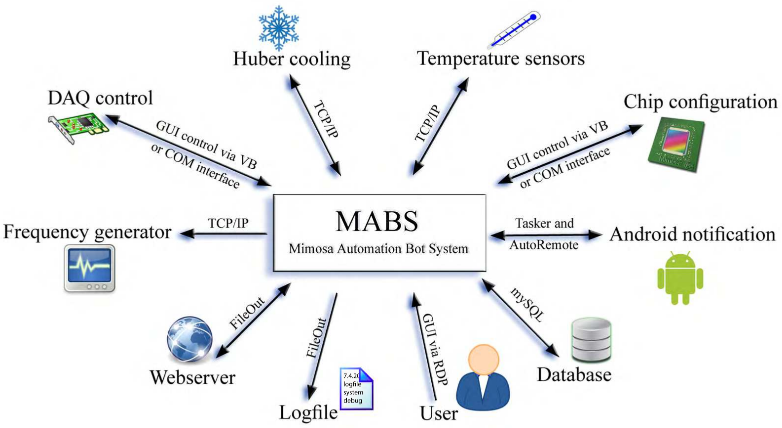

Figure B.2: In and output channels that MABS uses to accomplish its tasks.

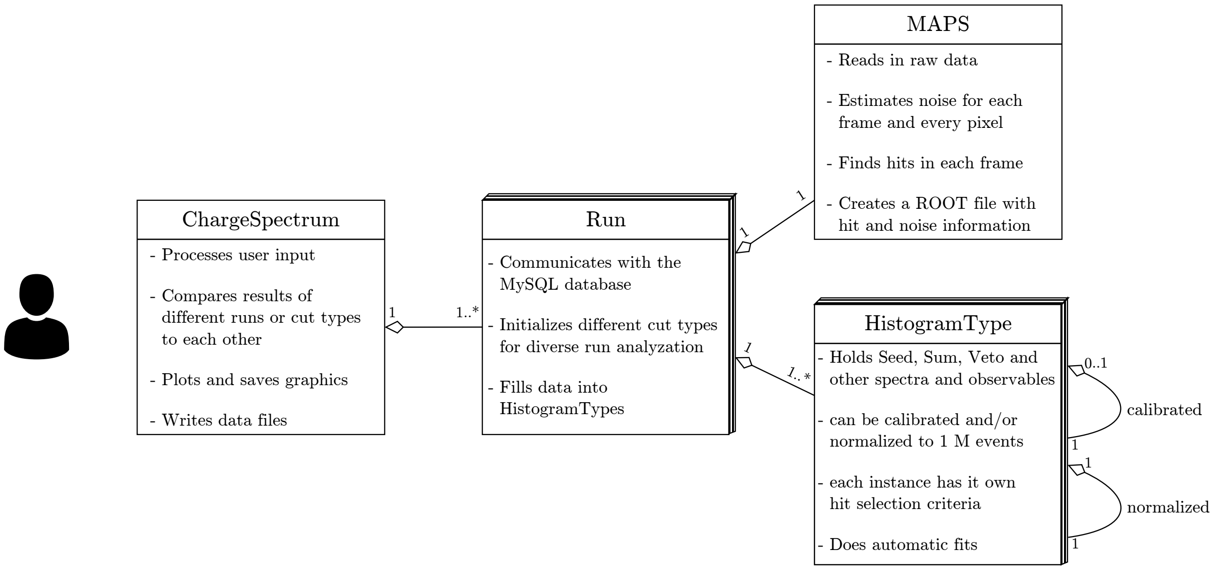

Figure B.3: Simplified UML[2] diagram of the C++ MABS Run Analyzer classes used for the experimental data evaluations. A complete UML diagram, the code and its full documentation are available online [Lin19].

"MABS Run Analyzer" consists mainly of three classes. The main class, "ChargeSpectrum" processes the user command line inputs and, based on these inputs, begins various analytical scenarios and organizes overall program flow. Each data measurement was assigned a unique number in the database. This number, in combination with the corresponding data and observables, is referred to as a "run". When a user requests an analysis of several runs, the main process initializes a "Run" class for each of them. This class organizes all observations and analysis for the specified run. To do so, it requires the processed raw pixel data. For this purpose, each "Run" class initializes a "MABS" class that processes the raw data created by the data measurement software and stores its results in a ROOT file, a data format that is easily accessible to the ROOT framework. As raw data files for one run can be several gigabytes in size, processing such large

---

[2] **U**nified **M**odeling **L**anguage

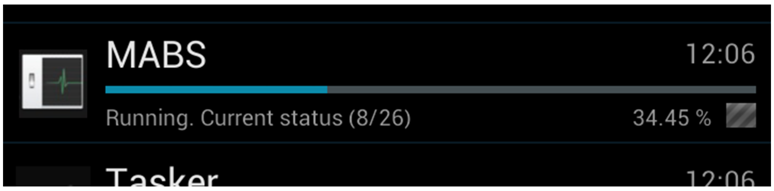

MABS 12:06

Running. Current status (8/26) 34.45 %

Tasker 12:06

Figure B.4: Running measurement status reported in the notification bar of an Android smartphone.

amounts of data is the most time-consuming part of the analysis chain. The resulting ROOT file is only a few megabytes in size and can be processed very quickly. It stores only the information relevant for later analyses, namely hit occurrences with complete charge information for the surrounding pixel cluster and noise data for all pixels for selected frames. As hit and noise information are independent of analysis type, the time-consuming conversion from raw data to ROOT file is skipped if a ROOT file has previously been created and the user enforced no new analysis. The “Run” class holds the processed data and creates many instances of the “HistogramType” class. Each “HistogramType” uses a different analysis approach. For example, the classical hit analysis determines a hit has occurred in pixel i if the collected charge is five times greater than its noise Q^i_{noise}, averaged over the last 100 frames:

$$Q^i_{\text{seed}} - Q^i_{\text{pedestal,seed}} > 5 \cdot Q^i_{\text{noise}}$$

This hit-finding criterion differs from a hit-finding approach where the summed charge of the whole pixel cluster must be three times higher than the summed noise of the cluster:

$$Q_{\text{cluster}} - Q_{\text{pedestal,cluster}} > 3 \cdot Q_{\text{cluster noise}}$$

It should be noted that the summed noise of the cluster and the summed charge are calculated as follows:

$$\begin{aligned}
Q_{\text{cluster}} &= \sum_{i}^{\text{cluster size}} Q^i_{\text{seed}} - Q^i_{\text{pedestal,seed}} \quad , \\
Q_{\text{pedestal,cluster}} &= \sum_{i}^{\text{cluster size}} Q^i_{\text{pedestal}} \quad , \\
Q_{\text{cluster noise}} &= \sqrt{\sum_{i}^{\text{cluster size}} (Q^i_{\text{noise}})^2}
\end{aligned}$$

This additional hit criterion suppresses fake hits that do not have much charge, which is typical in the far left region of the signal response spectrum. Usually, this area is not of interest and is often considered noise.

Other criteria used to discriminate hits are introduced when applied.

Acronyms

3T-Pixel	**3**-**T**ransistor **Pixel**, pixel consisting three transistors
3T	**3**-**T**ransistor, Simplest preamplifier built with three transistors
AC	**A**lternating **C**urrent
ADU	**A**nalog to **D**igital **U**nit, arbitrary unit
ALICE	**A** **L**arge **I**on **C**ollider **E**xperiment, Heavy ion experiment at the LHC
AMS	**A**ustria **M**icro **S**ystems, CMOS process with a structure size of 0.35 µm
ATLAS	**A** **T**oroidal **L**HC **A**pparatu**s**, experiment at theLHC
BNL	**B**rookhaven **N**ational **L**aboratory, research facility on Long Island, USA
β	**Beta-**particle, an electron or positron from a radioactive decay
C++	A standardized general-purpose programming language created in 1979 [Str13].
CCE	**C**harge **C**ollection **E**fficiency, charge collection efficiency
CDS	**C**orrelated **D**ouble **S**ampling
CERN	**C**onseil **E**uropéen pour la **R**echerche **N**ucléaire, Research facility in Geneva, Switzerland
CMOS	**C**omplementary **M**etal-**O**xide-**S**emiconductor
Cd-109	**C**a**d**Cadmium isotope with a mass number of **109**, radioactive, emits γ
DESY	**D**eutsches **E**lektronen-**Sy**nchrotron, research center in Hamburg
DPG	**D**eutsche **P**hysikalische **G**esellschaft, German Physical Society, the world's largest and oldest organisation of physicists
FAIR	**F**acility for **A**ntiproton and **I**on **R**esearch, future expansion of the research facility GSI
FRM II	**F**orschungs**r**eaktor **M**ünchen 2, research neutron source at the Heinz Maier-Leibnitz center
Fe-55	**Fe**rrum-(Iron)-Isotope with a mass number of **55**, radioactive, emits γ
GSI	**G**esellschaft für **S**chwer**i**onenforschung, Research facility near Darmstadt, Germany
γ	Gamma-photon, a photon from a radioactive decay
HFT	**H**eavy **F**lavor **T**racker, Vertex detector of STAR
HR	**H**igh-**R**esistivity, high-resistance epitaxial layer
HV	**H**igh-**V**oltage
IKF	**I**nstitut für **K**ernphysik **F**rankfurt
ILC	**I**international **L**inear **C**ollider
IPHC	**I**nstitut **P**luridisciplinaire **H**ubert **C**URIEN Strasbourg
ITS	**I**nner **T**racking **S**ystem, Vertex detector of ALICE
LHC	**L**arge **H**adron **C**ollider, Accelerator at CERN
LR	**L**ow-**R**esistivity, low-resistance epitaxial layer
MABS	**M**APS **A**automation **B**ot **S**ystem, Custom software and award winning bot controlling the measuring procedure in the laboratory, developed during this thesis
MAPS	**M**onolithic **A**ctive **P**ixel **S**ensor
MEDAPP	**Me**dical **app**lications, instrument at the Heinz Maier-Leibnitz center, primarily built for the medical treatment of tumours
MIMOSA	**M**inimum **I**onizing Particle **MOS** **A**ctive Pixel Sensor, MAPS, that are developed at the IPHC in Strasbourg
MIP	**M**inimal **I**onizing **P**article, minimum ionizing particle, a hypothetical particle with the lowest energy loss in matter, conventionally pions are used in experiments as MIPs

MPV	**M**ost **P**robable **V**alue, bin with the largest entry after a Landau fit, here related to a charge distribution
MVD	**M**icro**v**ertex**d**etector, Vertex detector of CBM
NA61/SHINE	**S**PS **H**eavy **I**on and **N**eutrino **E**xperiment, experiemnt at the SPS
NIEL	**N**on **I**onizing **E**nergy **L**oss, Model for describing non-ionizing radiation damage
NMOS	**N**-Channel-**M**etal-**O**xide-**S**emiconductor Transistor, field effect transistor
PGAA	**P**rompte-**G**amma-**A**ktivierungs-**A**nalyse, a method for the determination of the elementary composition of various solids
PICSEL	**P**hysics with **I**ntegrated **C**mos **S**ensors and **EL**ectron machines, CMOS MAPS development group at the IPHC
PMT	**P**hoto**m**ultiplier **t**ube, a vacuum tube converting photons into an electrical signal
Pipper	**P**ixelated sensor for Ionizing **P**article and **P**hotons **E**nergy **R**esolved detection
R&D	**R**esearch & **D**evelopment
RHIC	**R**elativistic **H**eavy **I**on **C**ollider, accelerator at BNL
ROOT	An object-oriented data analysis framework developed at CERN [BR97].
ROSE	**R**esearch and development **O**n **S**ilicon for future **E**xperiments
RTS	**R**andom-**T**elegraph-**S**ignal
S/N	**S**ignal-**N**oise-Ratio, signal-to-noise ratio
SB-Pixel	**S**elf-**B**ias **Pixel**, Preamplifier layout of a MAPS-Pixels
SB	**S**elf-**B**ias Diode, recharging diode in the preamplifier
SIS100	**S**chwer**i**onen**s**ynchrotron, accelerator at FAIR with the magnetic stiffness of 100 Tm
SPS	**S**uper **P**roton **S**ynchrotron, accelerator at CERN
SRIM	**S**topping Powe**r** of **I**ons in **M**atter
STAR	**S**olenoidal **T**racker **A**t **R**HIC, experiment at RHIC
Sr-90	**Str**ontium-Isotope with a mass number of **90**, radioactive, emits β
TCAD	**T**echnology **C**omputer **A**ided **D**esign, software to models semiconductor fabrication and device operation
THR	**T**ower-Jazz sensors with a **H**igh **R**esistivity epitaxial layer
TID	**T**otal **I**onizing **D**ose, ionizing radiation dose
TRIGA	**T**raining, **R**esearch, **I**sotopes, **G**eneral **A**tomic, research reactor for neutron irradiation, here in the Jožef Stefan Institut, Slovenia
TowerJazz	CMOS-Process by the manufacturer **Tower**-Jazz with a minimum structure size of **0,18**µm
VB	**v**acancies per **b**oron fission
Y-90	**Y**ttrium-90, an isotope of yttrium
CBM	**C**ompressed **B**aryonic **M**atter Experiment, future heavy ion experiment at the research facility FAIR
CPS	**C**MOS **P**ixel **S**ensor
CVD	**C**hemical **V**apor **d**eposition, used to produce synthetic diamond by a controlled process with a heat conductivity of up to 2000 W/m · K
HADES	**H**igh-**A**cceptance **D**iel**e**ctron **S**pectrometer, magnetic spectrometer aimed at studying dielectron production at GSI
PKA	**P**rimary **K**nock-on **A**tom, primary atom displaced by radiation
QCD	**Q**uanten**c**hromo**d**ynamics, field theory of strong interaction
TPG	**T**hermal **P**yrolytic **G**raphite, material with two-dimensional thermal conductivity of about 1500 W/m · K
UML	**U**nified **M**odeling **L**anguage, a diagram often used to visually represent a system along with its main actors

List of Figures

List of Tables

Bibliography

[Abl+17] T. Ablyazimov et al. “Challenges in QCD matter physics –The scientific programme of the Compressed Baryonic Matter experiment at FAIR”. In: *The European Physical Journal A* 53.3 (2017). DOI: `10.1140/epja/i2017-12248-y`.

[Adu16] A Aduszkiewicz. *Report from the NA61/SHINE experiment at the CERN SPS*. Tech. rep. CERN-SPSC-2016-038. SPSC-SR-197. Geneva: CERN, 2016. URL: `http://cds.cern.ch/record/2222876`.

[Aff+16] A. Affolder et al. “Charge collection studies in irradiated HV-CMOS particle detectors”. In: *Journal of Instrumentation* 11.04 (2016), P04007–P04007. DOI: `10.1088/1748-0221/11/04/p04007`.

[al01] G Lindström et al. “Radiation hard silicon detectors—developments by the RD48 (ROSE) collaboration”. In: *Nuclear Instruments and Methods in Physics Research Section A: Accelerators, Spectrometers, Detectors and Associated Equipment* 466.2 (2001), pp. 308–326. DOI: `10.1016/s0168-9002(01)00560-5`.

[al92] P. J. Griffin et al. “Neutron induced displacement damage cross-sections for 10^{-10} - 20 MeV”. In: *Sandia National Lab. report SAND 92-0094* (1992).

[AB75] R. C. Alig and S. Bloom. “Electron-Hole-Pair Creation Energies in Semiconductors”. In: *Physical Review Letters* 35.22 (1975), pp. 1522–1525. DOI: `10.1103/physrevlett.35.1522`.

[Bal+08] Jamie Ballin et al. “Monolithic Active Pixel Sensors (MAPS) in a Quadruple Well Technology for Nearly 100% Fill Factor and Full CMOS Pixels”. In: *Sensors* 8.9 (2008), pp. 5336–5351. DOI: `10.3390/s8095336`.

[Bau+09] J. Baudot et al. “First test results Of MIMOSA-26, a fast CMOS sensor with integrated zero suppression and digitized output”. In: *2009 IEEE Nuclear Science Symposium Conference Record (NSS/MIC)*. IEEE, 2009. DOI: `10.1109/nssmic.2009.5402399`.

[Bre+08] Harald Breitkreutz et al. “Spectral fluence rates of the fast reactor neutron beam MedApp at FRM II”. In: *Nuclear Instruments and Methods in Physics Research Section A: Accelerators, Spectrometers, Detectors and Associated Equipment* 593.3 (2008), pp. 466–471. DOI: `10.1016/j.nima.2008.05.008`.

[BR97] Rene Brun and Fons Rademakers. “ROOT — An object oriented data analysis framework”. In: *Nuclear Instruments and Methods in Physics Research Section A: Accelerators, Spectrometers, Detectors and Associated Equipment* 389.1-2 (1997), pp. 81–86. DOI: `10.1016/s0168-9002(97)00048-x`.

[Bus19] Tobias Bus. “Entwicklung von Messverfahren zur Ermittlung der Verarmungstiefe von Photodioden von CMOS Pixel Sensoren”. Goethe University Frankfurt, 2019. URL: `http://user.uni-frankfurt.de/~xmatter/publication/documents/`.

[BDL17] Tobias Bus, Michael Deveaux, and Benjamin Linnik. “Radiation tolerance of a fully depleted CMOS Monolithic Active Pixel Sensor”. In: *Verhandlungen der Deutschen Physikalischen Gesellschaft* (2017).

[Cin+09] Vladimir Cindro et al. “Radiation damage in p-type silicon irradiated with neutrons and protons”. In: *Nuclear Instruments and Methods in Physics Research Section A: Accelerators, Spectrometers, Detectors and Associated Equipment* 599.1 (2009), pp. 60–65. DOI: `10.1016/j.nima.2008.11.007`.

[Col14] ALICE Collaboration. “Technical Design Report for the Upgrade of the ALICE Inner Tracking System”. In: *Journal of Physics G: Nuclear and Particle Physics* 41.8 (2014), p. 087002. DOI: `10.1088/0954-3899/41/8/087002`.

[Con+15] G Contin et al. “The MAPS based PXL vertex detector for the STAR experiment”. In: *Journal of Instrumentation* 10.03 (2015), p. C03026.

[Con16] G. Contin. “The STAR PXL detector”. In: *Journal of Instrumentation* 11.12 (2016), pp. C12068–C12068. DOI: `10.1088/1748-0221/11/12/c12068`.

[Deg+12] Y. Degerli et al. “A digital Monolithic Active Pixel Sensor chip in a Quadruple-Well CIS process”. In: *2012 IEEE Nuclear Science Symposium and Medical Imaging Conference Record (NSS/MIC)*. IEEE, 2012. DOI: `10.1109/nssmic.2012.6551470`.

[DSa18] Ingo Deppner, Christian Simon, and Norbert Herrmann and. “The physics program of the CBM experiment”. In: *Proceedings of Critical Point and Onset of Deconfinement — PoS(CPOD2017)*. Sissa Medialab, 2018. DOI: `10.22323/1.311.0014`.

[Dep+02] G. Deptuch et al. “Design and testing of monolithic active pixel sensors for charged particle tracking”. In: vol. 1. 2002, 3/103–3/110 vol.1. ISBN: 0780365038. DOI: `10.1109/NSSMIC.2000.949027`.

[Dep02] Grzegorz Deptuch. “New generation of monolithic active pixel sensors for charged particle detection”. PhD thesis. Université Louis Pasteur-Strasbourg I, 2002. URL: `https://tel.archives-ouvertes.fr/tel-00011109/file/these_deptuch.pdf`.

[Dev08] Michael Deveaux. “Development of fast and radiation hard Monolithic Active Pixel Sensors (MAPS) optimized for open charm meson detection with the CBM-vertex detector”. PhD thesis. Université Louis Pasteur-Strasbourg I, 2008. URL: `https://tel.archives-ouvertes.fr/tel-00392111/`.

[Dev15] Michael Deveaux. “Monolithic active pixel sensors”. In: *Proceedings of 24th International Workshop on Vertex Detectors — PoS(VERTEX:045 2015)*. Sissa Medialab, 2015. DOI: `10.22323/1.254.0049`.

[Dev19] Michael Deveaux. “Progress on the radiation tolerance of CMOS Monolithic Active Pixel Sensors”. In: *Journal of Instrumentation* 14.11 (2019), R11001–R11001. DOI: `10.1088/1748-0221/14/11/r11001`.

[Dev+08] Michael Deveaux, S. Amar-Youcef, et al. “Random Telegraph Signal in Monolithic Active Pixel Sensors”. In: *2008 IEEE Nuclear Science Symposium Conference Record*. IEEE, 2008. DOI: `10.1109/nssmic.2008.4775010`.

[Dev+19] Michael Deveaux, B. Arnoldi-Meadows, et al. “Observations on MIMOSIS-0, the first dedicated CPS prototype for the CBM MVD”. In: (2019). arXiv: `1909.05614`.

[Dev+11] Michael Deveaux, J Baudot, et al. “Radiation tolerance of a column parallel CMOS sensor with high resistivity epitaxial layer”. In: *Journal of Instrumentation* 6.02 (2011), pp. C02004–C02004. DOI: `10.1088/1748-0221/6/02/c02004`.

[DH14] Michael Deveaux and Johann M Heuser. “The silicon detector systems of the Compressed Baryonic Matter experiment”. In: *PoS* (2014), p. 009.

[Doe08] Dennis Doering. “Random Telegraph Signal in Monolithic Active Pixel Sensors”. Goethe University Frankfurt, 2008. URL: `http://user.uni-frankfurt.de/~xmatter/publication/documents/2008_Doering_D_bac.pdf`.

[Doe10] Dennis Doering. “Eine Ausheilstudie an bestrahlten Monolithic Active Pixel Sensoren”. Goethe-Universität Frankfurt am Main, 2010. URL: `https://www.gsi.de/documents/DOC-2011-Jan-10.html`.

[Doe15] Dennis Doering. “Untersuchungen zur Verbesserung der Strahlenhärte von CMOS-Sensoren zum Einsatz in Vertexdetektoren von Schwerionenexperimenten”. PhD thesis. Goethe-Universität Frankfurt am Main, 2015. URL: `https://d-nb.info/1072227045/04`.

[Doe+13a] Dennis Doering, Michael Deveaux, et al. “Pitch dependence of the tolerance of CMOS monolithic active pixel sensors to non-ionizing radiation”. In: *Nuclear Instruments and Methods in Physics Research Section A: Accelerators, Spectrometers, Detectors and Associated Equipment* 730 (2013), pp. 111–114. doi: `10.1016/j.nima.2013.04.038`.

[Doe+13b] Dennis Doering, Michael Deveaux, et al. “Pitch dependence of the tolerance of CMOS monolithic active pixel sensors to non-ionizing radiation”. In: *Nuclear Instruments and Methods in Physics Research Section A: Accelerators, Spectrometers, Detectors and Associated Equipment* 730 (2013), pp. 111–114. doi: `10.1016/j.nima.2013.04.038`.

[Dor+10] A Dorokhov et al. “Improved radiation tolerance of MAPS using a depleted epitaxial layer”. In: *Nuclear Instruments and Methods in Physics Research Section A: Accelerators, Spectrometers, Detectors and Associated Equipment* 624.2 (2010), pp. 432–436.

[Dri10] C. et al. Dritsa. “A detector response model for CMOS Monolithic Active Pixel Sensors”. In: *PoS(Bormio2010)015*. 2010.

[DG10] Wojciech Dulinski and Mathieu Goffe. *MIMOSA 34 description*. 2010. url: `www.iphc.cnrs.fr/IMG/pdf/Mimosa34_Description.pdf`.

[Era14] Golla Eranna. *Crystal Growth and Evaluation of Silicon for VLSI and ULSI*. CRC Press, 2014. doi: `10.1201/b17812`.

[FAI16] FAIR. *GSI - FAIR, ”Das Universum im Labor” Flyer*. `https://www.gsi.de/presse/broschueren.htm`. (visited on 03.07.2017). 2016.

[FAI17] FAIR. *Facility for Antiproton and Ion Research: Magnets*. `http://www.fair-center.eu/public/what-is-fair/accelerators/magnets.html`. (visited on 04.07.2017). 2017.

[FAI19] FAIR. *Facility for Antiproton and Ion Research: MVD*. 2019. url: `https://fair-center.eu/for-users/experiments/nuclear-matter-physics/cbm/projects/mvd.html` (visited on 24.7.2019).

[Föl16] Helmut Föll. *Semiconductors*. 2016. url: `http://www.tf.uni-kiel.de/matwis/amat/semi_en/backbone.pdf` (visited on 30.1.2018).

[Fre+02] E. Fretwurst et al. “Radiation Damage in Silicon Detectors Caused by Hadronic and Electromagnetic Irradiation”. In: physics/0211118. DESY-02-199. DESY-2002-199 (2002). url: `http://cds.cern.ch/record/594033`.

[Fri16] Volker Friese. “Strangeness Prospects with the CBM Experiment”. In: *Journal of Physics: Conference Series* 668 (2016), p. 012014. DOI: `10.1088/1742-6596/668/1/012014`.

[Heu16] Johann Heuser. *Workshop on Detector Technologies for High-Energy Physics*. 2016. URL: `https://indico.gsi.de/materialDisplay.py?contribId=0&materialId=slides&confId=6203` (visited on 27.2.2018).

[Hey18] Julian Heymes. “Depletion of CMOS pixel sensors: studies, characterization, and applications”. PhD thesis. Strasbourg, 2018. URL: `https://www.theses.fr/2018STRAE010.pdf`.

[Hol12] Keith E Holbert. “Radiation Effects Damage”. In: *Course EEE 598 Syllabus,* (2012).

[HS95] J H Hubbell and S M Seltzer. *Tables of x-ray mass attenuation coefficients and mass energy-absorption coefficients 1 keV to 20 MeV for elements Z = 1 to 92 and 48 additional substances of dosimetry interest.* Tech. rep. 1995. DOI: `10.6028/nist.ir.5632`.

[Int] ASTM International. *Practice for Characterizing Neutron Fluence Spectra in Terms of an Equivalent Monoenergetic Neutron Fluence for Radiation-Hardness Testing of Electronics.* DOI: `10.1520/e0722-14`.

[IPH18] IPHC. *List of MIMOSA chips*. 2018. URL: `http://www.iphc.cnrs.fr/List-of-MIMOSA-chips.html` (visited on 4.8.2018).

[Kac+16] Maciej Kachel, J. Baudot, et al. *Fully depleted MAPS: Pegasus and MIMOSA 33*. 2016. URL: `http://www.iphc.cnrs.fr/IMG/pdf/mk_mimosa-22sx_nss2016_v6.pdf`.

[KD14] Maciej Kachel and W Dulinski. *MIMOSA-22SX - A Monolithic Active Pixel Sensor for Low Energy X-Ray Counting Applications.* 2014. URL: `https://indico.cern.ch/event/309449/contributions/1680020/attachments/591524/814253/KACHEL_CPIX_FDMAPS_Bonn.pdf`.

[Kes+13] O Kester et al. “Status of the FAIR facility”. In: *Proceedings of IPAC2013, Shanghai, China, TUXB101* (2013), pp. 2084–2087. URL: `https://accelconf.web.cern.ch/IPAC2013/papers/tuxb101.pdf`.

[Kle68] Claude A Klein. “Bandgap dependence and related features of radiation ionization energies in semiconductors”. In: *Journal of Applied Physics* 39.4 (1968), pp. 2029–2038.

[Kni81] Ronald Allen Knief. *Nuclear energy technology: theory and practice of commercial nuclear power*. Hemisphere Publishing Corporation, Washington, DC, 1981. ISBN: 9780891167907.

[Koz11] Michal Koziel. “Development of radiation hardened pixel sensors for charged particle detection”. PhD thesis. Strasbourg, IPHC, 2011. URL: `https://cds.cern.ch/record/1742056/files/CERN-ACC-2014-0090.pdf`.

[Kra84] H.W. Kraner. “Radiation damage in silicon detectors”. In: *Nuclear Instruments and Methods in Physics Research* 225.3 (1984), pp. 615–618. DOI: `10.1016/0167-5087(84)90114-5`.

[Kud+08] P. Kudejova et al. “The new PGAA and PGAI facility at the research reactor FRM II in Garching near Munich”. In: *Journal of Radioanalytical and Nuclear Chemistry* 278.3 (2008), pp. 691–695. DOI: `10.1007/s10967-008-1506-9`.

[Lan44] L. Landau. “On the energy loss of fast particles by ionization”. In: *J. Phys.(USSR)* (1944), pp. 417–424. DOI: `10.1016/b978-0-08-010586-4.50061-4`.

[LR07] Claude Leroy and Pier-Giorgio Rancoita. “Particle interaction and displacement damage in silicon devices operated in radiation environments”. In: *Reports on Progress in Physics* 70.4 (2007), pp. 493–625. DOI: `10.1088/0034-4885/70/4/r01`.

[Lin03] Gunnar Lindström. “Radiation damage in silicon detectors”. In: *Nuclear Instruments and Methods in Physics Research Section A: Accelerators, Spectrometers, Detectors and Associated Equipment* 512.1-2 (2003), pp. 30–43. DOI: `10.1016/s0168-9002(03)01874-6`.

[Lin14a] Benjamin Linnik. *Automatisierung von Messprozeduren zur systematischen Charakterisierung von Pixelsensoren.* 2014. URL: `https://www.dpg-verhandlungen.de/year/2014/conference/frankfurt/part/hk/session/46/contribution/64`.

[Lin14b] Benjamin Linnik. *Documentation of MABS hosted at the website of the x-matter group at the IKF.* 2014. URL: `http://jspc29.%20x-matter.uni-frankfurt.de/mabs/documentation/`.

[Lin19] Benjamin Linnik. *MABS_Run_Analyzer: Documentation.* 2019. URL: `http://jspc29.x-matter.uni-frankfurt.de/mabs/documentation/html/index.html` (visited on 24.7.2019).

[Lin+17] Benjamin Linnik, Tobias Bus, et al. “Radiation damage caused by cold neutrons in boron doped CMOS active pixel sensors”. In: *Journal of Instrumentation* 12.05 (2017), pp. C05011–C05011. DOI: `10.1088/1748-0221/12/05/c05011`.

[LDB16] Benjamin Linnik, Michael Deveaux, and Tobias Bus. *27th CBM Collaboration Meeting (11-15 April 2016), Status of radiation hardness.* 2016. URL: `https://indico.gsi.de/event/3620/other-view?view=standard`.

[LDB17] Benjamin Linnik, Michael Deveaux, and Tobias Bus. *29th CBM Collaboration Meeting (20-24 March 2017), Status of radiation hardness.* 2017. URL: `https://indico.gsi.de/event/4759/session/10/contribution/48/material/slides/1.pdf`.

[Lut07] Gerhard Lutz. "Detectors for Position and Energy Measurement". In: *Semiconductor Radiation Detectors.* Springer Berlin Heidelberg, 2007, pp. 109–152. DOI: `10.1007/978-3-540-71679-2_6`.

[Man+03] I. Mandic, V. Cindro, G. Kramberger, E.S. Kristof, M. Mikuz, and D. Vrtacnik. "Radiation damage in bipolar transistors caused by thermal neutrons". In: *2003 IEEE Nuclear Science Symposium. Conference Record (IEEE Cat. No.03CH37515).* IEEE, 2003. DOI: `10.1109/nssmic.2003.1352077`.

[Man+04] I. Mandic, V. Cindro, G. Kramberger, E.S. Kristof, M. Mikuz, D. Vrtacnik, et al. "Bulk damage in DMILL npn bipolar transistors caused by thermal neutrons versus protons and fast neutrons". In: *IEEE Transactions on Nuclear Science* 51.4 (2004), pp. 1752–1758. DOI: `10.1109/tns.2004.832927`.

[Man] Igor Mandic. *Ljubljana Neutron Irradiation Facility.* URL: `http://www-f9.ijs.si/~mandic/ReacSetup.html` (visited on 12.10.2017).

[Man+17] I. Mandić et al. "Neutron irradiation test of depleted CMOS pixel detector prototypes". In: *Journal of Instrumentation* 12.02 (2017), P02021–P02021. DOI: `10.1088/1748-0221/12/02/p02021`.

[Mer18] Stefano Meroli. *The Landau distribution for ionizing particles.* 2018. URL: `http://meroli.web.cern.ch/Lecture_landau_ionizing_particle.html` (visited on 1.7.2018).

[Mes+03] S.R. Messenger et al. "Niel for heavy ions: an analytical approach". In: *IEEE Transactions on Nuclear Science* 50.6 (2003), pp. 1919–1923. DOI: `10.1109/tns.2003.820762`.

[Mor+20] F Morel et al. "Toward the MIMOSIS sensor of the CBM-MVD". In: *CBM Progress Report 2019* (2020), p. 7. DOI: `10.15120/GSI-2020-00904`.

[OP04] Alan Owens and A. Peacock. "Compound semiconductor radiation detectors". In: *Nuclear Instruments and Methods in Physics Research Section A: Accelerators, Spectrometers, Detectors and Associated Equipment* 531.1-2 (2004), pp. 18–37. DOI: `10.1016/j.nima.2004.05.071`.

[Par16] Particle Data Group. "Review of Particle Physics". In: *Chinese Physics C* 40.10 (2016), p. 443. DOI: `10.1088/1674-1137/40/10/100001`.

[Pot+13] A. Potenza et al. “Radiation tolerance of a moderate resistivity substrate in a modern CMOS process”. In: *Nuclear Instruments and Methods in Physics Research Section A: Accelerators, Spectrometers, Detectors and Associated Equipment* 718 (2013), pp. 347–349. DOI: `10.1016/j.nima.2012.10.020`.

[PS08] B. Pritychenko and A.A. Sonzogni. “Sigma: Web Retrieval Interface for Nuclear Reaction Data”. In: *Nuclear Data Sheets* 109.12 (2008), pp. 2822–2827. DOI: `10.1016/j.nds.2008.11.017`.

[Rev15] Zsolt Revay. “PGAA: Prompt gamma and in-beam neutron activation analysis facility”. In: *Journal of large-scale research facilities JLSRF* 1 (2015). DOI: `10.17815/jlsrf-1-46`.

[Sch+88] J.R. Schwank et al. “Temperature effects on the radiation response of MOS devices”. In: *IEEE Transactions on Nuclear Science* 35.6 (1988), pp. 1432–1437. DOI: `10.1109/23.25476`.

[Sch59] H. C. Schweinler. “Some Consequences of Thermal Neutron Capture in Silicon and Germanium”. In: *Journal of Applied Physics* 30.8 (1959), pp. 1125–1126. DOI: `10.1063/1.1735281`.

[Sen+14] Serhiy Senyukov et al. “Development of CMOS pixel sensors for tracking and vertexing in high energy physics experiments”. In: (2014). arXiv: `1402.2172 [physics.ins-det]`.

[Sig14] Peter Sigmund. *Particle Penetration and Radiation Effects Volume 2*. Springer International Publishing, 2014. DOI: `10.1007/978-3-319-05564-0`.

[Smi+14] A Smirnov et al. “Ultrahigh vacuum in superconducting synchrotrons”. In: *Proceedings of RUPAC2014, Obninsk, Russia* (2014), pp. 23–25. DOI: `10.1063/1.58890`.

[SŽT12] Luka Snoj, Gašper Žerovnik, and Andrej Trkov. “Computational analysis of irradiation facilities at the JSI TRIGA reactor”. In: *Applied Radiation and Isotopes* 70.3 (2012), pp. 483–488. DOI: `10.1016/j.apradiso.2011.11.042`.

[SF06] P. Spiller and G. Franchetti. “The FAIR accelerator project at GSI”. In: *Nuclear Instruments and Methods in Physics Research Section A: Accelerators, Spectrometers, Detectors and Associated Equipment* 561.2 (2006), pp. 305–309. DOI: `10.1016/j.nima.2006.01.043`.

[Sta11] M. Stanitzki. “Advanced monolithic active pixel sensors for tracking, vertexing and calorimetry with full CMOS capability”. In: *Nuclear Instruments and Methods in Physics Research Section A: Accelerators, Spectrometers, Detectors and Associated Equipment* 650.1 (2011), pp. 178–183. DOI: `10.1016/j.nima.2010.11.166`.

[Str17] Joachim Stroth. “Status and Plans of HADES”. In: 2017, pp. 68–78. arXiv: `1701.07346 [hep-ph]`.

[Str13] B. Stroustrup. *The C++ Programming Language*. Addison-Wesley, 2013. ISBN: 9780321958327. URL: `https://books.google.de/books?id=AFuLnQEACAAJ`.

[SB93] GP Summers and EA Burke. “Ph. Shapiro, SR Messenger, RJ Walters”. In: *IEEE Trans. Nuclear Science, NS* 40 (1993), p. 1372.

[Sze85] S. M. Sze. *Semiconductor Devices: Physics And Technology*. Wiley, New York, 1985. ISBN: 812651681X.

[The18] Wikipedia Contributor TheNoise. *Datei:Pn-junction-equilibrium-graphs.png*. 2018. URL: `https://de.wikipedia.org/wiki/Datei:Pn-junction-equilibrium-graphs.png` (visited on 23.1.2018).

[Tow13] TowerJazz. *TowerJazz was Selected as Silicon Provider for the Upgrade of the Inner Tracking System of the ALICE Experiment at CERN*. Press Release. 2013. URL: `http://www.towerjazz.com/prs/2013/pdf/pr11202013.pdf`.

[Van+80] Victor AJ Van Lint et al. “Mechanisms of radiation effects in electronic materials. Volume 1”. In: *NASA STI/Recon Technical Report A* 81 (1980).

[VL00a] A Vasilescu and G Lindstroem. “Displacement damage in silicon, on-line compilation”. In: (2000). URL: `http://rd50.web.cern.ch/RD50/NIEL/default.html`.

[Vas97] Angela Vasilescu. “The NIEL scaling hypothesis applied to neutron spectra of irradiation facilities and in the ATLAS and CMS SCT”. In: *ROSE= TN* (1997), pp. 97–2. URL: `https://rd48.web.cern.ch/RD48/technical-notes/rosetn972.ps`.

[VL00b] Angela Vasilescu and Gunnar Lindström. “Notes on the fluence normalisation based on the NIEL scaling hypothesis”. In: *ROSE/TN* 2 (2000). URL: `http://cern.ch/RD48/technical-notes/rosetn00-02.ps`.

[Win11] M Winter. “CMOS Pixel sensors designed for the ALICE-ITS upgrade”. In: *Présentation ALICE Upgrade forum*. Vol. 29. 2011. URL: `https://indico.cern.ch/event/144152/session/4/contribution/6/attachments/133916/190028/Winter-mso_workshop_sept11_v2.pdf`.

[Wun+92] R. Wunstorf et al. “Results on radiation hardness of silicon detectors up to neutron fluences of 1015 n/cm2”. In: *Nuclear Instruments and Methods in Physics Research Section A: Accelerators, Spectrometers, Detectors and Associated Equipment* 315.1-3 (1992), pp. 149–155. DOI: `10.1016/0168-9002(92)90696-2`.

[Wun92] Renate Wunstorf. “A Systematic investigation of the radiation hardness of silicon detectors for high-energy physics experiments”. PhD thesis. Hamburg U., 1992. URL: `http://www-library.desy.de/cgi-bin/showprep.pl?DESY-FH1K-92-01`.

[Xap+04] M.A. Xapsos et al. “NIEL calculations for high-energy heavy ions”. In: *IEEE Transactions on Nuclear Science* 51.6 (2004), pp. 3250–3254. DOI: `10.1109/tns.2004.839136`.

[Yaz19] A. Yazgili. “Toleranz von MAPS gegenüber thermischen Neutronen”. bachelorthesis. Goethe University Frankfurt, 2019. URL: `https://indico.gsi.de/event/8804/contributions/43578/attachments/30928/38573/Abschlussarbeit_Ali_Yazgili-1.pdf`.

[ZZB10] James F. Ziegler, M.D. Ziegler, and J.P. Biersack. “SRIM – The stopping and range of ions in matter (2010)”. In: *Nuclear Instruments and Methods in Physics Research Section B: Beam Interactions with Materials and Atoms* 268.11-12 (2010), pp. 1818–1823. DOI: `10.1016/j.nimb.2010.02.091`.

Acknowledgment

First, I would like to thank Professor Joachim Stroth for the possibility of writing this thesis in his working group. It allowed me to work on a topic that is both highly relevant and exciting. During my research, a lot of progress was achieved in the field of radiation hardness of CMOS sensors. New articles on this topic were published every week and I visited multiple conferences where I met scientists from all over the world. The research in a field that is so fast evolving makes me proud. The possibilities given in our laboratories for the experimental investigations left nothing to be desired.

Michael Deveaux and Dennis Doering supported me in my investigations and helped whenever asked. I thank Michael Deveaux not only for being a dedicated scientific supervisor but also for being a mentor and a role model. His ideas and constructive discussions always inspired me. I thank the IPHC group in Strasbourg for providing us the CMOS MAPS and the laboratory equipment. I want to thank Dennis Doering for his patience, as he introduced me to a new field – experimental radiation hardness studies. I could always discuss, plan and fulfill our experimental goals with him. I thank Christian Muentz for providing us with the necessary space for our experiments. Jan Michel I thank for all the technical support and for providing us with an own server where MABS could be hosted. Furthermore, I would like to thank Alex Meistrenko, the conversations we had and his perseverance kept me going. A very special thanks to Benedict Arnoldi-Meadows for his in-depth and very helpful comments.

Thanks also to the whole IKF working group for the great atmosphere I have always liked. I enjoyed being part of a group of high performers.

I thank my mother, Marina Linnik, for encouraging me to study physics and always supported my knowledge and science hunger. I thank my father, Vladimir Brjuchanov, for the many inspiring conversations and his wisdom.

Finally, I would like to thank Tsvetelina Milanova, who always supported me and showed understanding.